

TROPISCAT FINAL REPORT

ESA CONTRACT N°4000103506/11/NL/CT/FK



Prepared by	ONERA Team (P. Borderies, C. Albinet, A. Hamadi, P. Dubois-Fernandez) POLIMI Team (F. Rocca, S. Tebaldini, D. Ho Tong Minh) CESBIO Team (T. Le Toan, L. Villard, T. Koleck)	
Approved by	Thierry Koleck (CESBIO)	Date and signature 19/06/2013 

TropiScat Final Report DCT/SI/AR/13-11019	Issue : 1 Date : 16/06/2013 Page : 2/136
---	--

DOCUMENT INFORMATION

Document Title: TropiScat Final Report
Keyword :BIOMASS, TropiScat
Writers : ONERA Team (P. Borderies, C. Albinet, P. Dubois-Fernandez) POLIMI Team (F. Rocca, S. Tebaldini, D. Ho Tong Minh, C. Prati) CESBIO Team (T. Le Toan, L. Villard, T. Koleck)
Summary : This document summarizes the work done during the TropiScat experiment in French Guiana

DOCUMENT CHANGES

Issue	Date	Changes	Comments
Draft	19/04/13		
1	19/06/13		

REFERENCE DOCUMENTS:

RD 1: Statement of Work, Appendix 1 to RFQ 3-13299/11/NL/CT/fk, "Technical Assistance For The Deployment Of Tower-based Radar and Geophysical Measurements during the TropiScat Experiment"

RD 2: TropiScat Data Acquisition Report, ref [DCT-SI-AR-13-11018](#)

RD 3: Statement of Work for CR/CCN 1 to TropiScat ESTEC Contract 4000103506/11/NL/CT, ref EOP-SM/2386

SUMMARY

1. INTRODUCTION	6
2. WORK PACKAGE ORGANISATION	7
3. WP 10: CAMPAIGN PREPARATION.....	8
3.1. WP 11: EXPERIMENT DEFINITION.....	8
3.2. WP 12: HARDWARE ACQUISITION & SHIPPING	9
3.3. WP 13: EXPERIMENT SETUP ON GUYAFLUX.....	11
3.4. WP 14: POLARIMETRIC TESTS AND VALIDATION	14
3.4.1. ANALYSE OF IMPULSE RESPONSES.....	14
3.4.2. SYSTEM COHERENCE.....	17
3.5. WP 15: TOMOGRAPHIC TESTS AND VALIDATION	18
3.5.1. DELAY COMPENSATION	18
3.5.2. PULSE RESPONSE.....	20
3.5.3. TOMOGRAM STABILITY AS A FUNCTION OF THE ACQUISITION TIME	23
3.5.4. ANALYSIS OF TOWER STABILITY	26
3.5.5. CONCLUSIONS	31
4. WP 20: DATA ACQUISITION.....	33
4.1. WP 21: DATA PRE-PROCESSING & QUALITY ASSESSMENT	33
4.2. WP 22: IN-SITU DATA	33
5. WP 30: DATA PROCESSING AND ANALYSIS.....	35
5.1. WP 31: TEMPORAL COHERENCE DATA PROCESSING	35
5.1.1. OVERVIEW OF DATA PROCESSING	35
5.1.2. TEMPORAL COHERENCE	39
5.1.3. BACKSCATTERING COEFFICIENT RESULTS.....	51
5.1.4. CONCLUSION.....	58
5.1.5. REFERENCES	59
5.2. WP 32: TOMOGRAPHIC DATA PROCESSING.....	60
5.2.1. TOMOGRAPHIC IMAGING	60

5.2.2. MULTI FREQUENCY TOMOGRAM	61
5.2.3. MULTI TEMPORAL TOMOGRAM.....	62
5.2.4. COHERENCE MATRIX ANALYSIS	65
5.2.5. TEMPORAL COHERENCE AS A FUNCTION OF VERTICAL STRUCTURE.....	71
5.2.6. TEMPORAL COHERENCE DURING THE DRY SEASON.....	75
5.2.7. CONCLUSIONS	77
5.3. WP 33: DATA INVENTORY	78
6. WP 40 TROPISAR DATA REPROCESSING	79
6.1. WP41: REPROCESSING OF TROPISAR DATA.....	79
6.1.1. SAR DATA ACQUISITION SCHEDULE	79
6.1.2. THE SETHI SAR SYSTEM AND ACQUISITION RADAR PARAMETERS.....	80
6.1.3. SAR DATA ACQUISITION FLIGHT DESCRIPTION AND LIST OF REPROCESSED IMAGES	81
6.1.4. PROCESSING WORKFLOW.....	82
6.1.5. DATA QUALITY ASSESSMENT SUMMARY	84
6.2. WP42 : POLINSAR FOREST HEIGHT RETRIEVAL	87
6.2.1. DISTORTION LINKED TO RADAR GEOMETRY AND PROPOSED COMPARISON APPROACH	87
6.2.2. SINGLE BASELINE POLINSAR INVERSION TECHNIQUE.....	90
6.2.3. GROUND ELEVATION	92
6.2.4. VEGETATION HEIGHT	94
6.2.5. CONCLUSIONS	101
6.2.6. REFERENCES	102
6.3. WP 43: PERFORMANCE ANALYSIS POLINSAR AND BACKSCATTERING COEFFICIENT.....	103
6.3.1. METRICS TO QUANTIFY THE PERFORMANCE OF POLINSAR AND INTENSITY BASED FOREST HEIGHT AND BIOMASS INVERSION.....	103
6.3.2. RETRIEVAL ALGORITHM AND PERFORMANCE	104
6.3.3. IMPACT OF TOPOGRAPHY	113
6.3.4. IMPACT OF FILTERING/TEMPORAL VARIATIONS	114
6.3.5. CONCLUSIONS	114

6.3.6. REFERENCES	115
6.4. WP 44: PERFORMANCE ANALYSIS TOMOGRAPHY.....	116
6.4.1. 6 MHZ DATA GENERATION.....	116
6.4.2. TOMOGRAPHIC PROCESSING	119
6.4.3. TOMSAR RESULTS	121
6.4.4. CORRELATION BETWEEN TOMSAR AND ABOVE GROUND FOREST BIOMASS	122
6.4.5. FOREST HEIGHT ESTIMATION	125
6.4.6. CONCLUSIONS	128
6.4.7. REFERENCES	129
7. CONCLUSIONS AND RECOMMENDATIONS.....	131
7.1. TROPISCAT.....	131
7.1.1. EXPERIMENTAL SET UP	131
7.1.2. TEMPORAL DECORRELATION.....	131
7.1.3. BACKSCATTERING INTENSITY.....	132
7.1.4. TOMOSAR.....	132
7.1.5. TROPISCAT RECOMMENDATIONS/ FURTHER WORKS.....	133
7.2. ASSESSMENT OF RETRIEVAL PERFORMANCE WITH TROPISAR 6 MHZ DATA133	
7.2.1. THE PROCESSED DATA.....	133
7.2.2. ASSESSMENT OF POLSAR RETRIEVAL ALGORITHM	134
7.2.3. POLINSAR	134
7.2.4. POLSAR & POLINSAR	134
7.2.5. TOMOSAR.....	135
7.2.6. RECOMMENDATIONS AND FURTHER WORKS.....	135

1. INTRODUCTION

The retrieval algorithms currently developed for BIOMASS are based on the use of P-band vectorial intensity and interferometry or tomography. The last two techniques require high temporal coherence for coherent processing of data from repeat pass acquisitions. The condition to have exploitable interferometric or tomographic information is to have high temporal coherence over forests for time intervals compatible with the BIOMASS mission. This requirement is particularly important for tropical forests for which interferometric (Pol-InSAR and tomography SAR) measurements can efficiently complement polarimetric data, temporal coherence has been addressed during the TropiSAR experiment, over a dense tropical forest in French Guiana, during which multi-temporal acquisitions during a 20 days period have been performed in August 2009. In order to have more complete variations of the measurements in a full range of seasons and weather conditions, ESA and CNES decided to develop and deploy the ground based TropiScat experiment chosen to be set up at the Paracou field station, which is the same site investigated during the TropiSAR campaign.

The major objectives of the experiment are the temporal survey of the variation of the measurements in time scales ranging from diurnal, weekly, monthly, up to 12 months of observation. The measurements which have to be tracked are in order of priority:

- The temporal coherence in HH, VV and HV polarizations, at a very short rate in the order of 15 minutes, covering daily and monthly scale,
- The backscattering coefficient at HH, VV and HV polarizations and in all time scales,
- 2D vertical imaging through tomographic focusing;
- the vertical distribution of temporal coherence, as obtained by comparing tomographic data taken at different times, covering time scales of minutes, days, and months.

In addition to electromagnetic scattering measurements, ancillary in-situ data are also collected on the same area.

2. WORK PACKAGE ORGANISATION

As described in the contract, this study has been organized in work packages, as shown in Figure 1.

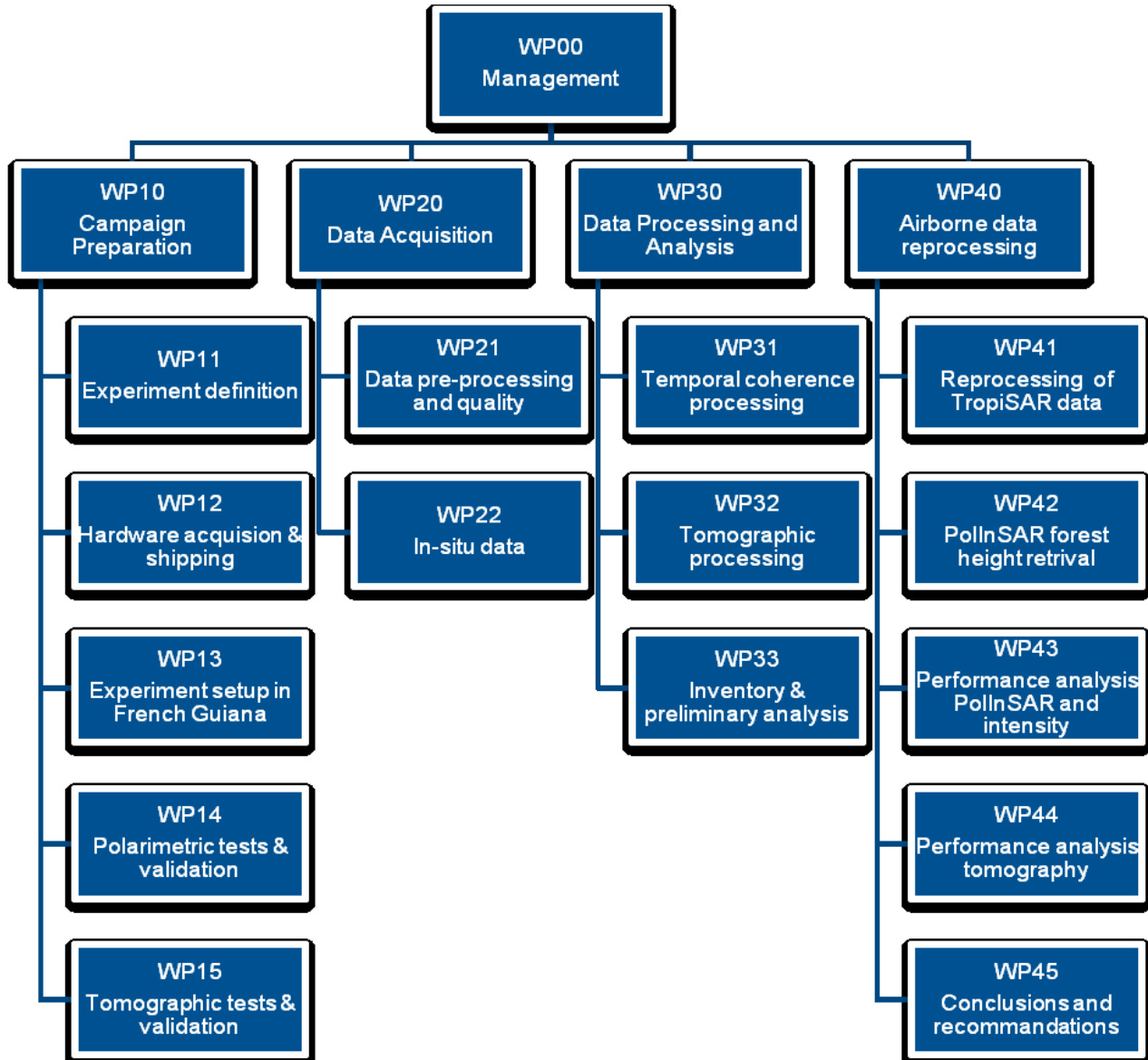


Figure 1 - Work Packages organization

This document summarizes the activities done in each work package. The document plan follows this organization.

3. WP 10: CAMPAIGN PREPARATION

3.1.WP 11: EXPERIMENT DEFINITION

This work package was dedicated to the definition of the TropiScat instrument.

The full description of this work is in the Data Acquisition Report (RD 2).

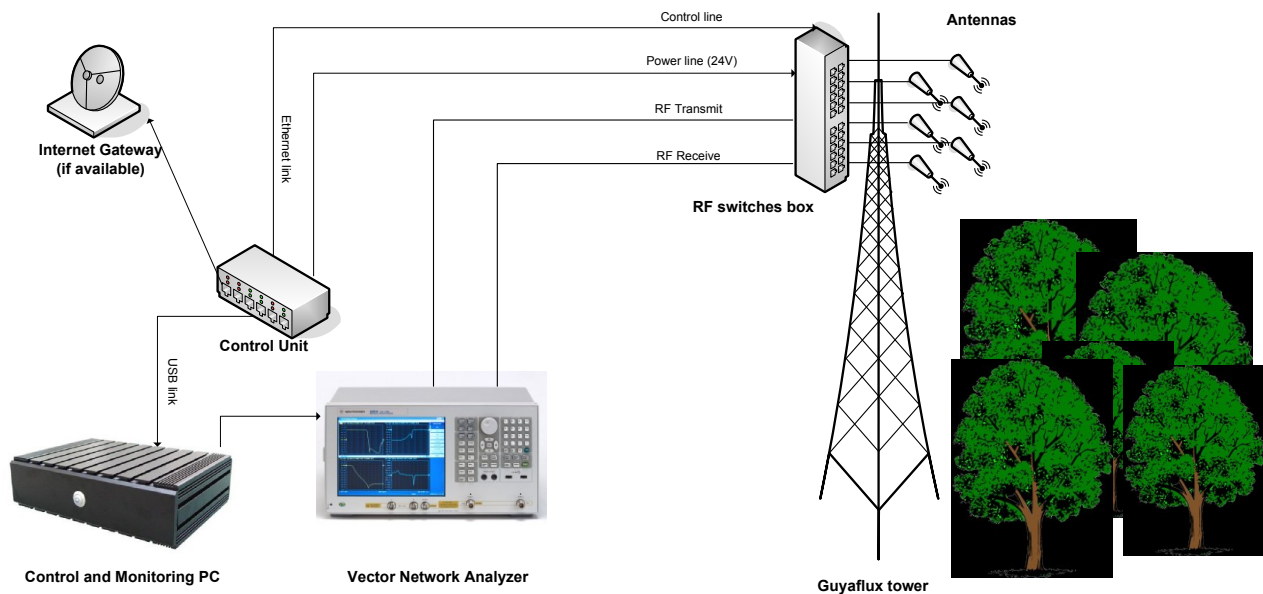


Figure 2 - Synoptic of the TropiScat instrument

The main TropiScat hardware is composed of a VNA, a tropicalized industrial computer PC, a set of wide-band antennas, a radio frequency (RF) switching box and a command unit.

The VNA works as a transmitter/receiver (RX/TX) device. So it has been configured in S21 mode (port 1 in TX, port 2 in RX).

The VNA generates a RF signal, over a 200 MHz frequency band. This signal travels in a low-loss cable to the RF switch box, which routes the signal to the selected TX antenna. This antenna radiates to the forest. Then the backscattered signal is received by the selected RX antenna and driven to the VNA via a second low-loss cable. The VNA records the S21 parameter over the frequency band.

An array of 20 antennas has been designed to fulfill the requirements for the tomography acquisitions. This design had to deal with mechanical and electrical constraints due to the antenna type (log-periodic antennas): the inter antenna coupling must be minimized and the TX and RX antennas must be separated. The final antenna array design is shown on Figure 3.

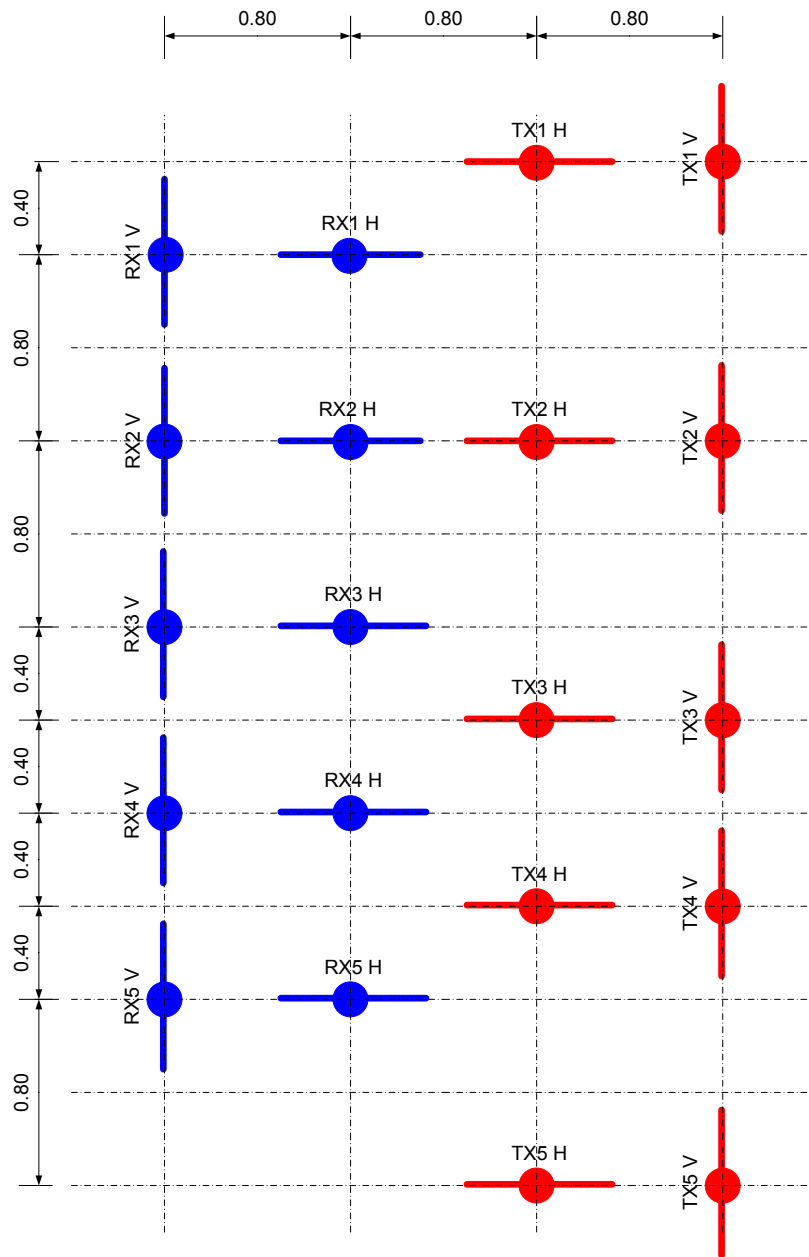


Figure 3 - Geometry of the antenna array

The definition of the experiment has taken into account the environment where the instrument is deployed. The main constraints we have to deal with were:

- The tropical climatic conditions (temperature, humidity, sun)
- The limited electrical power available and its quality
- The autonomy of the instrument because of the lack of remote control capability.

3.2.WP 12: HARDWARE ACQUISITION & SHIPPING

As output of WP11, the instrument design has been defined, with technical specifications for the components. After a comparison of available components in the commercial market, we choose the following devices:

- The Vector Network Analyzer is an Agilent E6051B,
- Antennas have been provided by Satimo Italy (LP 400 model),
- The switch boxes have been designed and build by the team, using four Agilent SP6T electromechanical switches.
- Low-loss cables from Elhyte supplier.

Hardware has been shipped to French Guiana, according the French exportation rules to French Overseas Departments with the support of the Centre Spatial Guyannais.



Figure 4 - Trihedral and dihedral reflectors used during the campaign

3.3.WP 13: EXPERIMENT SETUP ON GUYAFLUX

This experiment has been installed on the Guyaflux tower, at the CIRAD Paracou station, during October 2011. This tower is fully described in <http://www.ecofog.gf/spip.php?article365>

A full description of the Paracou site is given in the Data Acquisition Report (RD 2).

The Guyaflux tower is a 55 meters height metallic structure.

The first step of the installation campaign was the setup of the antennas array, according the geometry given in Figure 3. This geometry is a view from the array, in the forward direction.

A metallic structure has been built and fixed on the tower top.



Figure 5 - Set up of the antennas (left) on the tower, so as to form the vertical array (right)

Two 70 meters long low-loss cables have been used to connect the VNA to the RF switch boxes.

The ground equipment has been installed in a small technical bungalow.



Figure 6 - Technical cabin at the Guyaflux tower

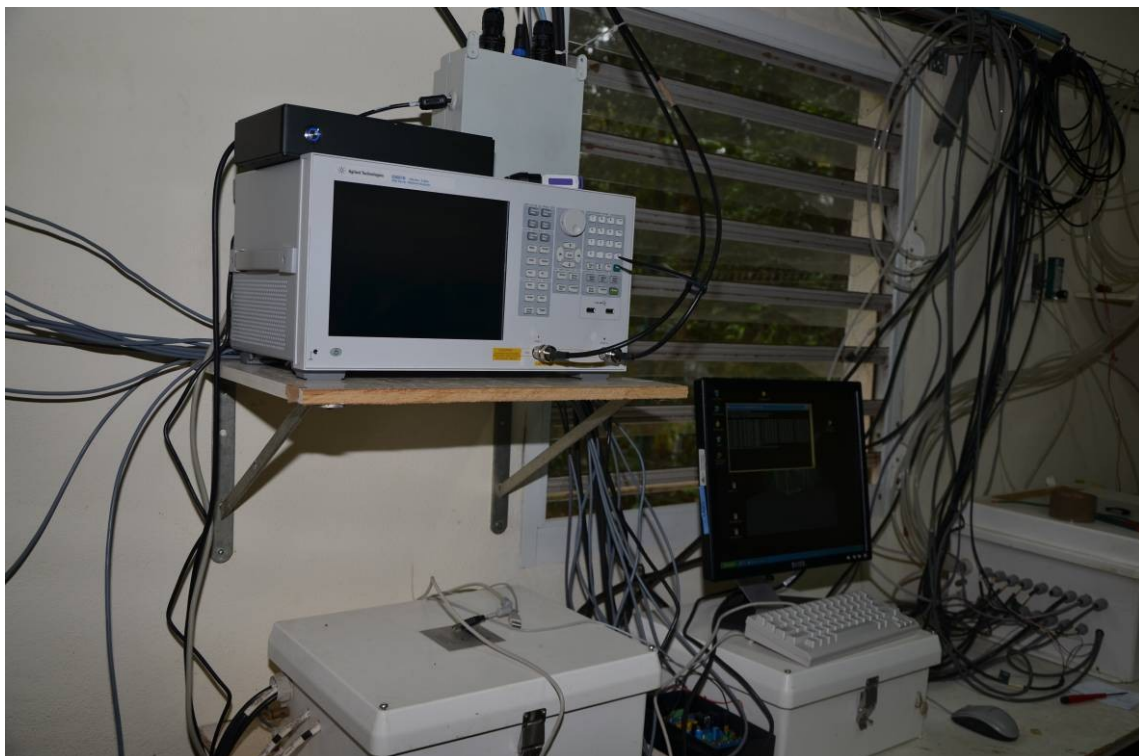


Figure 7 - TropiScat hardware: VNA, computer and switch box driver

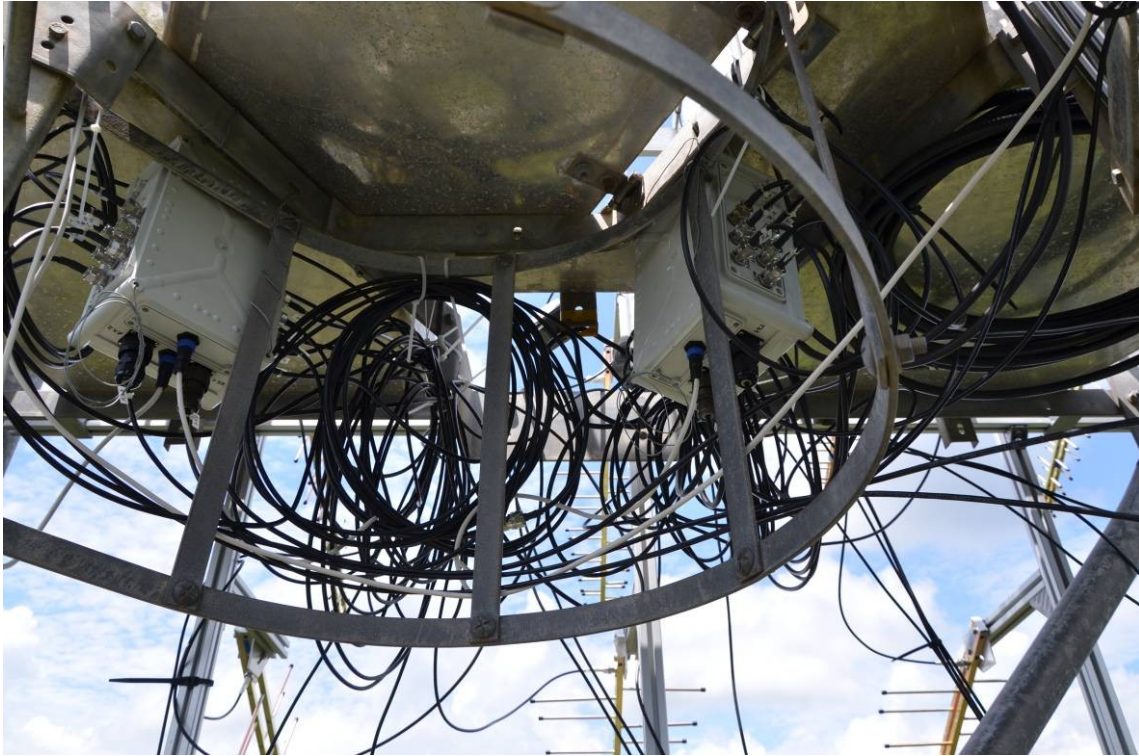


Figure 8 - View of the 2 RF switch boxes on the tower top

Electrical power (220V AC 50Hz) is provided by solar panels, located at 400 meters from the tower. To support the TropiScat experiment consumption, the existing solar panels surface has been extended by 12 meters square. Battery units have been also renewed to increase to electrical storage capacity.

3.4.WP 14: POLARIMETRIC TESTS AND VALIDATION

3.4.1. ANALYSE OF IMPULSE RESPONSES

The first tests was dedicated to the checking of the impulse responses of the system i.e. the responses of the system in the time domain.

Next figures show typical examples of impulse responses of the forest for the 3 polarizations: HH in Figure 9, VV in Figure 10 and HV in Figure 11. First, one can see that the result is as expected. In the very low range (few meters) the direct coupling between the two considered antennas is clearly present. Then the tower echo is obvious as decreasing lobes. It may include some resonances between the antennas of the array themselves and interactions with the tower. Afterwards at approximately 25 m range the part of the forest closest to the antennas begin to appear with contribution of the volume part of the forest only. The nadir echo appears at around 55 m range. Beyond the complete forest is seen by the radar.

On the graphs, it can be checked that at 25 m the tower contribution is more than 15 dB below the first significant echoes of the forest and looking at its decaying behavior one can see that the tower echo contribute insignificantly to the foliage only response, and the full forest is free of tower contribution.

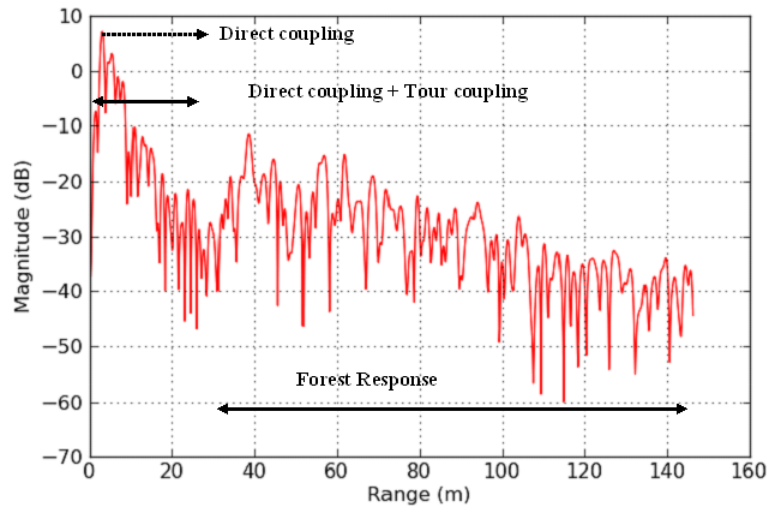


Figure 9: Example of forest raw impulse response : HH polarisation

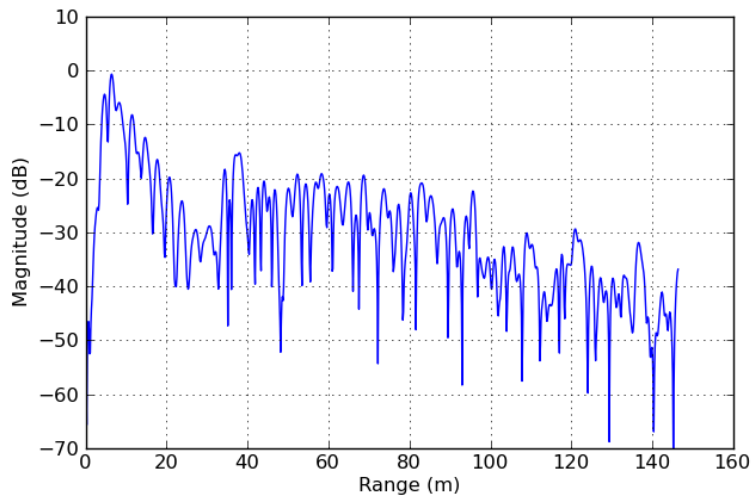


Figure 10: Example of forest raw impulse response: VV polarisation

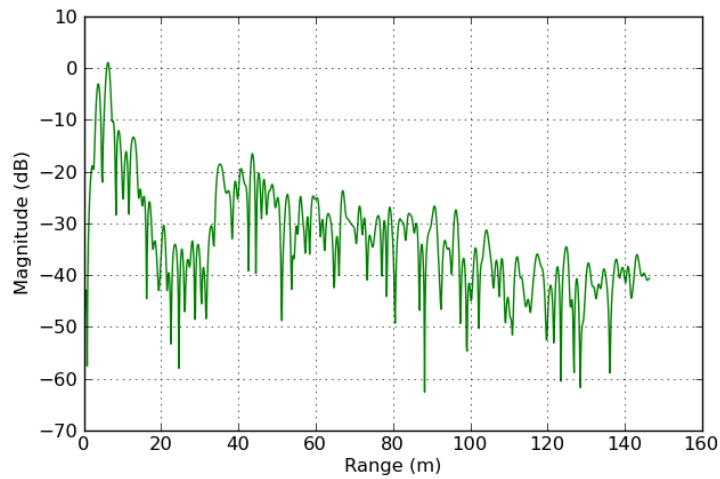


Figure 11 : Example of forest raw impulse response: HV polarization

Some measurements has been done with a corner reflector (CR) on ground.

Figure 12 represents the forest with the corner reflector (HH polarization) (blue curve) and the forest alone (red curve). We can observe a higher level at 62 meters (in range) that correspond to the corner reflector response. Figure 13 represent the corner reflector as it appears with forest removing with complex subtraction of the forest 15 minutes before. It can be seen that the CR contribution is highly mixed with the forest echoes and that the continuous presence of the CR in the forest would not be very helpful. Conversely, with chamber (forest) removing it appears very clearly well above the residual noise in its expected location. When repeating this operation in HV, a level 17 dB below is measured. This means that the cross talk is lower than this value. Actually, averaging over all antenna couples, an average cross polarization of 16 dB is obtained. This threshold is widely sufficient for insuring that the experiment is validated for full polarimetry since the levels expected and effectively measured for HV are in the order of 6 dB below the main polarizations.

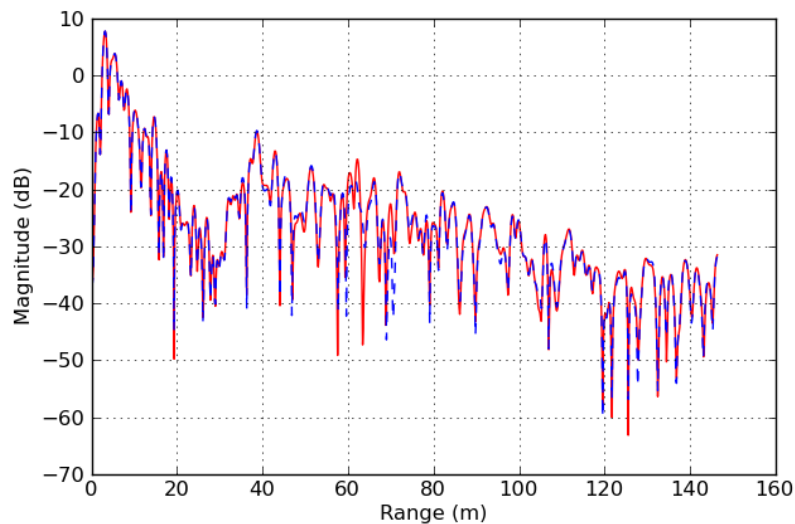


Figure 12: Impulse response of forest with corner reflector embedded and forest alone

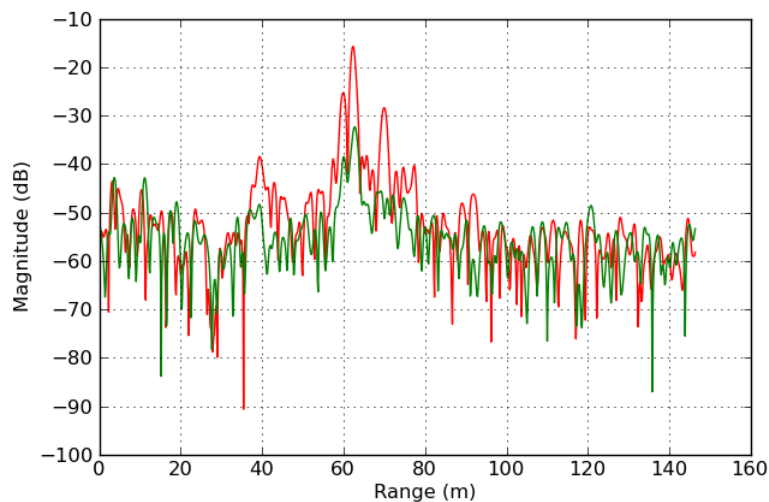


Figure 13: Impulse response of corner reflector minus forest (red : HH; green: HV)

3.4.2. SYSTEM COHERENCE

The main objective of this experiment is the estimation of the long term coherence of the forest backscattering. However the system itself may present some phase instabilities which might spoil the coherence estimation. Therefore, the system coherence was evaluated by considering the responses of the antennas at the coupling level, considering range cells around the coupling peak. Results are shown on Figure 14 for the dry period and on Figure 15 for the rainy one, for the average coherence at 6 a.m. In the following, these average coherences will be taken into account for the computation of the forest coherence. Indeed, even if they indicate a stable behavior of the experiment, their influence on the forest result has to be accounted for.

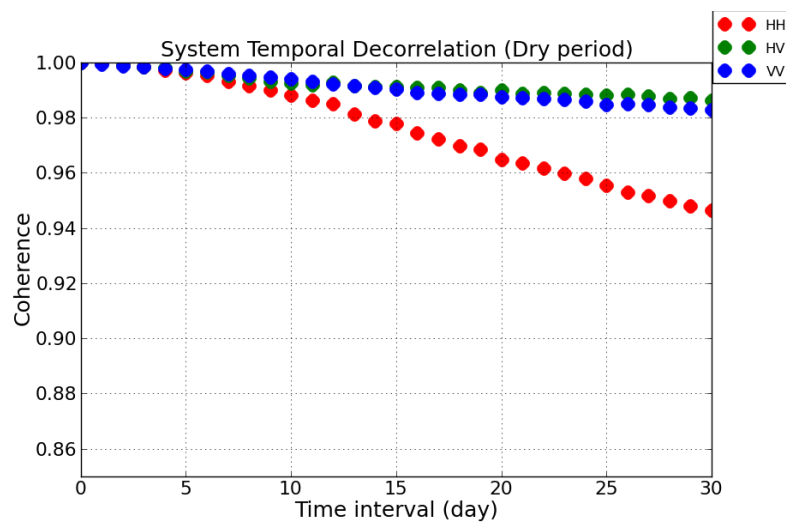


Figure 14 : System average coherence in the dry period and at 6 a.m.

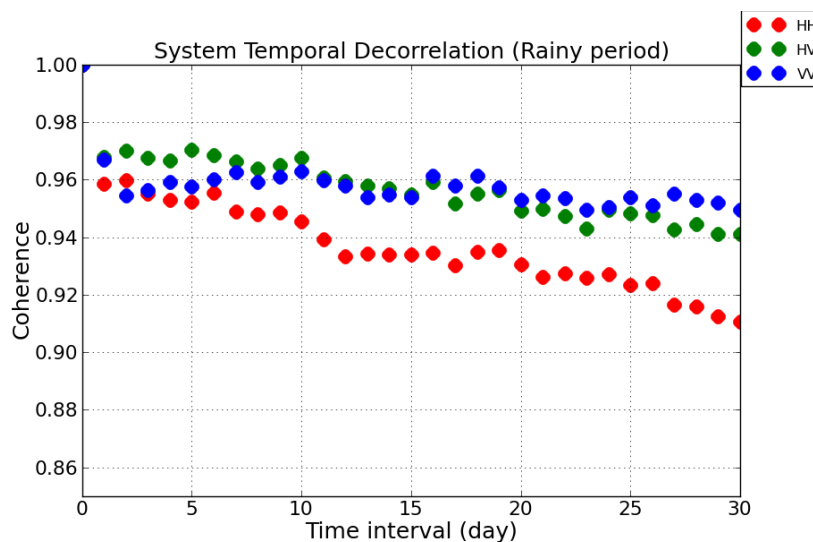


Figure 15: System average coherence in the rainy period and at 6 a.m.

These results will be used to remove the system coherence loss from the measurements in order to estimate the forest coherence only.

3.5.WP 15: TOMOGRAPHIC TESTS AND VALIDATION

The activity of PoliMi's team in French Guyana had been focused on checking the quality of the tomographic measurements made available since the beginning of October 2011 after installing the 20 antenna array depicted in the Experimental Plan document.

The first analyses were focused on tuning the tomographic processor according to the estimated delays due to the cables and the switchboxes.

Further analyses were carried out to get the Tomographic pulse responses in all polarizations. This has been made possible by employing a trihedral and a rotated dihedral reflector placed in front of the Guyaflux tower. Pulse responses have then been obtained by taking the difference between two acquisitions gathered with and without the reflectors, so as to remove contributions from the forests through coherent cancelation.

Finally, the tomogram quality has been analyzed as a function of the acquisition time, so as to derive preliminary information about the scene stability.

A side activity was focused on developing an automatic procedure for accessing the data based on acquisition time, frequency band, and polarization. The format for the acquisition name assumed in this section is the following:

Year – Month (1-12) – Day (1-31) Acquisition time (h-min) Frequency band (1,2,3) Polarization (HH,HV,VH,VV).

3.5.1. DELAY COMPENSATION

Signal delays associated with the hardware equipment result in spurious side lobes which affect the correct interpretation of the tomograms, and thus need to be compensated for during the tomographic processing. Delays due to cables connecting the array to the VNA are nominally the same for each antenna pair. It follows that their contributions is simply to induce a range offset in the resulting tomograms, as visible by comparing Figure 16 and Figure 17. The employment of two different switchboxes gives rise to more critical blurring phenomena, see Figure 18, due to the fact that antenna connected to different switchboxes experience different delays.

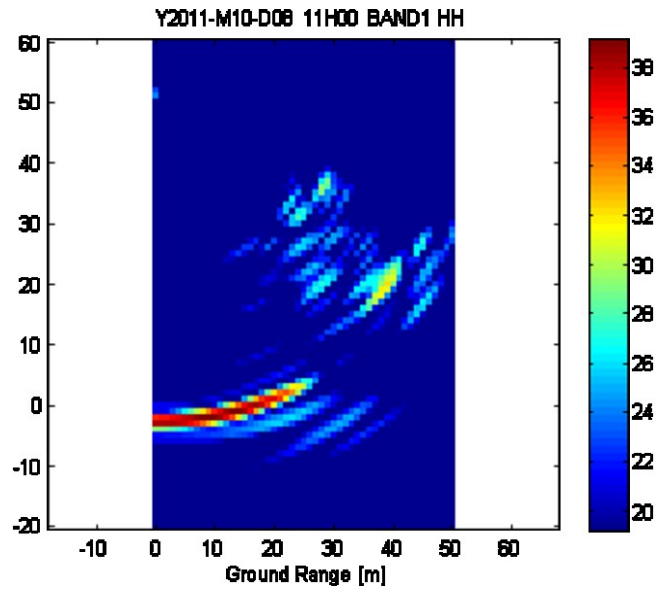


Figure 16: Tomogram after compensating for switch-box and cable delays. The scene includes the forest and the trihedral reflector

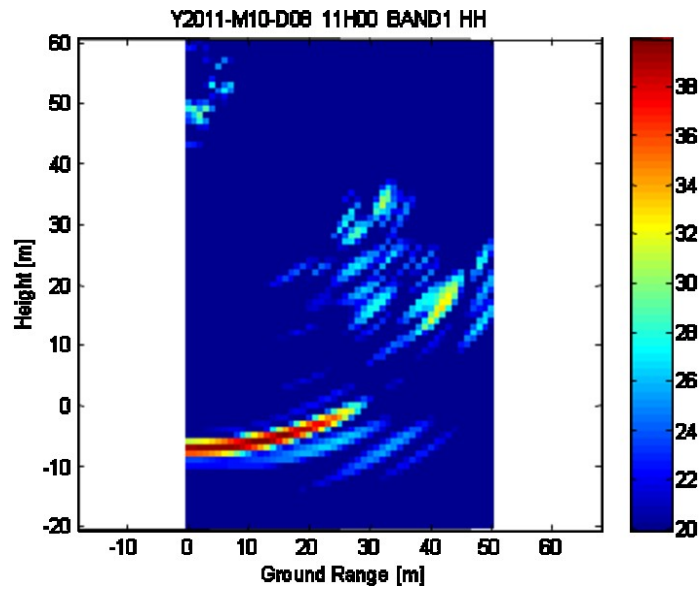


Figure 17: Tomogram after compensating for switch-box delays only. The scene includes the forest and the trihedral reflector

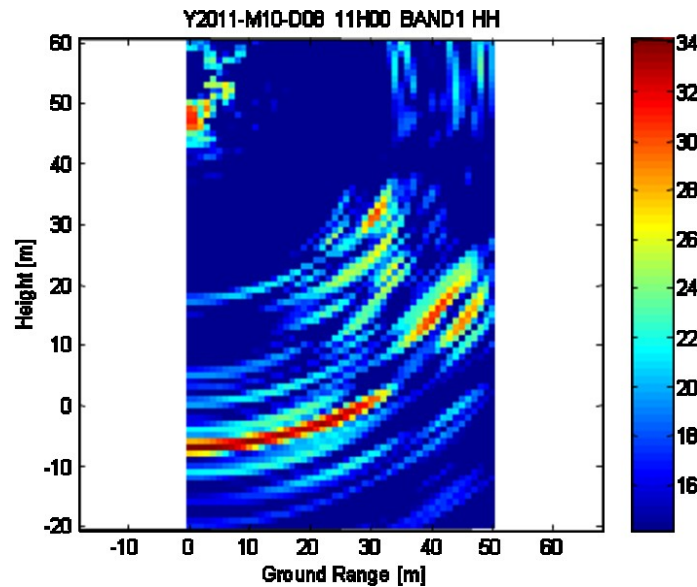


Figure 18 : Uncompensated tomogram. The scene includes the forest and the trihedral reflector.

3.5.2. PULSE RESPONSE

The tomographic responses of a trihedral and (rotated) dihedral reflector have been derived by taking the difference between the signals acquired with and without the reflectors, so as to remove forest contributions through coherent cancellation. The pulse responses for the trihedral reflector at 500 MHz, 700 MHz, and 900 MHz are reported in Figure 19, Figure 20, and Figure 21. The trihedral is observed to be very well visible in HH at all frequency bands at the same location in the ground range, height plane. As expected, the best angular resolution is achieved at 900 MHz, which provides the best accuracy concerning the localization of the target.

The corner is visible in VV polarization as well, even though signal backscattering coefficient is about 10 dB lower than in HH. Such a discrepancy appears to be due to the different antenna patterns for HH and VV at very steep incidence angles.

The trihedral reflector is partially visible in HV and VH, even though the signal amplitude appears to be comparable to that of residual contributions resulting from an imperfect cancellation of the forest.

The pulse response for HV and HV was recovered by exploiting a rotated dihedral reflector, for which the signal backscattering coefficient in cross-pol is observed to be significantly higher than forest contributions, see Figure 22.

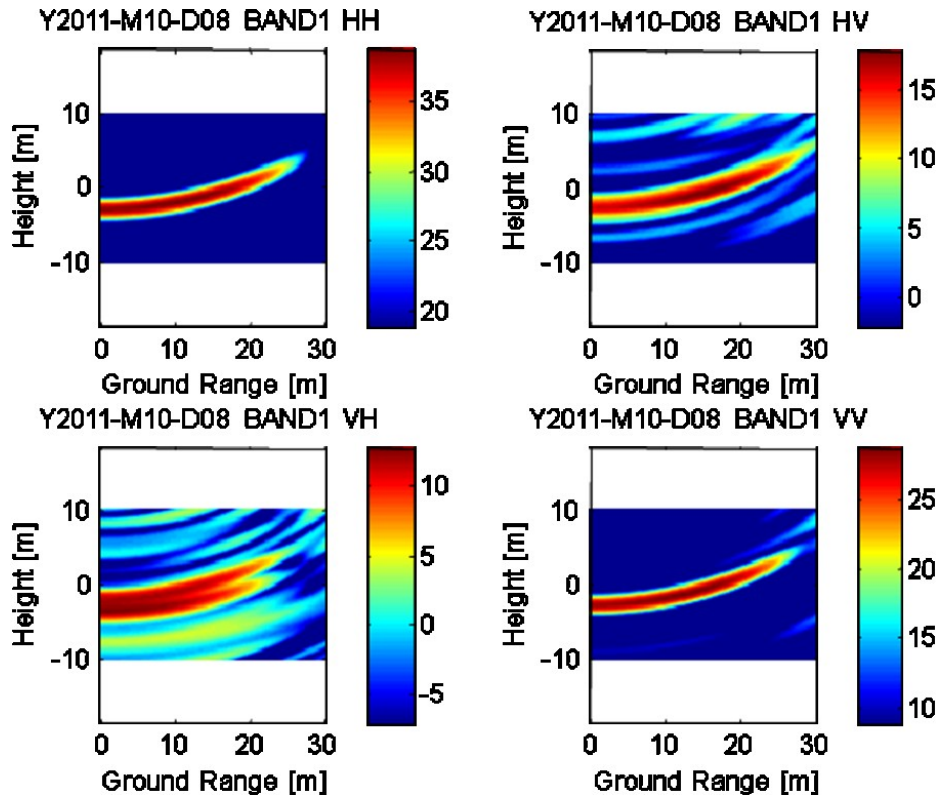


Figure 19: Tomographic pulse response for the trihedral reflector at 500 MHz.

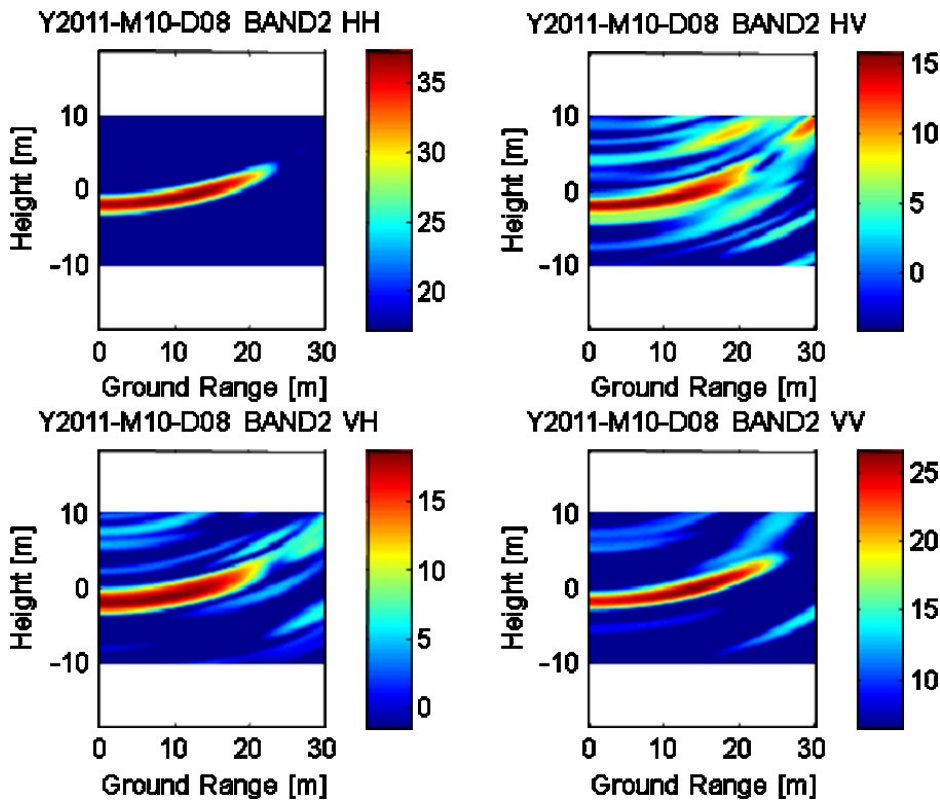


Figure 20: Tomographic pulse response for the trihedral reflector at 700 MHz.

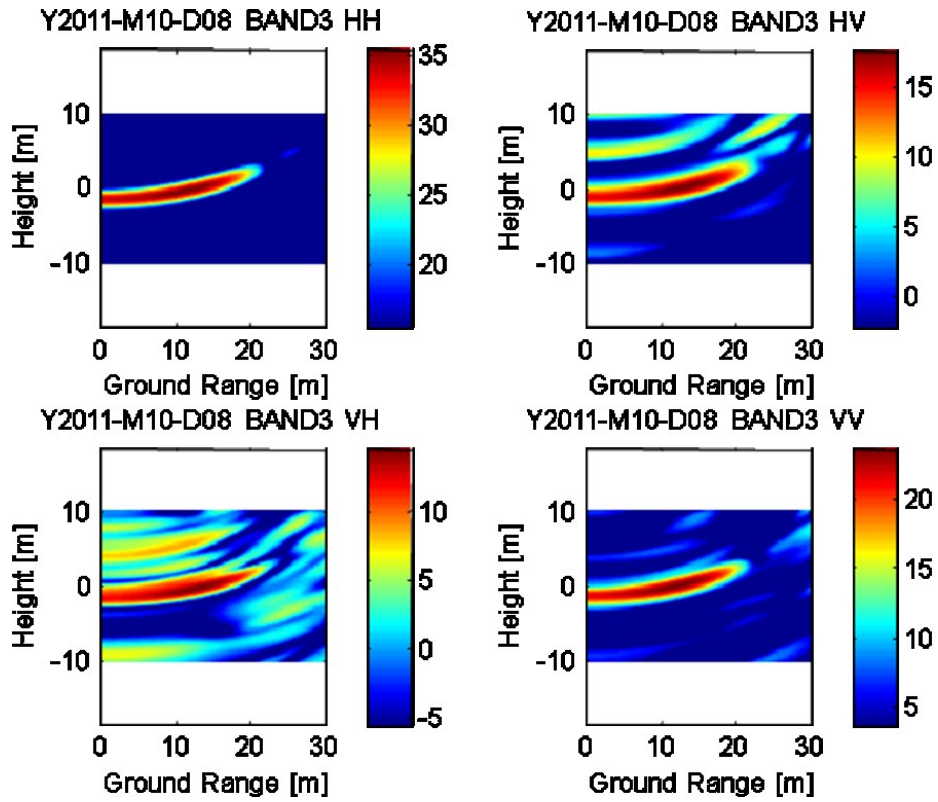


Figure 21: Tomographic pulse response for the trihedral reflector at 900 MHz.

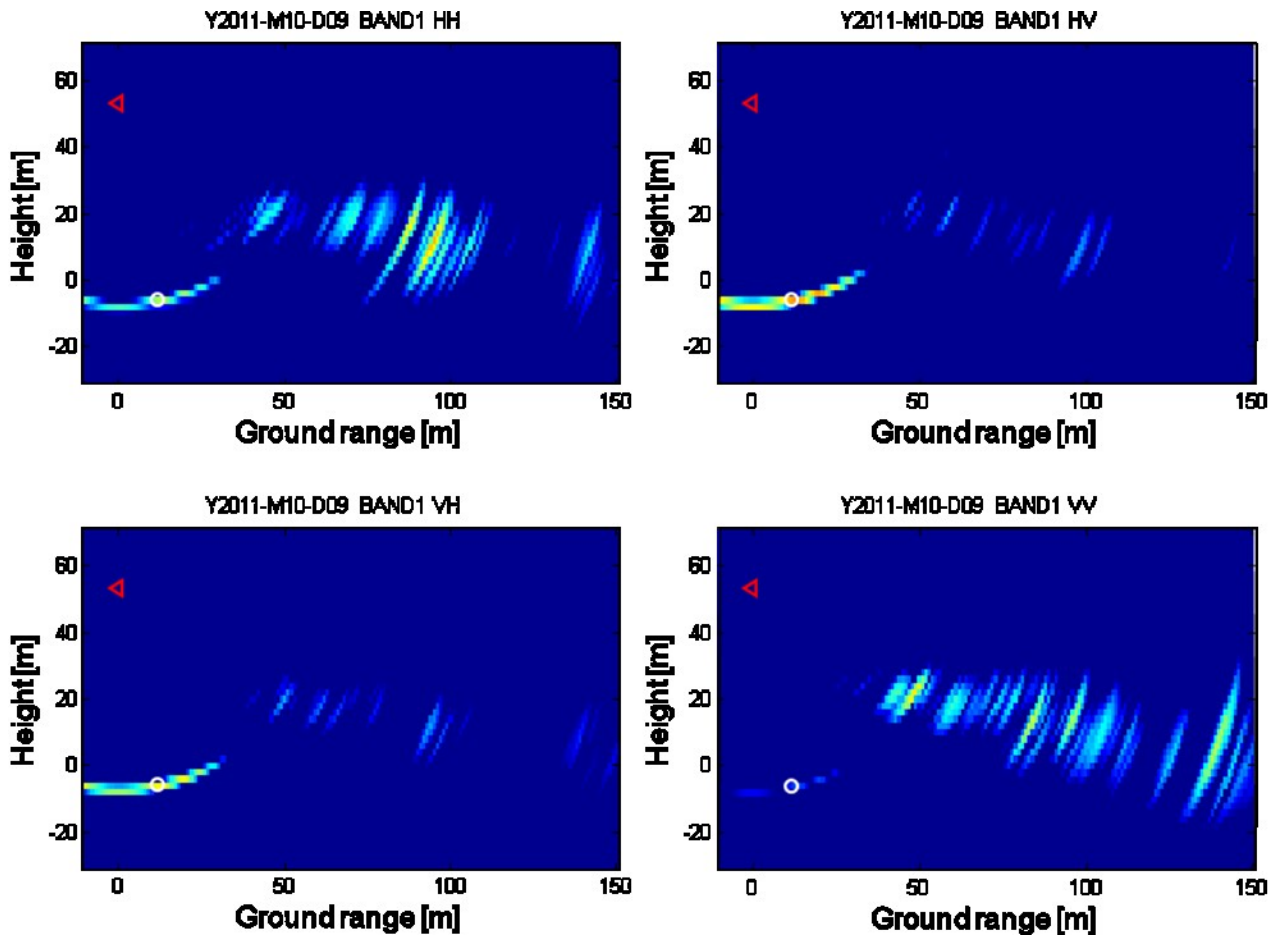
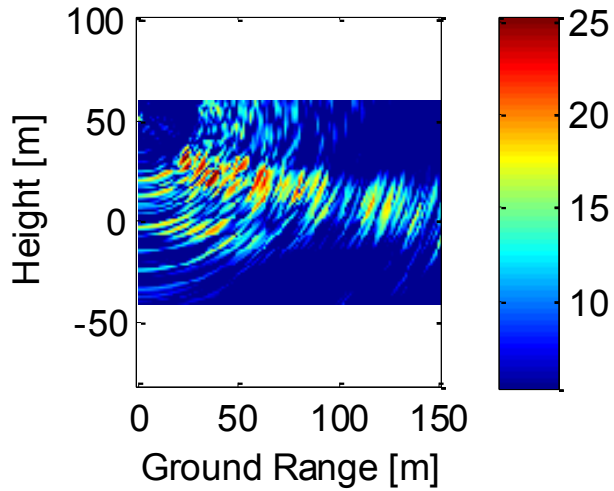


Figure 22: Tomographic pulse response for the dihedral reflector at 500 MHz.

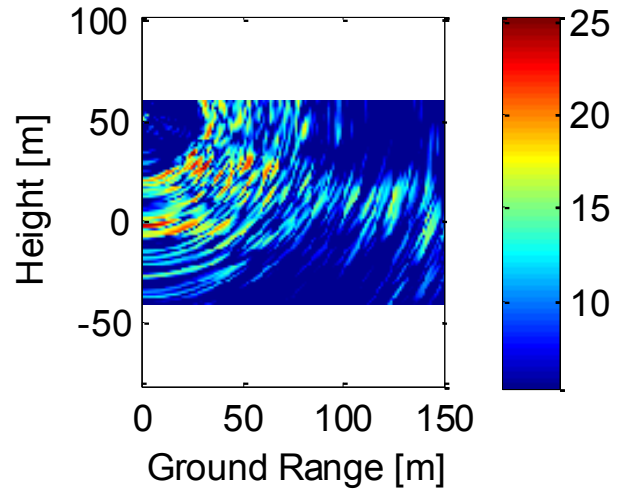
3.5.3. TOMOGRAM STABILITY AS A FUNCTION OF THE ACQUISITION TIME

Due to hardware constraints each tomographic acquisition is gathered over a time span of about 3, 4 minutes, which causes tomograms to be sensitive to fast motion of the forest induced by gusts of wind. Based on the examined data this phenomenon appears to be typical of late morning and afternoon hours, for which anomalous side-lobes are observed in the tomograms, see Figure 23. The scene appears to be more stable overnight, resulting in better focused tomograms see Figure 24.

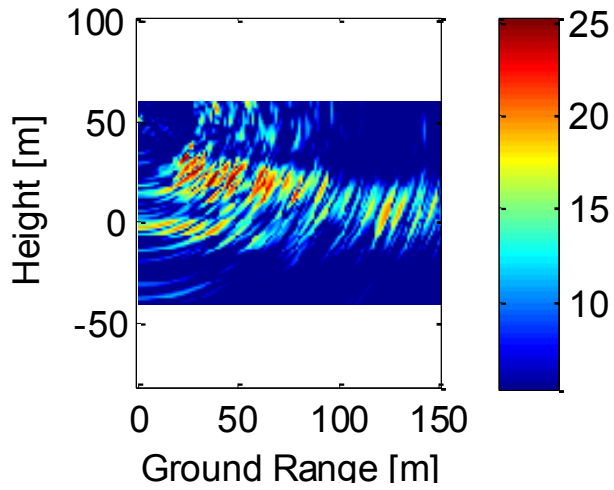
Y2011-M10-D07 13H00 BAND1 HV



Y2011-M10-D07 13H15 BAND1 HV



Y2011-M10-D07 13H30 BAND1 HV



Y2011-M10-D07 13H45 BAND1 HV

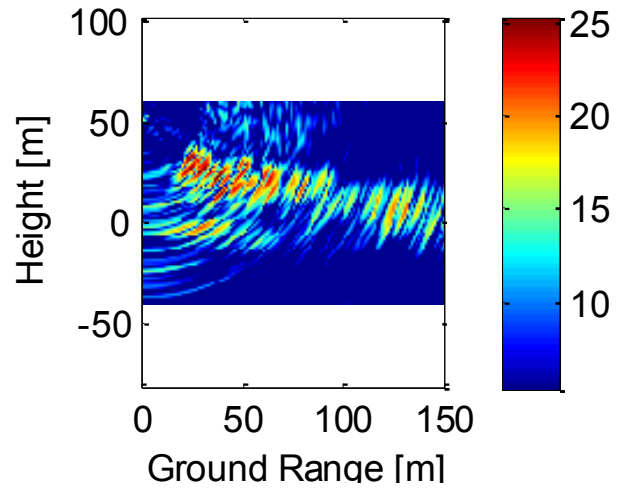
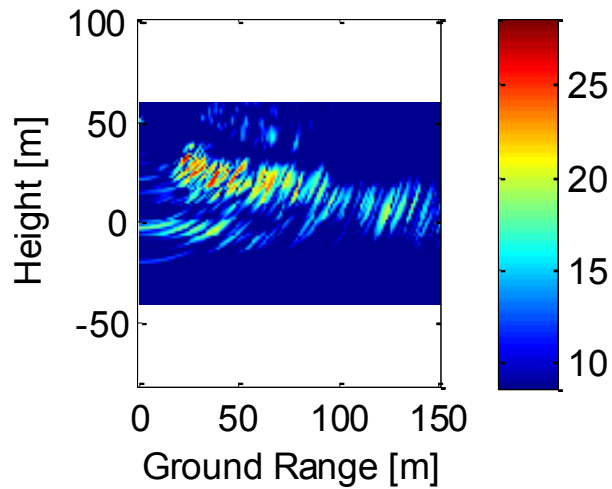
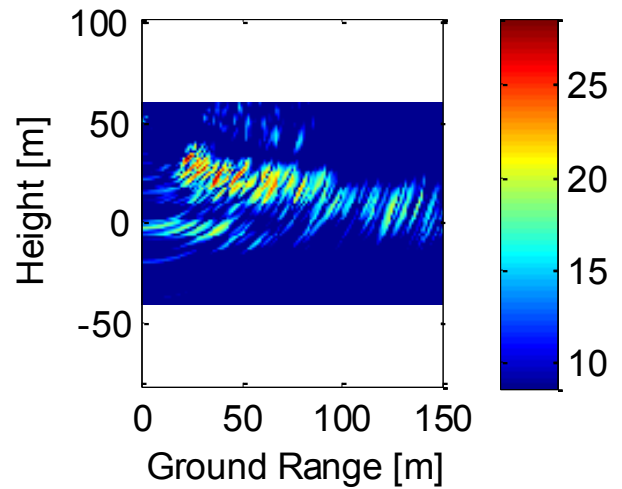


Figure 23: HV Tomograms gathered every 15 minutes from 13:00 to 13:45 .

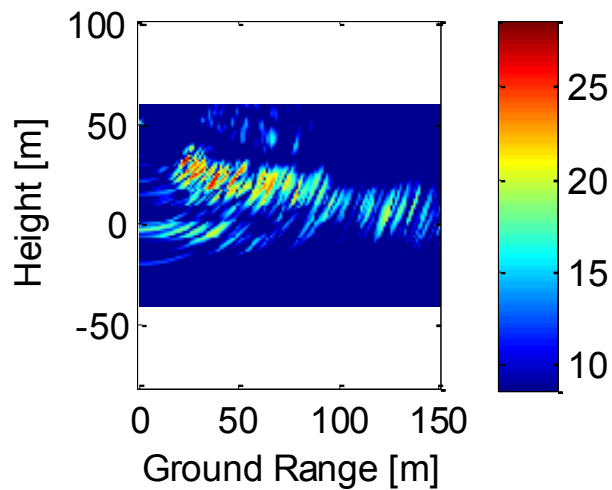
Y2011-M10-D07 01H00 BAND1 HV



Y2011-M10-D07 01H15 BAND1 HV



Y2011-M10-D07 01H30 BAND1 HV



Y2011-M10-D07 01H45 BAND1 HV

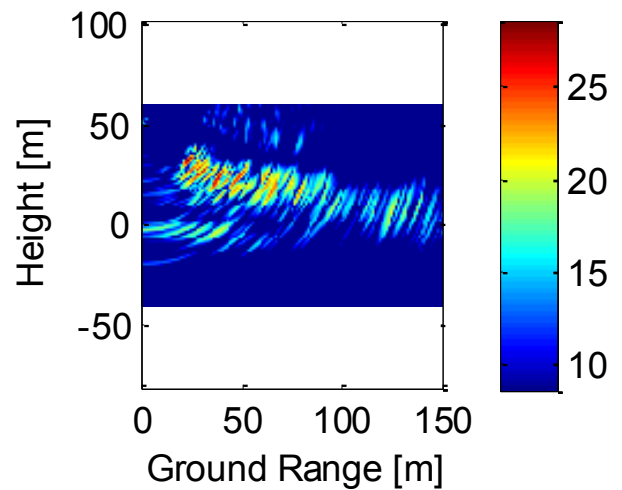


Figure 24: HV Tomograms gathered every 15 minutes from 1:00 to 1:45.

A simple and effective way to mitigate the impact of fast motions of the forest is to average a number of acquisitions gathered at nearby times. Significant side-lobe mitigation has been observed by averaging 4 acquisitions, as shown in Figure 25.

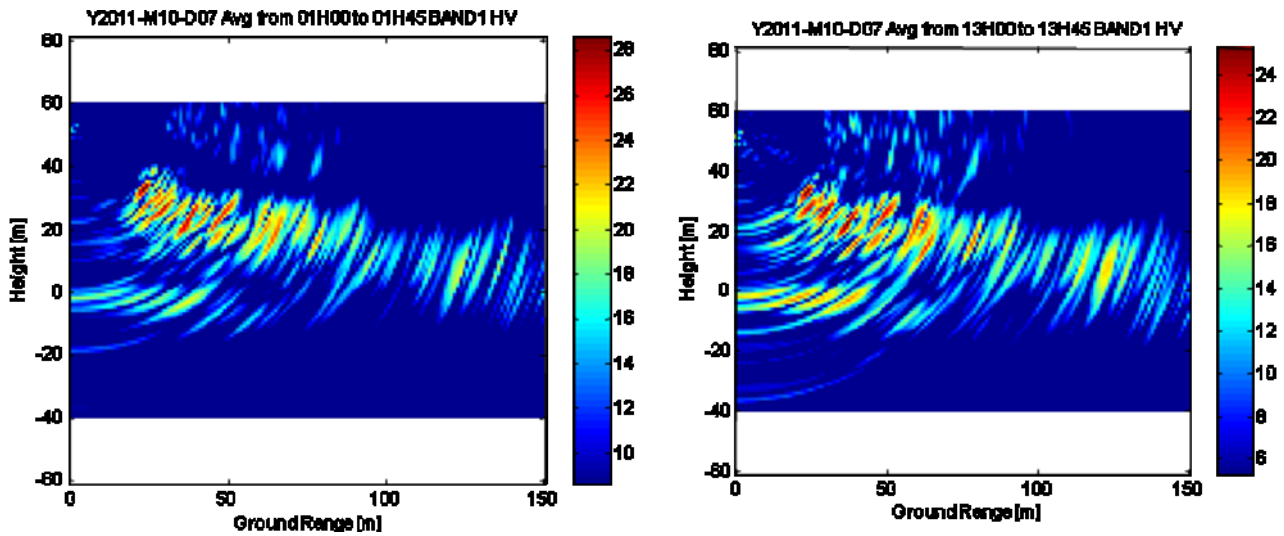


Figure 25: Averaged tomograms. Left: average from 1:00 to 1:45 . Right: average from 13:00 to 13:45

3.5.4. ANALYSIS OF TOWER STABILITY

Tower stability is a fundamental parameter to the aim of this experiment, as unwanted oscillations of the Radar equipment on top of the Guyaflux tower could be confused with motions within the vegetation layer. The stability analysis reported hereinafter is based on data collected in October 2011, when it was possible to install a corner reflector in front of the Guyaflux tower. Based on this analysis tower stability appears to be sufficient to carry out reliable measurements of the true temporal behavior of the forest.

The area is considered not very windy (wind speed < 5 m/s). However the wind pressure can generate small oscillating movements of the tower top. The amplitude of such movements is estimated to be less than 10 centimeters at worst with a temporal frequency of about 0.5 Hz. To assess the extent of tower motion we considered the time series obtained by taking the pixels in the focused tomograms corresponding to the positions of the trihedral reflector and the antenna array. Figure 26 reports the observed backscattering coefficient and Line of Sight (LOS) displacement, starting from October 7 2011 at midnight. LOS displacements have been obtained as:

$$dr = \varphi \cdot \frac{\lambda}{4\pi}$$

Equation 1

Where φ is the measured interferometric phase with respect to midnight and λ is the wavelength (0,6 m at P-Band).

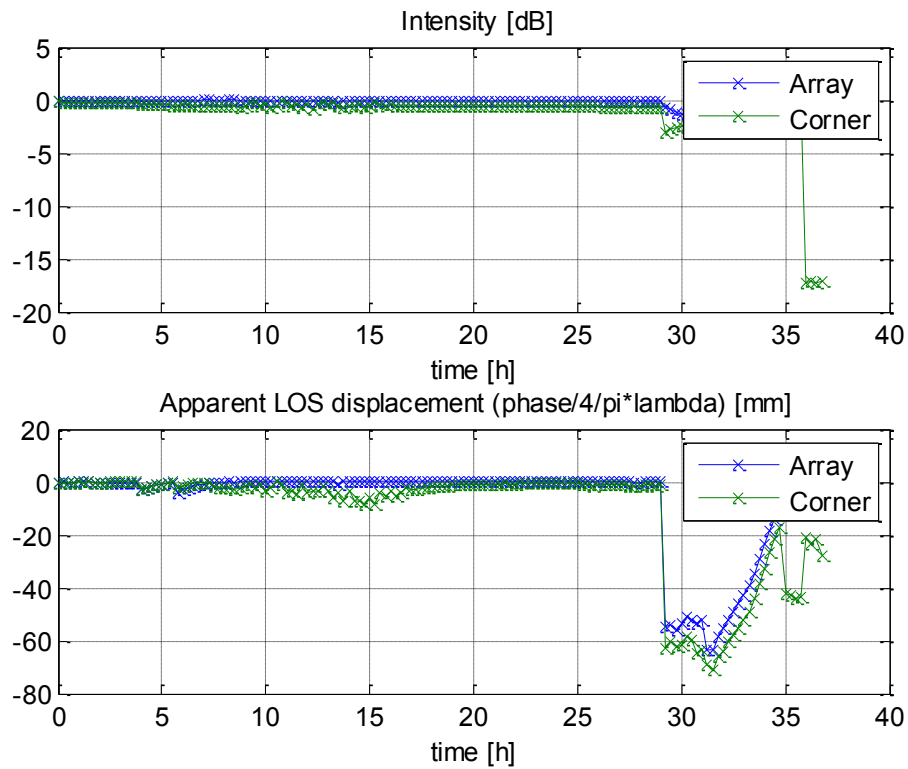


Figure 26: Top panel: backscattering coefficient (HH); bottom panel: apparent LOS displacement.

It is immediate to note an abrupt change took place slightly before 6 in the morning on day 8, corresponding to 30 hours from the starting time. Such an event is readily found to be associated with morning rain, see Figure 28. The impact of rainfall is even better observed by considering the change of the interferometric phase over time, as shown in Figure 27

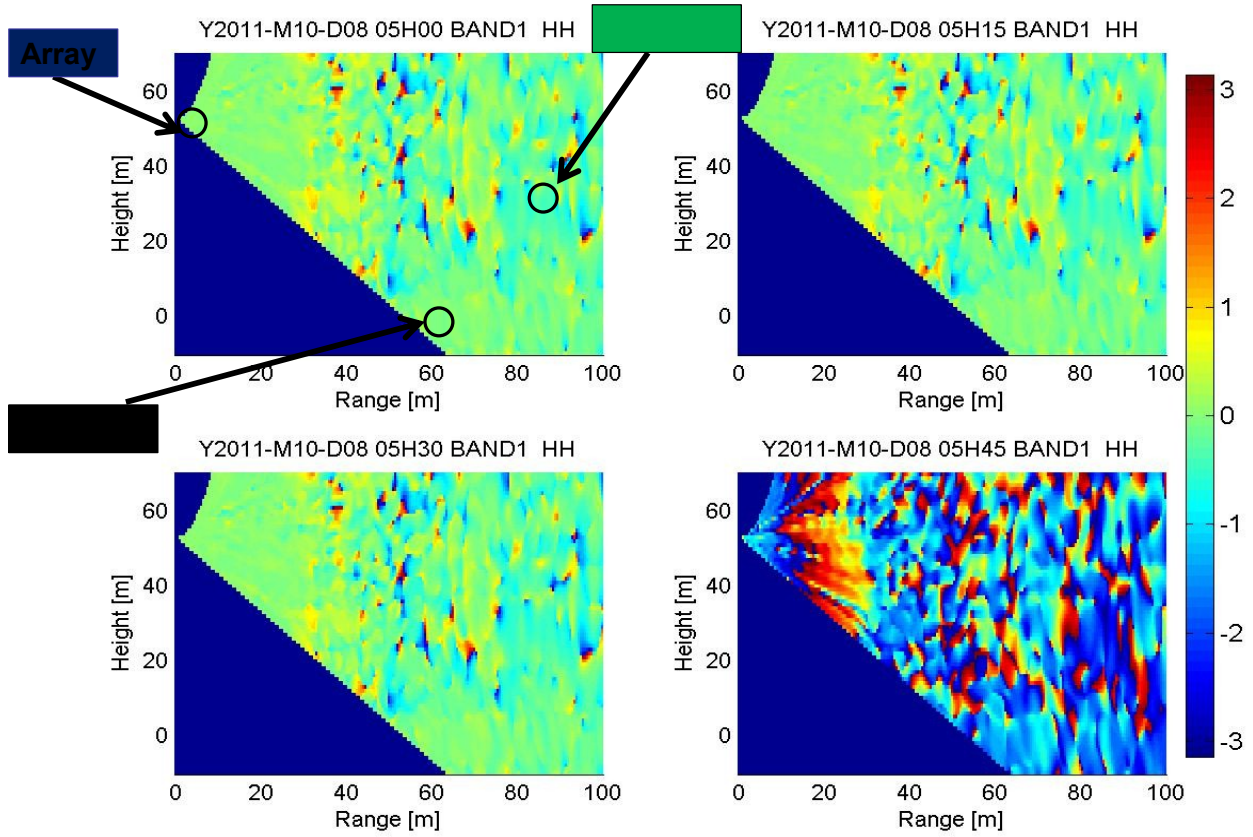


Figure 27: Interferometric phase with respect to midnight

The fact that the phase is modified by rain both at the corner and at the array indicates that rainfall affects the electromagnetic response of the equipment. Accordingly, data acquired during rainfalls should be neglected in evaluating the temporal behavior of the forest.

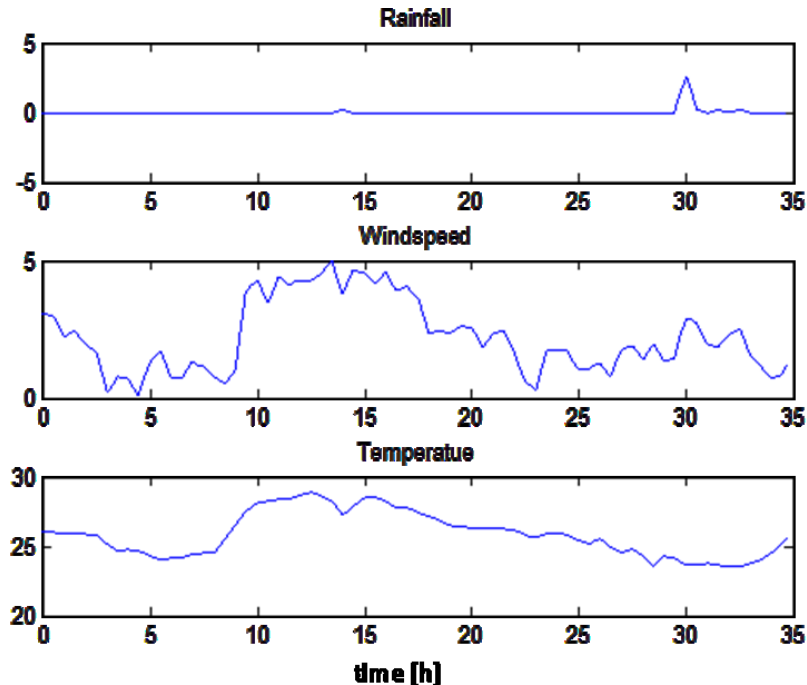


Figure 28: weather data from October 7 at midnight.

A closer look to array and corner apparent motion is reported in Figure 29 where rainfall times are not considered. Three different phase behaviors are observed:

- From 4 to 6 in the morning there two phase peaks both at the corner and at the array. The observed trend is about 2 mm in LOS motion, but no oscillations are observed.
- From 9 to 16 the corner phase is observed to have a trend of about 8 mm plus a number of phase oscillations (< 1 mm). No relevant change is observed concerning the array phase.
- During most night hours the phase histories at both the array and the corner exhibit an excellent stability.

Concerning the motion of the antenna array under the action of the wind, two effects are expected. The first is a rigid translation due to a slight leaning of the tower top under the effect of a constant wind. This motion has no effect on the quality of tomographic imaging, as it would just result in a very slight image translation. The other effect is associated with random horizontal oscillations due to varying wind speed. This kind of motion can potentially degrade image quality due to the fact that tomographic focusing is carried out by processing data acquired by 15 different antenna pairs, the time lag between one pair and another being on the order of 30 seconds.

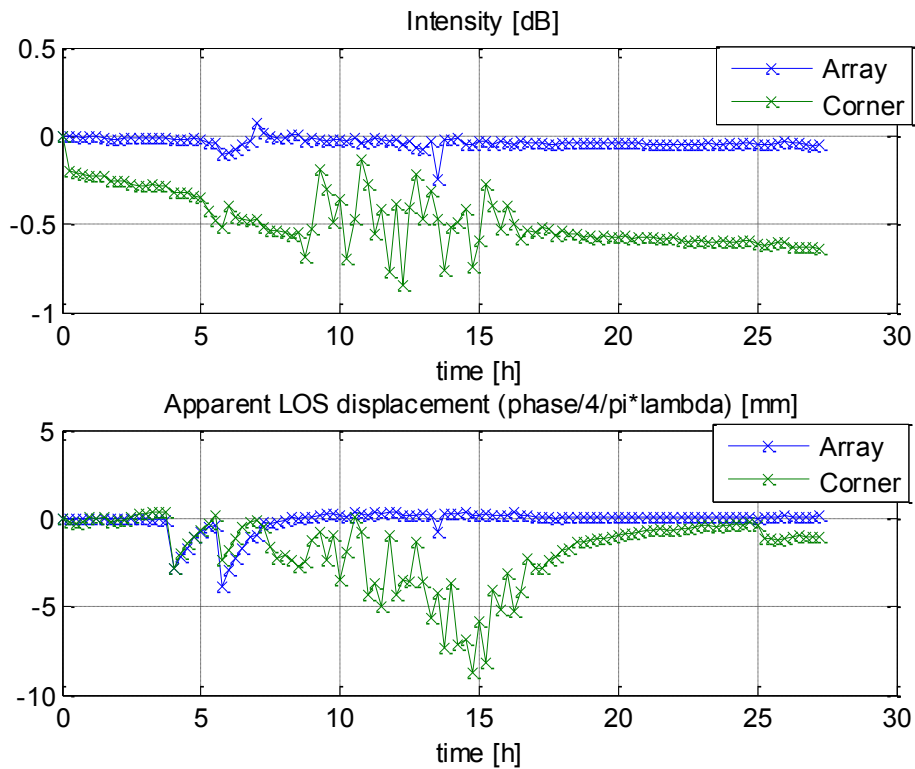


Figure 29: Top panel: backscattering coefficient (HH); bottom panel: apparent LOS displacement.

Assuming the observed oscillations in the corner phase histories are due to horizontal motions of the tower, the standard deviation of the latter can be obtained as:

$$\sigma_x = \frac{\sigma_r}{\sin \theta} \sqrt{15}$$

Equation 2

Where σ_r is the standard deviation of LOS motion, θ is the incidence angle at the corner position, and the factor $\sqrt{15}$ accounts for the fact that 15 antenna pairs are used in the tomographic focusing.

The result is shown in Figure 30. A peak value on the order of 4 cm is found during day time, when wind speed is at its maximum (5 m/s), whereas the average value during night time is 1 cm or less. Such a value is consistent with the one assessed in the Experimental Plan Document (< 5 cm), which was shown not to be critical for the tomographic imaging quality.

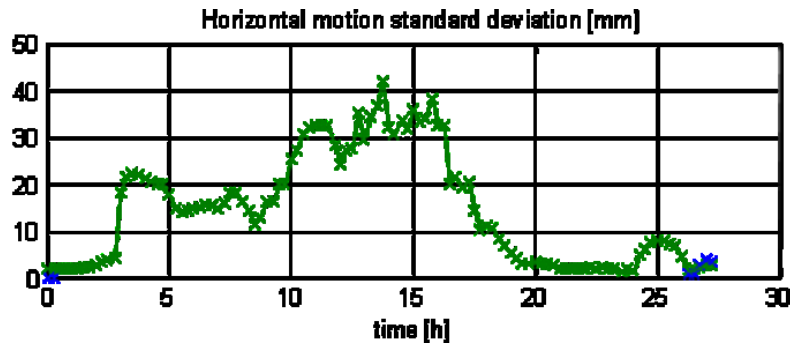


Figure 30: standard deviation of horizontal tower motion, as predicted based on the corner phase history.

To provide a further demonstration that such a motion does not jeopardize image quality we simulated the effect of random motion errors about the sensor positions on data focusing. To do this we considered real HH data acquired at midnight (Y2011-M12-D15 00H00) and used it to produce two synthetic raw data by injecting a Gaussian random displacement with zero mean and standard deviation equal to 2.5 cm and 5 cm, respectively. The raw data are then focused in all cases assuming the tower is perfectly still. Results are presented in Figure 31.

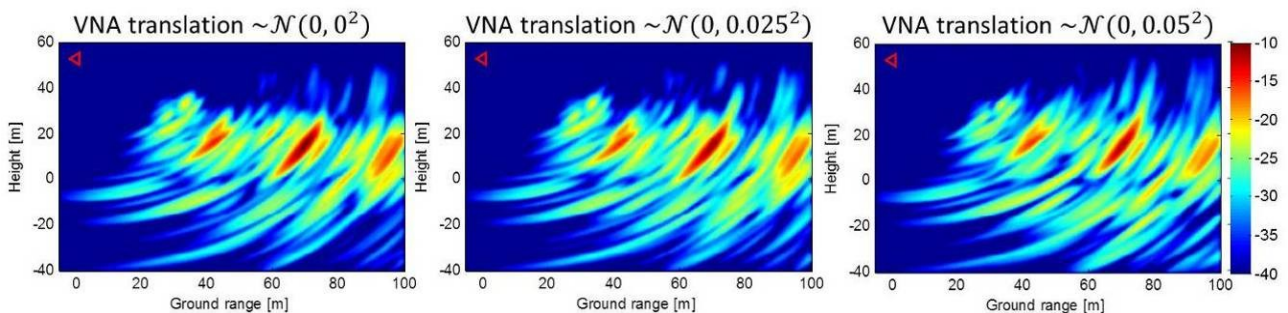


Figure 31: The effects of tower motion to the tomographic imaging.

It is important to observe that image quality is fully preserved, even in the worst case scenario where the tower moves randomly by 5 cm. As discussed above this value was derived by assuming that the observed corner phase variations are entirely due to tower motions, therefore providing a worst case upper bound for tower motions. It is also worth noting that in the rare case of such a strong wind as to induce very large tower motions (> 5 cm) the forest would be heavily shaken too, giving unavoidably rise to relevant temporal decorrelation phenomena. Based on this analysis, we then conclude that defocusing phenomena observed during daytime can be safely imputed to forest motion under the action of wind. Moreover, the excellent tower stability during night hours confirms the feasibility of yielding accurate measurements of the forest temporal decorrelation, with the one precaution to exclude rainfalls from the analysis.

3.5.5. CONCLUSIONS

The analyses carried out on the data gathered in the first part of the TropiScat experiment fully confirmed the feasibility of retrieving accurate information about the forest vertical structure through tomographic imaging.

System delays have been accurately compensated for based on external information, i.e.: no attempt has been made to estimate the delays directly from the data. The quality of the pulse responses for the trihedral

and dihedral reflectors indicates that external information is already sufficient to ensure accurate tomographic imaging.

The motion of the forest induced by gusts of wind during the time required for each tomographic acquisition (about 3, 4 minutes) has been observed to result in unwanted side-lobes which hinder physical interpretation. Such a phenomenon has been observed to occur mainly during day-time, whereas night acquisitions appear to be more stable. The impact of wind-induced motions of the forest has been observed to be strongly mitigated by averaging tomograms over one hour, corresponding to four acquisitions. Concerning the study of temporal coherence, which is the main goal of the TropiScat campaign, averaging tomograms entails that the temporal analysis is limited to the part of the forest that stays stable over the averaging time (say one hour), moving components being rejected by the averaging process. Tomogram averaging then appears to be well suited to study all decorrelation phenomena characterized by a dynamic slower than the averaging time, such as changes in humidity and vegetation growth, while rejecting the impulsive effect due to gusts of wind.

Tower stability against wind gusts has been evaluated based on the phase histories at the corner reflector. Based on this analysis, tower motion is at most 4 cm, which is consistent with the value assumed in the Experimental Plan Document, we can conclude that the defocusing phenomena observed during daytime can be safely imputed to forest motion under the action of wind, as discussed above. Moreover, the excellent tower stability during night hours confirms the feasibility of yielding accurate measurements of the forest temporal decorrelation, with the one precaution to exclude rainfalls from the analysis.

4. WP 20: DATA ACQUISITION

4.1.WP 21: DATA PRE-PROCESSING & QUALITY ASSESSMENT

Raw data are pre-processed in order to check the instrument health and the quality of the data.

During the validation phase, it was shown that rainfall affects the electromagnetic response of the equipment (the phase is modified). As a consequence, to ensure a good quality of the analysis, data acquired during rain are flagged and should be avoided.

During the experiment, some important events occur, disturbing the acquisition schedule:

- In November-December 2011, quality analyses showed strong disturbances during and after rainfalls. In order to assess the effect of rainfalls on equipment, ONERA has carried out laboratory experiments. During heavy rains, water enters in the antenna and was not able to flow out because of silicon paste. This silicon paste is efficient in case of light rain, to prevent water to leak inside the antenna. But in case of heavy rain, a small part of the water goes inside the antenna and was stored there during many days. After several rainy days, the stored water has electrically shortened the antenna feeding system, affecting strongly the antenna gain.
- In April 2012, one RF switch broke down. After 4 millions of switching, in tropical environment, the device did not respond to the command. As a consequence, only 2 polarizations were still working.
- In May 2012, The Vector Network Analyzer broke down. Internal hard disk and electronic card were out of order. Investigations showed that the main cause was an electrical power failure of the Paracou installation. This problem caused 3 months of interruption of data acquisitions.

The processing of the data is described in 5.1.1

4.2.WP 22: IN-SITU DATA

In-situ data have been provided by the INRA sensors. INRA team sent us weather data every 45 days. In-situ data collected during the experiment are summarized in the Data Acquisition Report [RD 2]. They include:

- Temperature (°C) & relative hygrometry (%) @ 2 meters, 30 meters and 55 meters from ground
- Soil temperature (°C) @ -3 cm, - 18 cm, -33 cm and -53 cm above ground
- Soil moisture @ -3 cm, - 18 cm, -33 cm and -53 cm above ground
- Atmospheric pressure (mm Hg)
- Wind direction and speed (m/s)
- Rain level (mm)
- Total incident radiation (W/m²) and total reflected radiation (W/m²)
- IR incident radiation (W/m²) and IR reflected radiation (W/m²)
- PAR (Photosynthetic Active Radiation) incident radiation (W/m²) and PAR reflected radiation (W/m²)

All these measurements are available every 30 minutes. Each measurement data is an average of 30 measures performed every one minute. All in-situ data are stored in the database for use in data processing.

5. WP 30: DATA PROCESSING AND ANALYSIS

5.1.WP 31: TEMPORAL COHERENCE DATA PROCESSING

5.1.1. OVERVIEW OF DATA PROCESSING

The objective of WP31 is to analyze the temporal variations of the polarimetric coherence at P-band over a tropical forest. Measurements at P band (400MHz to 600 MHz) focusing on the individual impulse responses are done every 15 minutes. .

The measurement are performed in the frequency domain then transformed into the time domain or equivalent range domain by IFFT (Inverse Fast Fourier Transform). So, for each acquisition we obtain a complex impulse response. If Δf and ∂f are respectively the frequency bandwidth and the frequency step,

with $\Delta f = (Nf - 1) \times \partial f$, then the range resolution is $dr = \frac{c}{2\Delta f}$ and the unambiguous range $D = \frac{c}{2\partial f}$. So,

for the range $i.dr$, the range profile is defined by the complex array $S(i) = (X(i), Y(i))$ where "i" is the i_{th} range bin, and dr is the width of range bin.

The raw data collected during the TropiScat campaign are must be processed before use for temporal coherence estimation. First, the antenna gain is accounted for.

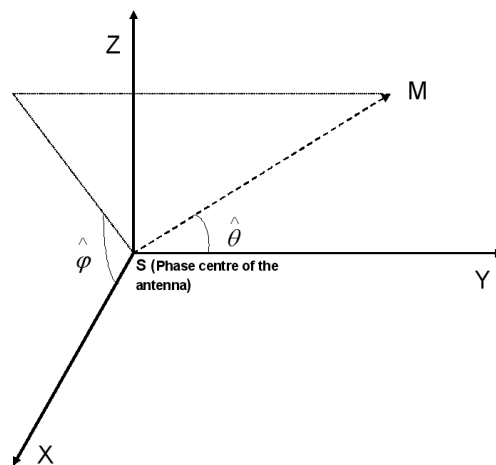


Figure 32: Coordinate system of the antenna

Figure 32 represents the coordinate system of the antenna $(SXYZ)$, $\hat{\theta}$ and $\hat{\varphi}$ are respectively the elevation and the azimuth angle. Considering Figure 32, the plane $\hat{\varphi} = \frac{\Pi}{2}$ is the elevation plane and $\hat{\varphi} = 0$ is the azimuth one.

The gain in the coordinate system of the antenna is given by Equation 3.

$$G'(\hat{\theta}, \hat{\varphi}) = G_{\max} - 3 \frac{\hat{\theta}^2}{\theta_3^2}$$

Equation 3

Where G_{\max} represents the maximum gain of the antenna and θ_3 corresponds to 3 dB aperture and it is given by Equation 4

$$\theta_3 = \theta_{3_{elev}} \cdot \cos^2\left(\hat{\varphi} - \frac{\pi}{2}\right) + \theta_{3_{az}} \sin^2\left(\hat{\varphi} - \frac{\pi}{2}\right)$$

Equation 4

Where $\theta_{3_{elev}}$ corresponds to 3 dB aperture in the H plane for H polarisation and in the E plane for V polarisation, whereas $\theta_{3_{az}}$ corresponds to 3 dB aperture in the H plane for V polarisation and in the E plane for H polarisation.

On the other hand, in the coordinate system $(Oxyz)$ tied to the soil as horizontal plane (Oxy) and to the tower axis (Oz) , an observation point M is in spherical coordinates defined by (r, θ, φ) . These coordinates depend on $\hat{\theta}$ and $\hat{\varphi}$ as follows (Equation 5):

$$\cos \hat{\theta} = \sin \theta \sin \varphi \sin \theta_0 + \cos \theta \cos \theta_0$$

$$\cos \hat{\varphi} = \frac{\sin \theta \cos \varphi}{\sin \hat{\theta}}$$

$$\sin \hat{\varphi} = \frac{\sin \theta \sin \varphi \cos \theta_0 - \cos \theta \sin \theta_0}{\sin \hat{\theta}}$$

Equation 5

Where θ_0 is the direction of maximum radiation, θ and φ are respectively the elevation and the azimuth angle in the $(Oxyz)$ coordinate system (Figure 33:).

The raw data are calibrated with a trihedral reflector as expound in Figure 4. As the presence of the corner reflector may disturb the forest response, its measurements have been done at particular time slots with locating it on the forest ground with a quite clear line of sight from the tower top. Its contribution was evaluated with time gating and clutter removal with complex subtraction which appeared to be fully efficient for more than 30 minutes.

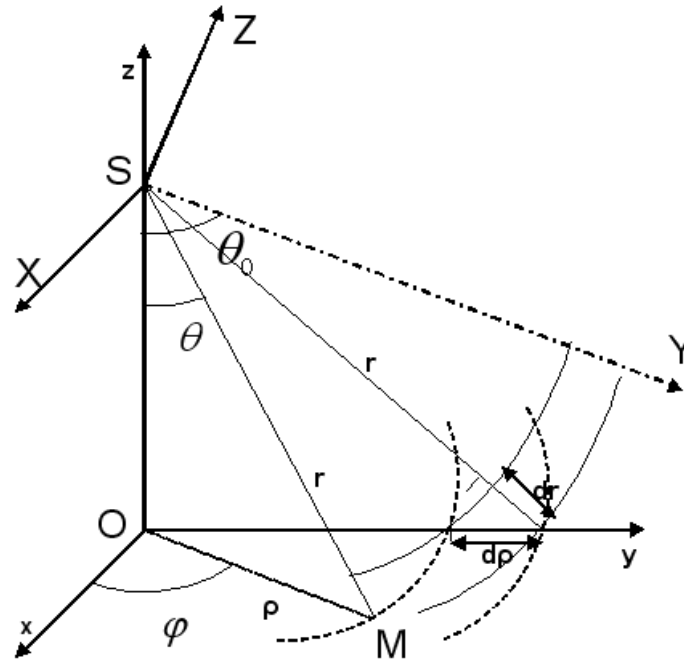


Figure 33: Antenna-ground geometry and illuminated surface projected on ground

For the forest, it is to evaluate the weighted illuminated area I_{pq} for a given range cell.

Let $G(\theta, \varphi) = G'(\hat{\theta}, \hat{\varphi})$

$$I_{pq} = \int_{\varphi=0}^{\varphi=\pi} G_e(\theta, \varphi) G_r(\theta, \varphi) \rho d\rho d\varphi = \int_{\varphi=0}^{\varphi=\pi} G'_e(\hat{\theta}(\theta, \varphi), \hat{\varphi}(\theta, \varphi)) G'_r(\hat{\theta}(\theta, \varphi), \hat{\varphi}(\theta, \varphi)) r dr d\varphi$$

Equation 6

As $\rho d\rho = r dr$, with ρ the distance from the soil to the bottom tower axis,

and with $p = \left| \frac{H}{V} \right|$ and $q = \left| \frac{H}{V} \right|$, G_e the emission gain, G_r the reception gain.

Note that it was delicate to position the trihedral reflector because of the forest presence. So this introduces some uncertainty related to the calibration. Or this point is not critic because only a relative calibration is required here to perform temporal monitoring. However, such calibration allows normalization between polarizations and antennas pairs.

Another correction was made in order to adjust the impulse response. In fact, it was noted that the direct coupling between antennas may be subject to some changes with time in particular during the rainy period. However this direct coupling is supposed to be constant. Consequently, we have established a method to adjust data that corrects this effect and normalize the level of direct coupling between antennas at a constant level. In fact, the hypothesis that a change in the antenna gain is fully characterized by the coupling change is done.

To do this, an impulse response measured at dry time is chosen and considered as a reference $S'_{ref} = (X'_{ref}, Y'_{ref})$. All impulse responses include the antennas direct coupling, the tower coupling and the forest response as displayed in (Figure 34:).

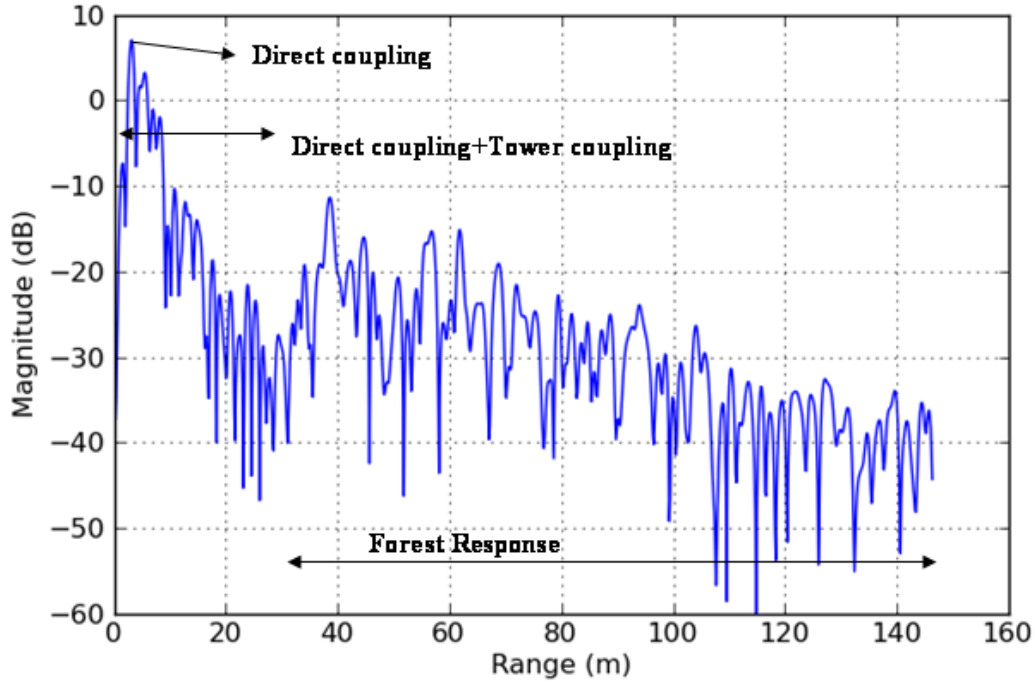


Figure 34: The backscattered impulse response

For all impulse responses $S'(i)_t = (X'(i)_t, Y'(i)_t)$, the real and imaginary parts are corrected as follows:

$$X_{pqt}(i) = X'_{pqt}(i) \cdot \frac{C_{pqref}}{C_{pqt}} \quad \text{and} \quad Y_{pqt}(i) = Y'_{pqt}(i) \cdot \frac{C_{pqref}}{C_{pqt}}$$

Equation 7

Where, by averaging the power around the direct coupling peak over N cells, we have:

$$C_{pqref} = \sqrt{\frac{\sum_{i_{max}-\Delta N_i/2}^{i_{max}+\Delta N_i/2} (X'_{pqref}{}^2 + Y'_{pqref}{}^2)}{N}} \quad ; \quad C_{pqt} = \sqrt{\frac{\sum_{i_{max}-\Delta N_i/2}^{i_{max}+\Delta N_i/2} (X'_{pqt}{}^2 + Y'_{pqt}{}^2)}{N}}$$

Equation 8

where $p = \left| \frac{H}{V} \right|$, $q = \left| \frac{H}{V} \right|$, i_{max} is the index of coupling peak, Δ_i is the number cells around the i_{max} , $N = \Delta N_i + 1$.

Furthermore, it was noted that the direct coupling between antennas can be subject to changes during the rainy period. We have established a method to correct this effect by normalizing the level of direct coupling between antennas at the same level as a reference level chosen in the dry period [Hamadi et al., 2013a] and [Hamadi et al., 2013b].

5.1.2. TEMPORAL COHERENCE

TEMPORAL COHERENCE COMPUTATION

The temporal coherence is an indicator of the change in forest backscattering between two measurements made at two different times. The short-term variations are due to the wind movement, rain fall, soil moisture and long-term variations include the growth of the forest, cumulative rain fall, vegetation and soil moisture... In this section, we study the variations of the temporal coherence at different time scales and assess the link of these variations to the weather parameters which are wind speed and rain fall.

Considering simultaneously K antenna pairs illuminating the same range gate, the temporal complex coherence coefficient between the backscattered signals S_2 at t_2 and S_1 at t_1 is given by (eq. 7).

$$\gamma_{pq} = \frac{\sum_{k=1}^K \sum_{i_{\min}}^{i_{\max}} S_{1\ pq}^k(i) \cdot S_{2\ pq}^k(i)^*}{\sqrt{\sum_{k=1}^K \sum_{i_{\min}}^{i_{\max}} |S_{1\ pq}^k(i)|^2 \sum_{k=1}^K \sum_{i_{\min}}^{i_{\max}} |S_{2\ pq}^k(i)|^2}}$$

Equation 9

with $p = \begin{matrix} H \\ V \end{matrix}$ and $q = \begin{matrix} H \\ V \end{matrix}$, i_{\min} and i_{\max} correspond to the limits of the range gate under consideration, k refers to the considered antenna pair, K is the total number of antenna pairs taken in consideration. Actually, in Equation 9, the range cells of the impulse responses several antenna pairs' are combined and incorporated in a single complex vector. The time interval t_2-t_1 is the temporal baseline. In the following, coherence will refer to the modulus of the complex coherence coefficient.

To obtain a good estimation of the coherence, a minimum number of independent looks is necessary [Touzi et al., 1999]. This number can be provided by the number of spatial resolutions within the measured area, and also by the number of antenna pairs. An increasing number of antenna pairs was tested. To assess the stability of the measurements, we choose a spatial zone limited between 45 m to 60 m starting from the tower basis, corresponding to an incidence angle on the forest of about 44° . Within this area, there are 15 range cells of the size of spatial resolution (about 1m including the apodization factor) per antenna pair.

Figure 35 shows the coherence variation versus the number of antenna pairs. The coherence is computed between the signal at a given reference date and time of the day and the acquired signal with a temporal sampling of 15 minutes, and for a given number K of antenna pairs, is averaged over one month.

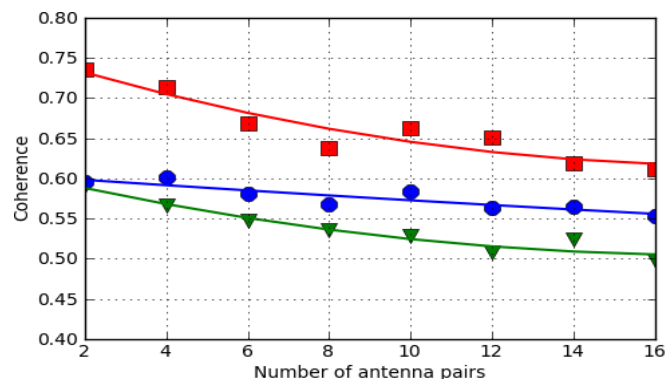


Figure 35: Coherence variation versus the number of antenna pairs for the HH, HV and VV polarization

Figure 35 shows that average coherence versus the number of antenna pairs. The analysis shows that the stability is observed for a number of antenna pair higher than 12, for the 3 polarization. In the following, the 16 antenna pairs will be used for computing the coherence at a given time.

The range profiles have been normalized to account for the variation with range of the propagation losses, the antenna gain and the intercepted soil surface [5.1.1] and corrected in range so that the footprint is the same for all antennas sets. Note that the coherences plotted here underestimate the coherence of the scene since they incorporate the decorrelation due to the instrument itself.

DAILY CYCLE COHERENCE

To better understand the variation of the P-band coherence on the tropical forest with respect to the principal sources of decorrelation, we begin with the daily cycle of the coherence. In the analysis, we distinguish measurements from 'volume only' and measurements from 'full forest'. For that, signal corresponding to ranges less than 55 m which do not intercept the ground level and will be called in the following as 'volume only'. When the ranges are greater than 55 m, both forest volume and underlying ground are intercepted and in this case we will refer to 'full forest'. In the following, detailed diurnal variations of the coherence every 15 minutes in two days (from 22/09/2012 to 24/09/2012) during the dry period are analyzed. To compute the coherence, two time references were chosen. Figure 36 shows the coherence of the full forest with the reference at midnight, and Figure 37 with the reference at 6 a.m. Figure 38 shows the coherence of the 'volume only' or canopy with a reference at midnight, together with the wind speed (m/s). During the day time the wind speed is about 5 m/s whereas it is about 2 m/s between 6 pm and 6 am.

Over these two days, decorrelation with strong oscillations is observed during the daytime whereas coherence it is high and stable between 6 p.m. and 8 a.m.

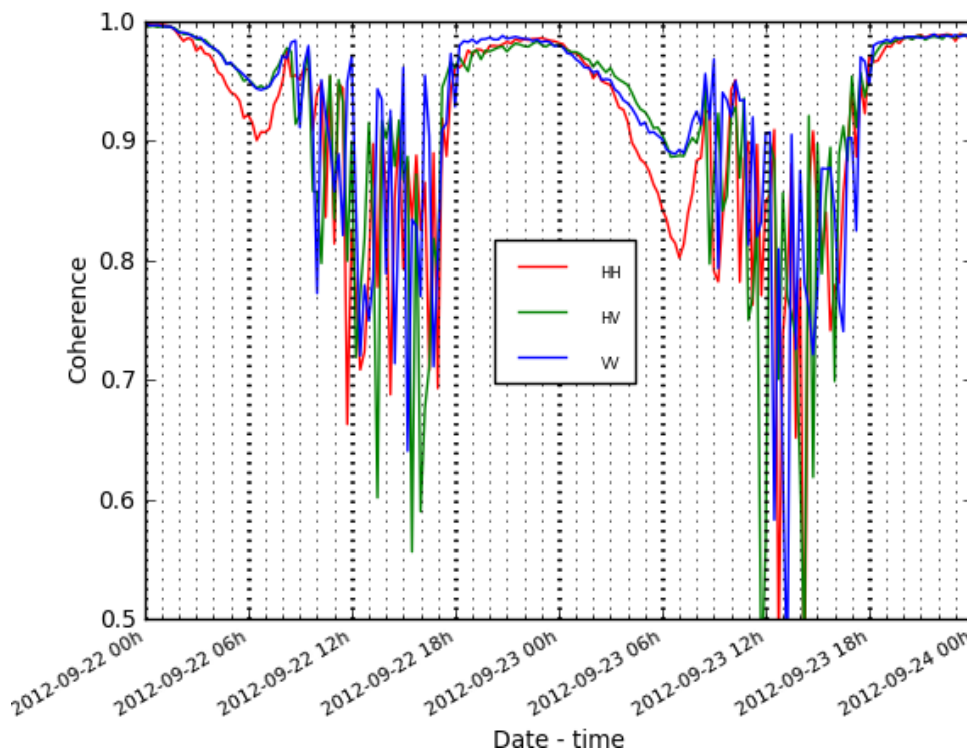


Figure 36: Daily cycle of the full forest in dry period computing with a reference at midnight

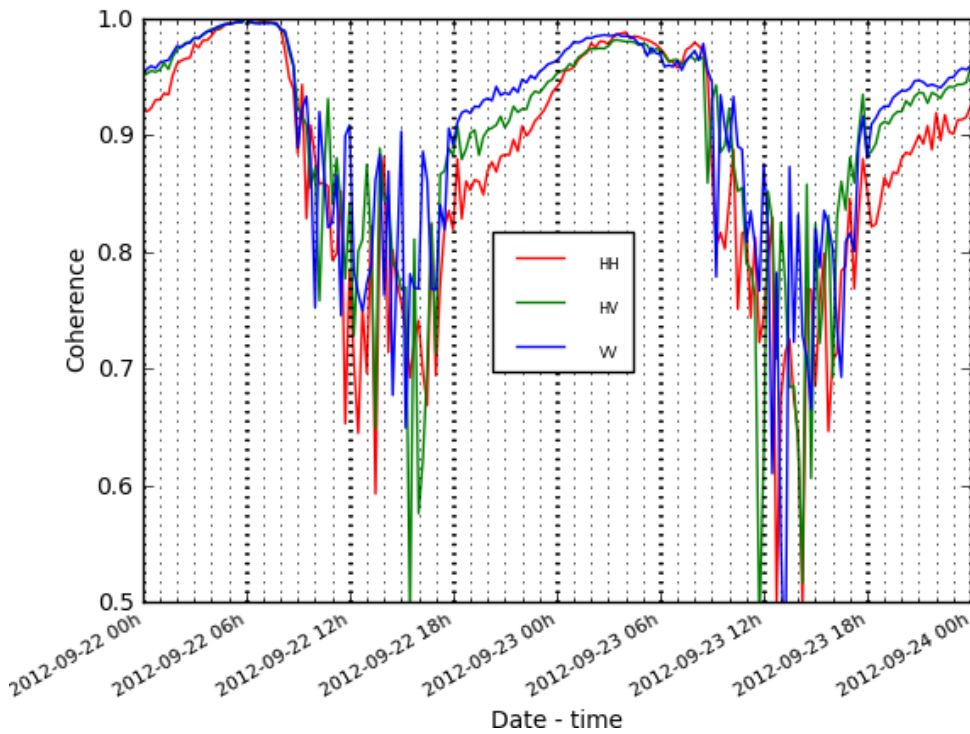


Figure 37: Daily cycle of the full forest in dry period computing with a reference 6 a.m

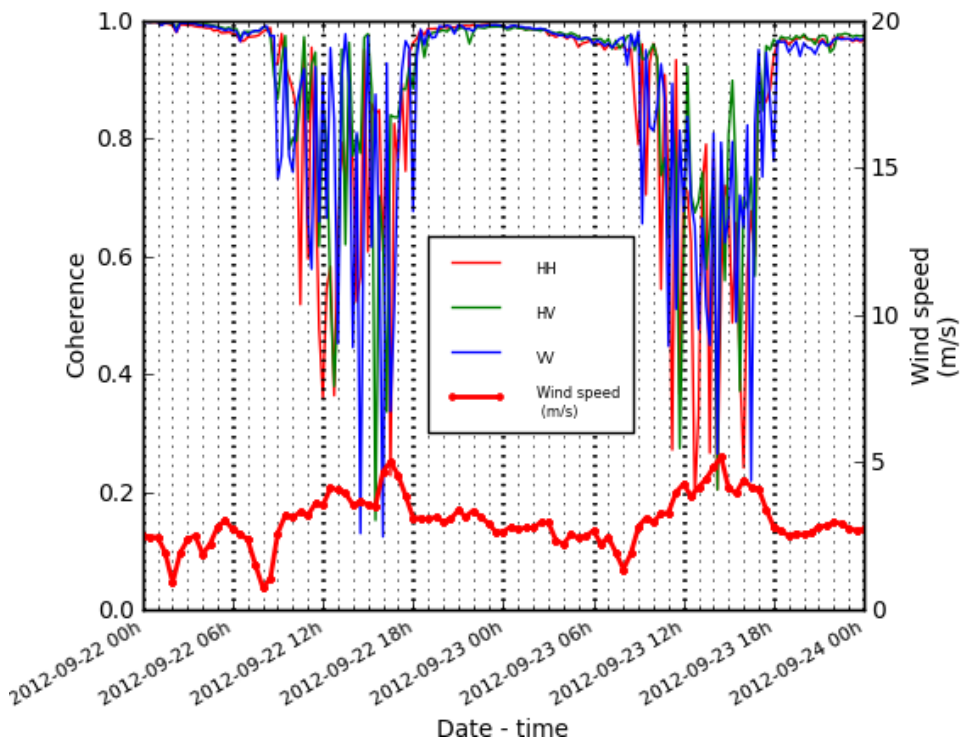


Figure 38: Daily cycle of the canopy (volume only) in dry period computing with a reference at midnight

Firstly, the results at night time are analysed as follows. In Figure 38, the coherence of 'Volume only' observed at night time is very high (greater than .97) and does not depend on polarization. Reversely, for the

'full forest' (Figure 36 and Figure 37), the coherence clearly depends on polarization. It is still very high at the reference time (midnight in Figure 36 and 6 am in Figure 37) and lower for other time of the day, but however, still higher than .9 for VV and HV, and higher than .8 for HH. Note that the shape of this coherence daily cycle in night time changes with the reference time. For the midnight reference time, Figure 37 shows a strong decorrelation in HH close to 6 a.m. for the 'full forest', and this is not observed for the 'volume only'. One possible interpretation is that the signal decorrelation for the 'full forest' is in relation with the ground contribution to the backscatter. This contribution, which may involve direct ground scattering or double bounce scattering, will be further investigated experimentally and also by using models. During the day time, the loss of coherencies is very likely caused by the wind effects. It is stronger for the volume case and the amplitude of the oscillations are also much stronger. For example the lowest coherencies were observed for the highest wind speed. It can be noted that the wind speed is higher during day time than during night time. In addition, the same variations are observed for all polarizations and reference times.

At this stage, these TropiScat results indicate that the motion of the forest due to the wind speed during the day will degrade any coherent processing. For this reason, in the following, we will limit for long time series analysis the measurements from dusk to dawn.

LONG TERM TIME SERIES OF COHERENCE

Figure 39 to Figure 41 show the temporal coherence of the polarimetric backscattering coefficients over a period of 3 months during to the rainy season (from 6th December 2011 to 11th Mars 2011). The reference signal S_2 corresponds to the signal on 18/12/2011 at 5 A.M. and the S_1 signal is the signal measured every 15 minutes (from 6th December 2011 to 11th Mars 2011). The rain fall data are depicted in the same figures. The signals acquired during rain events were removed from the data. We observe strong oscillations at short term and at long term, the coherence envelope decreases at longer terms but still remains high (e.g. from 0.9 to 0.7). We also note that after rain fall, the coherence decreases.

For the HH polarization (Figure 39), the coherence contour curve keeps a very high level (more than 0.8) until about 2 months and decreases to 0.7 after three months. The VV polarization (Figure 40), decreases quickly during the rain and continues to decrease slowly just after the rain. The VV coherence is lower than the HH coherence (decreases to 0.6 after three months). HV coherence (Figure 41) decreases faster than HH and VV (coherence decreases to 0.5 after three months). This can be explained by the fact that HV (volume effect) is more sensitive to leaves and branches growth/change and wind movement than HH and VV which incorporate more direct ground scattering and interactions volume/ground which are a priori more stable.

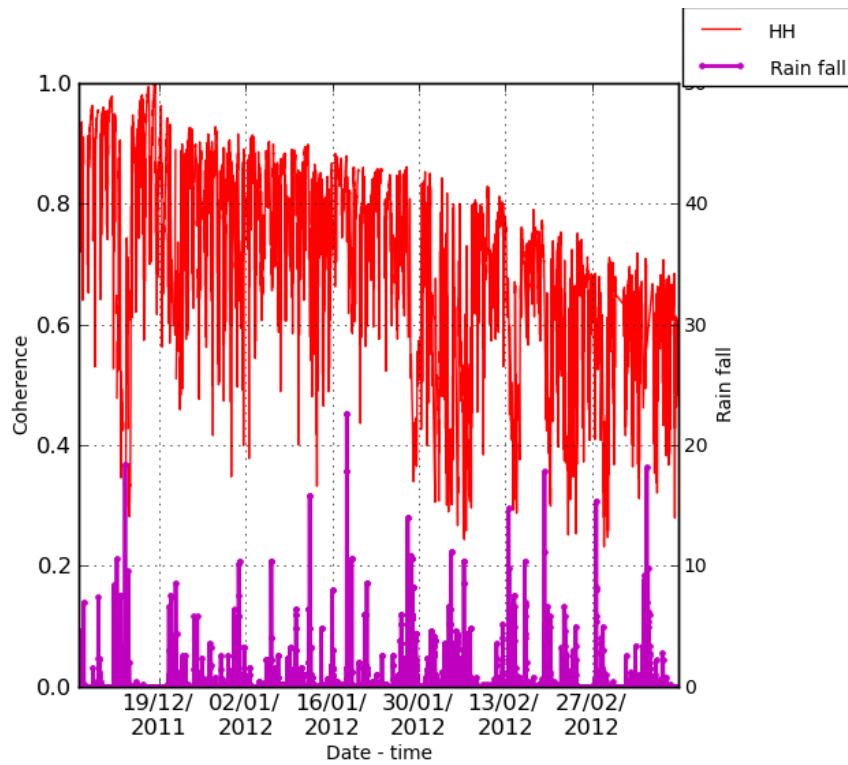


Figure 39 - Temporal coherence OF HH POLARIZATION over 3 months (full forest during the rainy season)

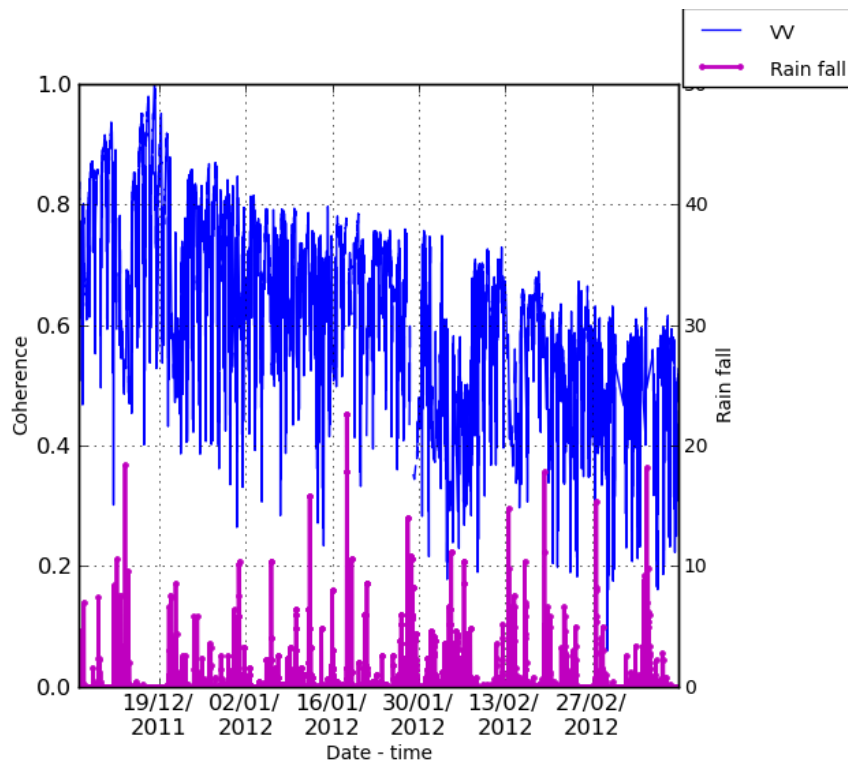


Figure 40 - Temporal coherence OF VV POLARIZATION over 3 months (full forest during the rainy season)

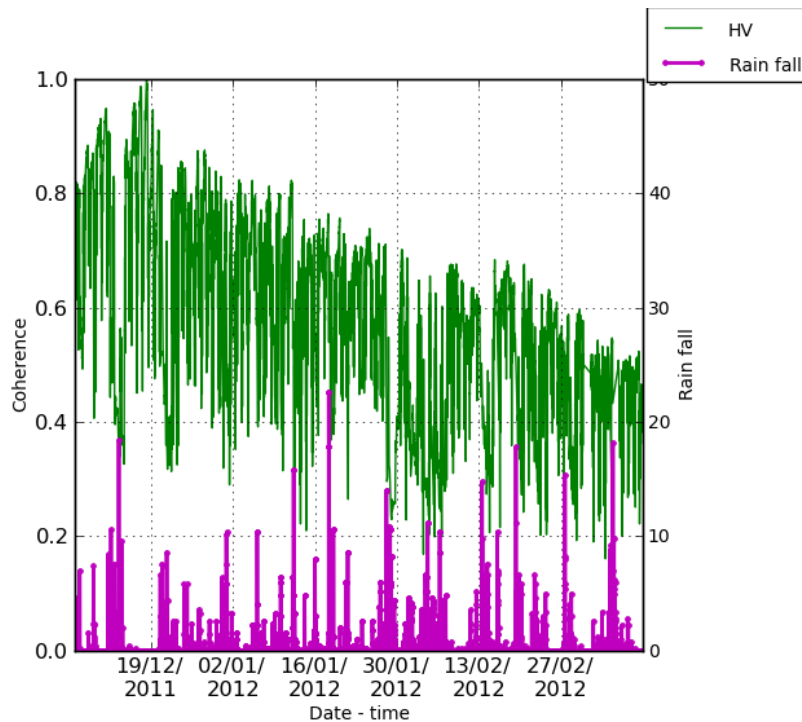


Figure 41 - Temporal coherence of HV polarization over 3 months (full forest during the rainy season)

Figure 42 shows the temporal coherence over a period of 5 dry days (from 16th December 2011 to 20th December 2011) during the rainy season. We observe a daily cycle, with high coherence in the night. The night/day decorrelation may be attributed to two phenomena. The first is the motion of the tree elements (mainly the branches) caused by the wind during the day. The second is related to a second effect is directly related to the tree ecophysiology. Previous studies (Mc Donald et al., 2002) have reported that P band dielectric properties of xylem tissue vary temporally, with marked diurnal cycle, corresponding to changes in xylem sap flux density, sap chemistry, and vapor pressure deficit (VPD), and these changes were also linked to meteorological conditions. In general, it was found that vapor pressure deficit was correlated to dielectric constant, however, decorrelation was apparent at low VPDs, e.g. after rain.

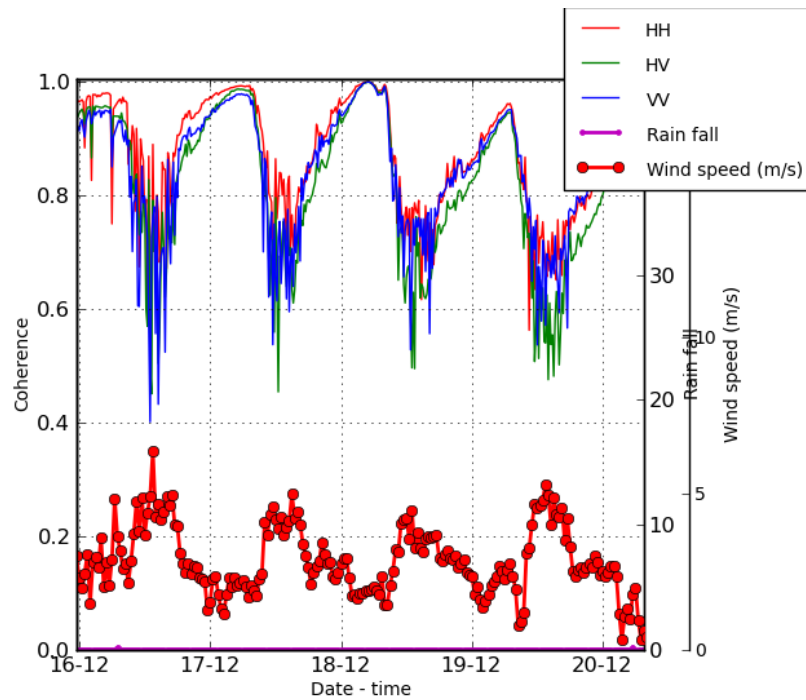


Figure 42 - Temporal coherence over 5 days during a dry period (full forest in the rainy season)

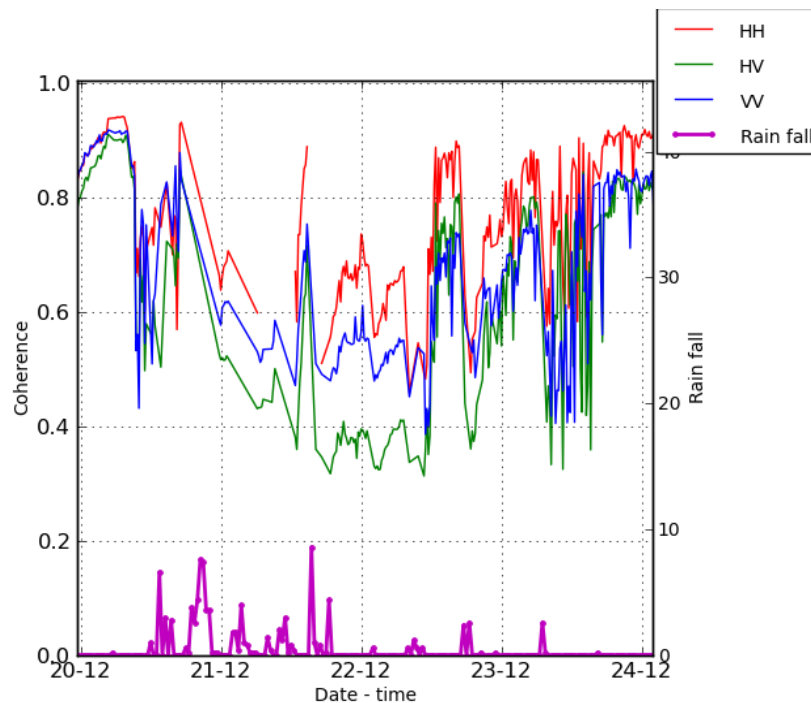


Figure 43 - Temporal coherence over 5 days during a rain period (full forest in the rainy season)

Figure 43 shows the coherence over a period of 5 rainy days. We observe that the rainfall disrupts the daily cycles: the maxima of coherence are around 0.8 and the coherence decreases up to 0.4.

During the dry season, Figure 44 and Figure 45 show that the HH and VV coherence (signal's envelope) is higher than 0.8 after one month and becomes close to 0.7 after 2 months. We note a fast decrease on the 09/10/2012 corresponding to the rain event.

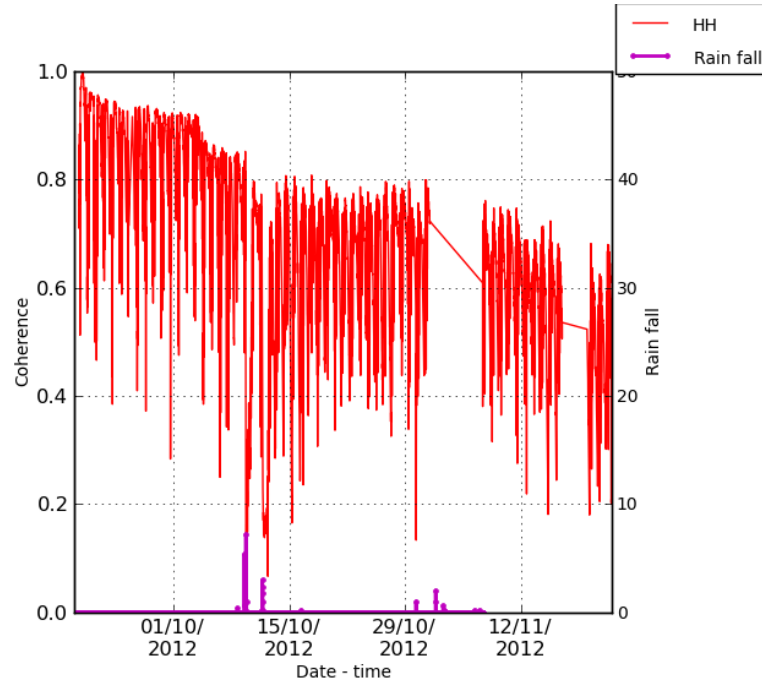


Figure 44 - Temporal coherence of HH over 3 months (full forest during the dry season)

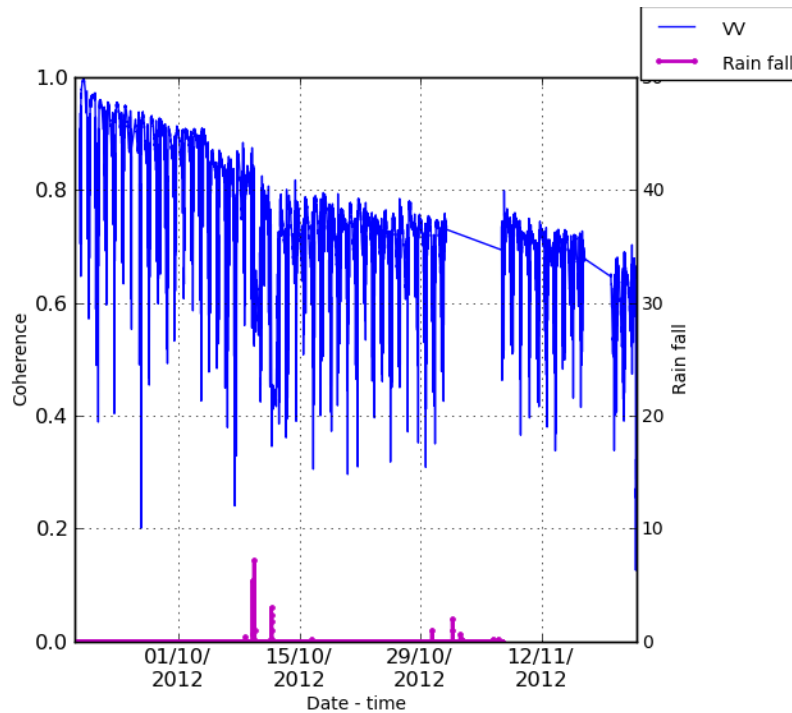


Figure 45 - Temporal coherence of VV over 3 months (full forest during the dry season)

The HV polarization (Figure 46) shows a coherence higher than 0.8 after one month and decrease abruptly after the rain events and becomes lower than 0.5 after 2 months.

Comparing the rainy and dry period, at short term, the coherence in the dry period is greater than during the rainy period but is lower at long-term. A possible explanation is the fact that, during the dry period, the rain effect decorrelated the relations between vapor pressure deficit (low during dry season) and dielectric constant, resulting in a lower coherence after rain [Mc Donald et al., 2002].

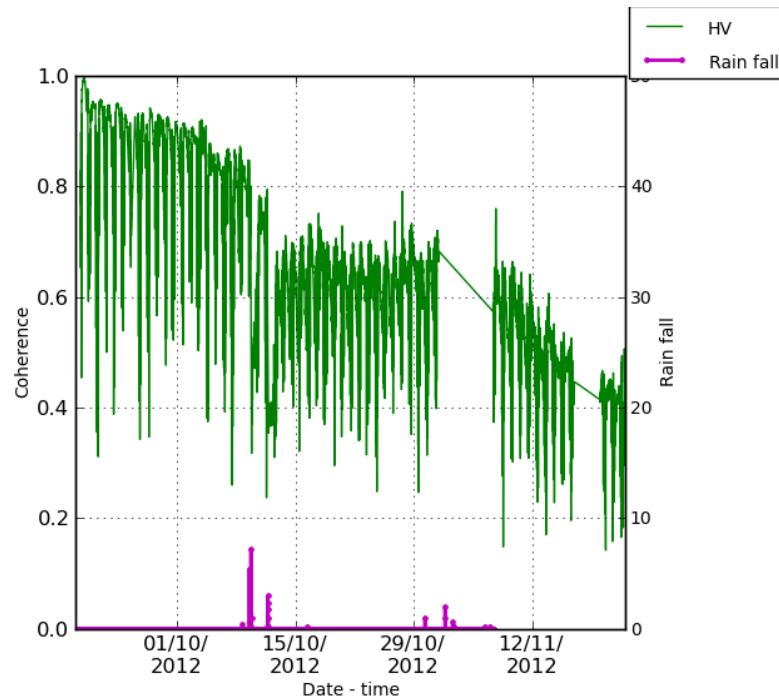


Figure 46 - Temporal coherence of HV over 3 months (full forest during the dry season)

AVERAGE TEMPORAL DECORRELATION

The main objective of this study is to quantify the temporal decorrelation in the case of repeat pass acquisitions from space. Therefore a given hour of the day will be considered for long time series. In the rainy period full polarimetric data are available from 6th December 2011 to 14th Mars 2012 and in the dry period from 19th September 2012 to 18th December 2012.

In this section, the goal is to evaluate the statistics of coherence as a function of temporal baseline (t_2-t_1) over a given period (N_c days). So, for a given temporal baseline, the set of all possible couples (t_1, t_2) is considered. Within this set, a subset of N_r couples is determined so that the choice of couples (t_1, t_2) is uniformly randomly distributed over the period and N_r is the same for all baselines. Note that the system introduces itself a temporal decorrelation that was compensated [Zebker et al., 1992]. The system coherence was computed with the complex direct coupling for all antennas pairs (between the reception and the emission antenna) [3.4.2]. The overall coherence was then divided by the system coherence to estimate the forest decorrelation.

Figure 47 presents the mean coherence computed over the volume only for a temporal baseline ranging between 1 and up to 30 days with $N_r=60$ and 30 days with $N_r=30$, among $N_c=90$ days in the rainy period, considering all acquisitions between 5 a.m and 7 a.m. On the first 30 days, the result is the same on both cases for the HH, HV and VV polarizations. We can deduce from this plot that in this case the number N_r of couples used for averaging the coherence is sufficient. It can be observed that for the volume only, the coherence remains high (>0.8) up to 20 days for HV polarization (lightly lower for HH and VV) and it drops to the interval $[0.65, 0.7]$ after 60 days.

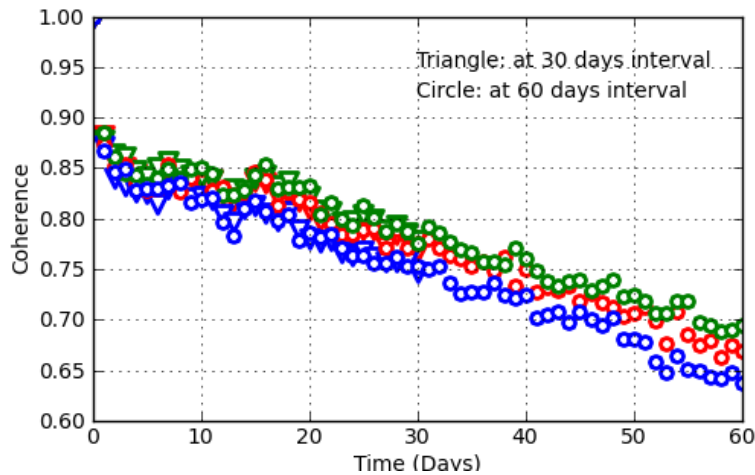


Figure 47: Mean coherence at 6 am versus temporal baseline of the canopy (volume only) for HH, HV and VV polarizations in the rainy period averaged from measurements at time interval of 30 and 60 days. The triangle corresponds to the coherence computed up to 30 days interval and the circle up to 60 one. Red curve corresponding to HH polarization, green to HV and blue to VV.

Figure 48 shows the mean coherence for the full forest in the rainy and dry periods and for temporal baselines ranging up to 60 days, computed as previously.

In the dry period, up to 20 days, the mean coherence is higher than 0.8 for all polarizations. This is the most important result since it shows that over such a temporal baseline coherence is sufficient to envisage coherent processing based on repeat pass acquisitions.

In the rainy period the coherence drops quickly to 0.7 in the very first temporal baseline (3 days) and decreases very slowly after that. It can be observed that up to 20 days the coherence in the dry period is higher than in the rainy period for all polarizations. At long term (30-40 days) the mean coherence in HH and VV polarizations becomes lower in the dry period than in the rainy period and HV polarization in the rainy period is always lower than in the dry period, but reaching the same value (0.6) for 60 days baseline.

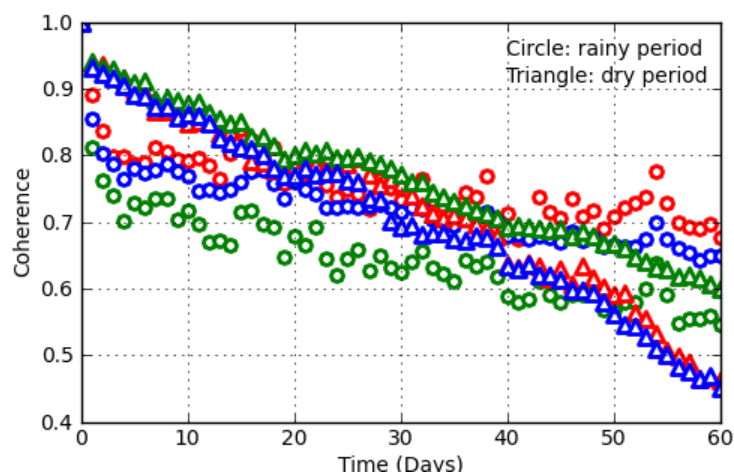


Figure 48: Mean coherence at 6 am versus temporal baseline of the full forest for the HH, HV and VV polarizations in the rainy and dry period at temporal baseline 60 days. The triangle is corresponding to the coherence in dry period and the circle in the rainy one. Red curve corresponding to the HH polarization, green to HV and blue to VV.

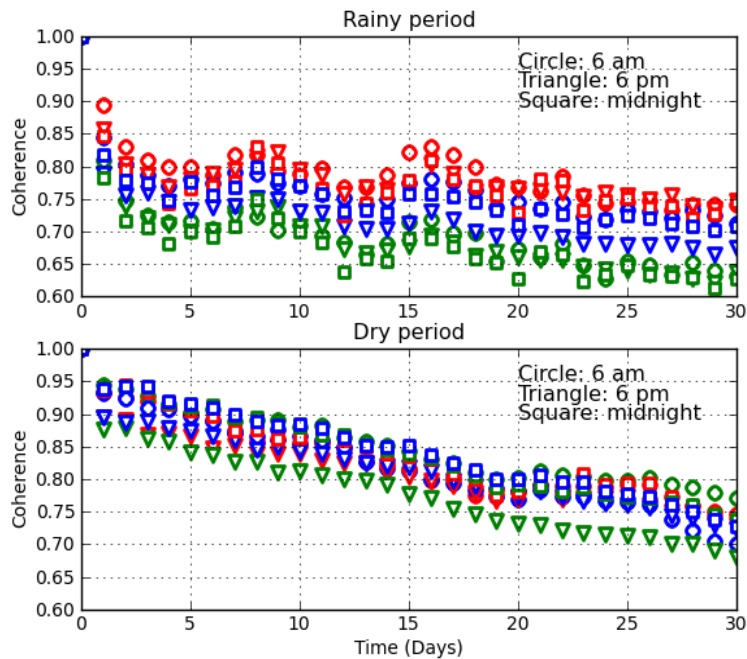


Figure 49: Mean coherence versus temporal baseline of the full forest for the HH, HV and VV polarizations. Top: in the rainy period. Bottom: in the dry period. Circle: time observation at 6 am, triangle: time observation at 6 pm and square: time observation at midnight. Red curve corresponding to the HH polarization, green to the HV and blue to the VV one.

Comparison between coherences at specific time of the day is performed in the following. Figure 49 reports the mean coherence computed at 6 am, 6 pm and at midnight in the rainy period (top) and in the dry period (bottom). In the rainy period, HH and HV show close values as a function of time of the day, whereas VV have lower values at 6 pm. HH has coherences higher than VV which are higher than HV. HH polarization is the most coherent at 6 a.m., whereas for VV coherence is weaker at 6 p.m. Globally, in the rainy period, the coherence is more sensitive to polarization than to time, between dusk and dawn.

In the dry period, all polarizations are approximately of the same order, except the case of the HV polarization at 6 pm for which the coherence is smaller. This decorrelation may be due to the wind effect at 6 pm which may still be causing motion in the canopy at this time in the dry season as shown in Figure 38.

To confirm this hypothesis, a comparison of the coherences is made in the dry period at 6 pm and 7 pm in Figure 49. These figure shows that the coherence is higher at 7 p.m. especially for the HV polarization, and actually the wind speed at 7 pm is smaller than at 6 pm (see Figure 38).

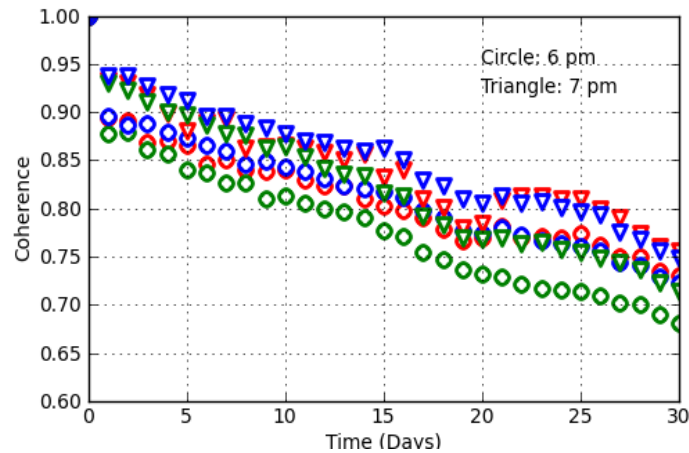


Figure 50: Mean coherence versus temporal baseline of the full forest for the HH, HV and VV polarizations in the dry period at time interval 30 days at 6 pm and 7 pm

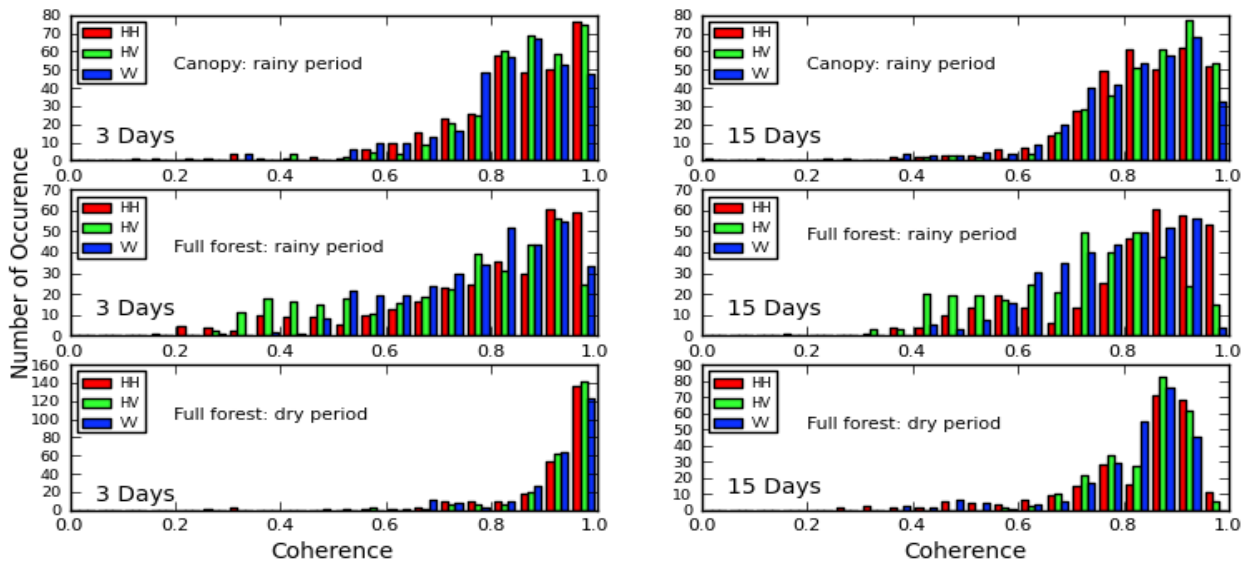


Figure 51: Histogram of the coherence for temporal baselines 3 days (left) and 15 days (right). Top panel: results for the canopy in the rainy period, middle: full forest in the rainy period and bottom: full forest in the dry period

Figure 51 reports the histograms related to Figure 49 for respectively 3 days and 15 days temporal baselines at 6 a.m. It corresponds to the set of coherences for the volume only in the rainy period, for the full forest in the rainy period and the full forest in the dry period, for the $N_r=60$ pairs and the 9 considered times around 6 a.m. It can be observed that, in the rainy period, for 3 and 15 days baseline, major part of occurrences are localized in the interval $[0.8-1]$ for the volume only whereas the histogram is more spread in the interval $[0.4-1]$ for the full forest. This fact evidences the role of the underlying ground in the decorrelation process in the rainy period. However, it can be noted that high coherences values (close to 1) may correspond to no-rain days during the rainy period. Another observation is that there is a strong similarity between histograms corresponding to 3 and 15 days baselines in this period, showing that for these scales of time, the coherences are only weakly dependent on the time interval. Comparing the coherences of the full forest in the rainy and dry period, one can see, in the dry period, a high concentration of the histogram in $[0.9-1]$ for 3 days temporal baseline and in $[0.8-0.9]$ for 15 days temporal baseline: in this case, coherence is more dependent on the temporal baseline.

COHERENCE VERSUS INCIDENCE ANGLE

The above results were performed with incidence angle centered on 44°. In this section the influence of the incidence angle is investigated. The coherence was computed up to 30 days temporal baseline for incidence angles ranging from 40° to 61°. For a given incidence angle the mean coherence as computed in previous section was averaged again for all baselines ranging from 15 to 25 days.

Figure 52 shows the average coherence versus baseline as a function of incidence angle. A relative stability for incidence angle ranging from 40° to 50° and a more important decorrelation at higher incidence angles, in particular for HH and VV. Although care should be taken to interpret the results (e.g. in terms of homogeneity of forest canopy at different angles) it can be understood that the decorrelation is caused by the relative volume contribution which increases with incidence angle.

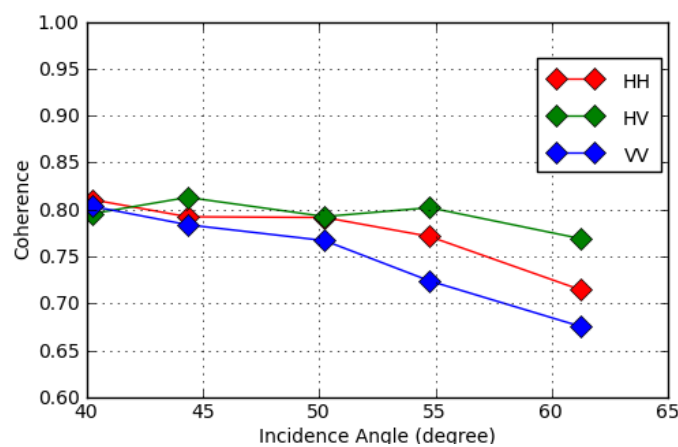


Figure 52: Variation of the coherence as a function of the incidence angle

5.1.3. BACKSCATTERING COEFFICIENT RESULTS

BACKSCATTERING COEFFICIENT DERIVATION

As mentioned above, for each acquisition we obtain a normalized range backscattering profile and for the range $i.dr$, the range profile is defined by the complex array $S(i)_t = (X(i)_t, Y(i)_t)$. The backscattering coefficient I_{pq} is computed by averaging the backscattering coefficient range profile in distance, time and several couples successively. First, we define a range gate for filtering the data. At a given time t (iteration time, every 15 mn), we perform an averaging over resolution cells (Equation 10)

$$I_{pq}(t, c) = \frac{\sum_{r=r_{\min}}^{r_{\max}} (X(r)^2 + Y(r)^2)}{N_r}$$

Equation 10

Where c defines a couple of antennas, t is the time of acquisition and r a given range cell. N_r is the number of cells between r_{\min} and r_{\max} .

Then an averaging temporal window Δt is defined and the backscattering coefficient is computed with the following averaging, with N_T the number of acquisitions (Equation 11):

$$I_{pq}(t, c) = \frac{\sum_{t'=t-\Delta t/2}^{t+\Delta t/2} I_{pq}(t', c)}{N_T}$$

Equation 11

with $p = \begin{vmatrix} H \\ V \end{vmatrix}$ and $q = \begin{vmatrix} H \\ V \end{vmatrix}$

Finally, for increasing the degree of liberty and increasing the number of computational cells we performed an averaging over several couples (Equation 12). In fact, the behaviour of the backscattering coefficient changes according to the considered couple: each couple sees a different scene. So using several antennas increases the number of independent looks.

$$I_{pq}(t) = \frac{\sum_{c=1}^{N_c} I_{pq}(t, c)}{N_c}$$

Equation 12

Where N_c is the number of couples.

TIME SERIES

Using the definition of the backscattering coefficient given in the previous chapters, we can focus on the time series of these coefficients on large periods.

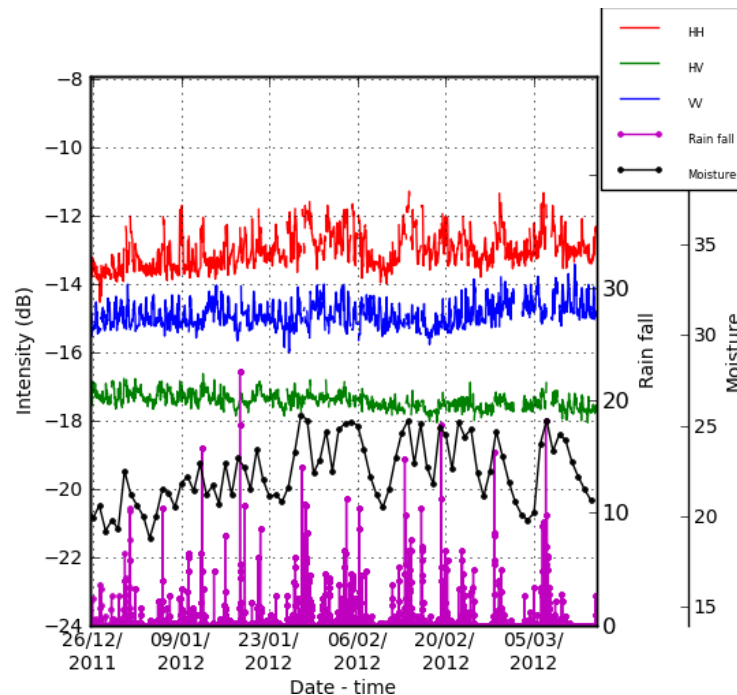


Figure 53 - The geophysical parameters (rain fall and soil moisture) and the HH, VV, HV backscattering coefficient computed over the canopy (volume only) during the rainy period

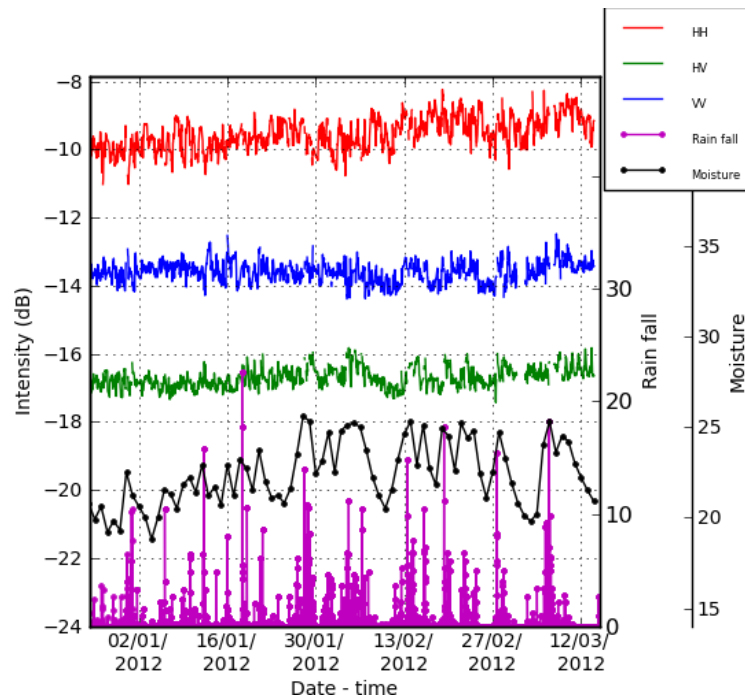


Figure 54 - The geophysical parameters (rain fall and soil moisture) and the HH, VV, HV backscattering coefficient computed over the full forest during the rainy period

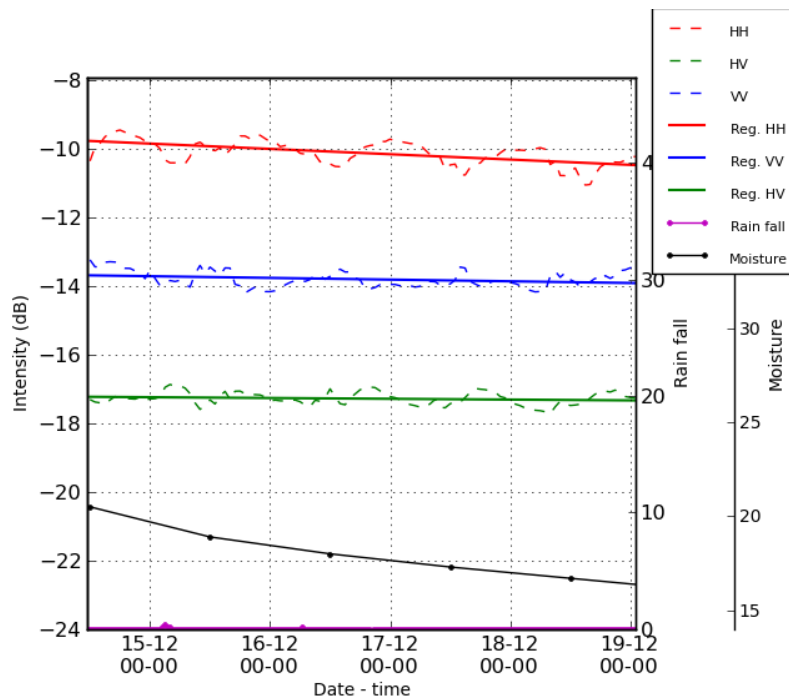


Figure 55 – Detailed of the temporal variations during 5 dry days in the rainy period of the geophysical parameters (rain fall and soil moisture) and the radiometric signal computed over the full forest.

Figure 53 and Figure 54 show the backscattering coefficient (HH, HV and VV) over three months in the rainy period (from 26/12/2011 to 11/03/2012). These figures also show the rain fall and the soil moisture at 10 cm depth. In the case of the canopy, we note a relatively stable level of the backscattering coefficient for all polarizations. For the full forest, we note a stable level for the VV polarization whereas HH and HV increase slowly through this rainy period. At the same time, soil moisture increases over time as shown in Figure 54

(black curve). As the HH is supposed to include the ground interaction, it was expected that it increases with the soil moisture. The increase of HV in full forest (less in 'volume only') could be caused by double bounce. Making a zoom on the few (5) dry days in the rainy period, Figure 55 shows a decrease of the signal on all the polarization linked to the decrease of the soil moisture. The VV backscattering coefficient appears the most stable with time.

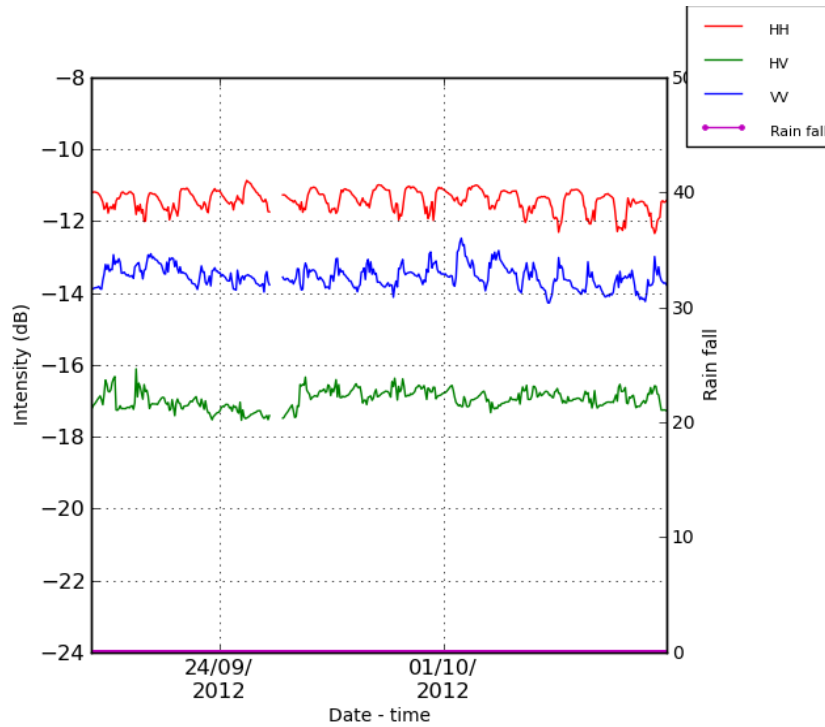


Figure 56 - The geophysical parameters (rain fall and moisture) and the radiometric signal computed over the canopy during the dry period

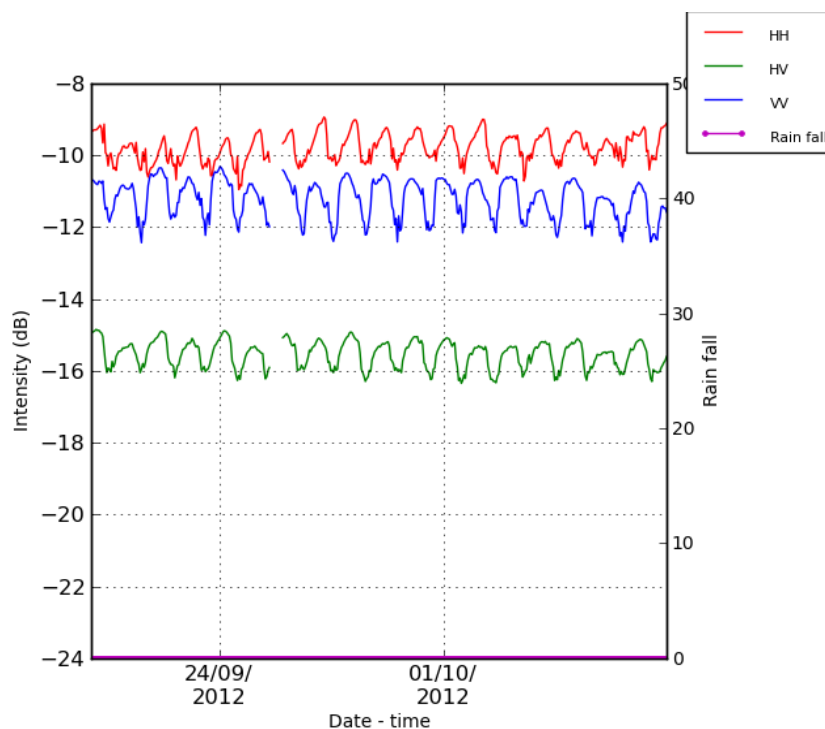


Figure 57 - The geophysical parameters (rain fall and moisture) and the radiometric signal computed over the full forest during the dry period

Figure 56 and Figure 57 show the backscattering coefficient computed in the dry period (from 20/09/2012 to 07/10/2012) for 'volume only' and for full forest respectively. In these figures, a daily cycle of 1 dB variation between the day and the night can be observed, the daily cycle being clearer for full forest than for the 'volume only'. It was previously discussed that the cycle comes from dielectric constant of xylem tissue. For 'full forest', larger permittivity changes are possibly caused by changes in the lower woody elements. In Compared to the rainy period, the backscattering coefficient at HH, VV, HV appear more stable.

BACKSCATTERING COEFFICIENT AT DAWN AND DUSK

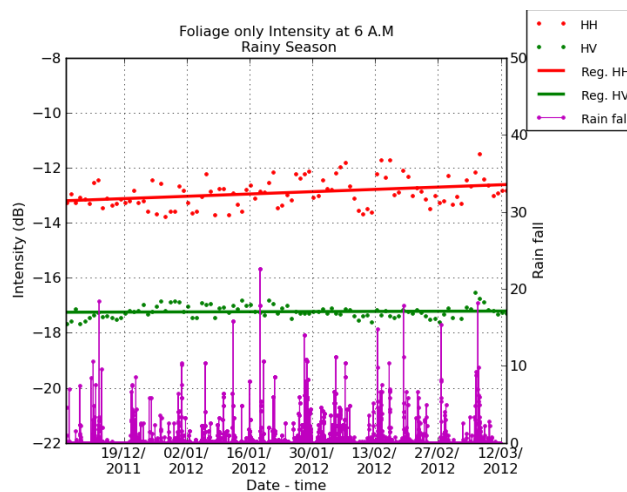


Figure 58: HH and HV backscattering coefficient computed over the canopy at 6 a.m and corresponding rain fall data

Figure 58 reports the backscattering coefficient computed at 6 a.m. over the volume only zone of the forest with the rain fall rate every half hour. There are short term variations of both HH and HV backscattering coefficients with time, related to rain fall. At long term, HH grows of less than 1 dB, whereas HV is stable.

Figure 59 and Figure 60 report the backscattering coefficient computed at 6 a.m. and 6 p.m. respectively. For both, a small increase is observed along this rainy period for both the HH and HV polarization, whereas the VV one is more stable. In Figure 62 and Figure 63 the same is displayed during the dry season, showing a coherent behavior versus the previous ones. In particular, the values of January 2012 are retrieved in January 2013.

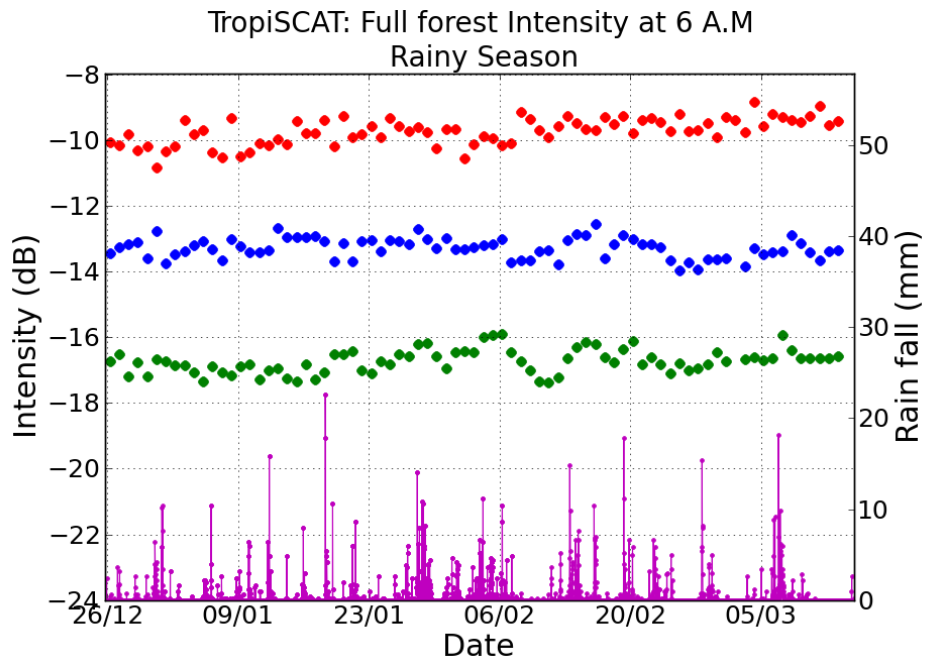


Figure 59: HH,VV and HV backscattering coefficient computed over the full forest at 6 A.M and corresponding rain fall

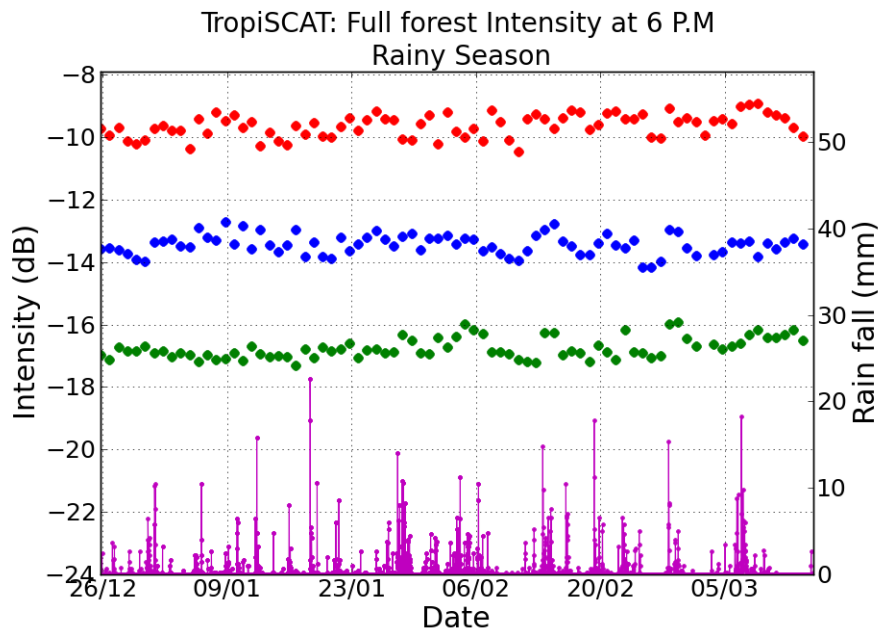


Figure 60: HH,VV and HV backscattering coefficient computed over the full forest at 6 P.M and corresponding rain fall data

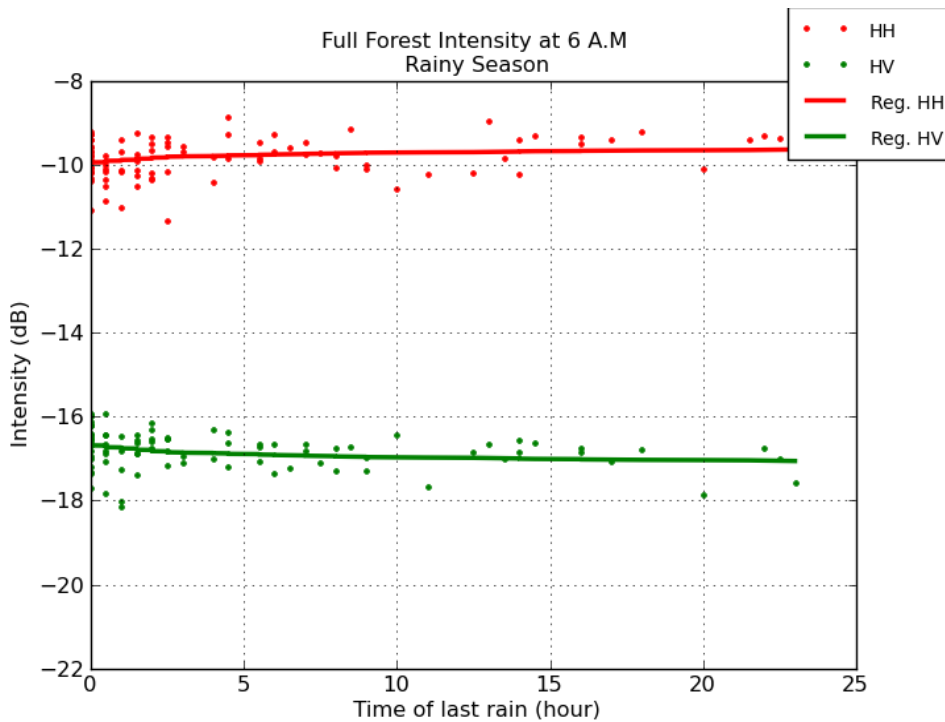


Figure 61: Backscattering coefficient variation at 6 a.m time lag of most recent rain fall

The influence of the most recent rain event on the backscatter backscattering coefficient is studied by computing the backscattering coefficient as a function of time after the last rain event. Figure 61 shows that the results are relatively stable with this time lag, which suggests that the effect of rain is mainly through the increase of moisture during the first few hours.

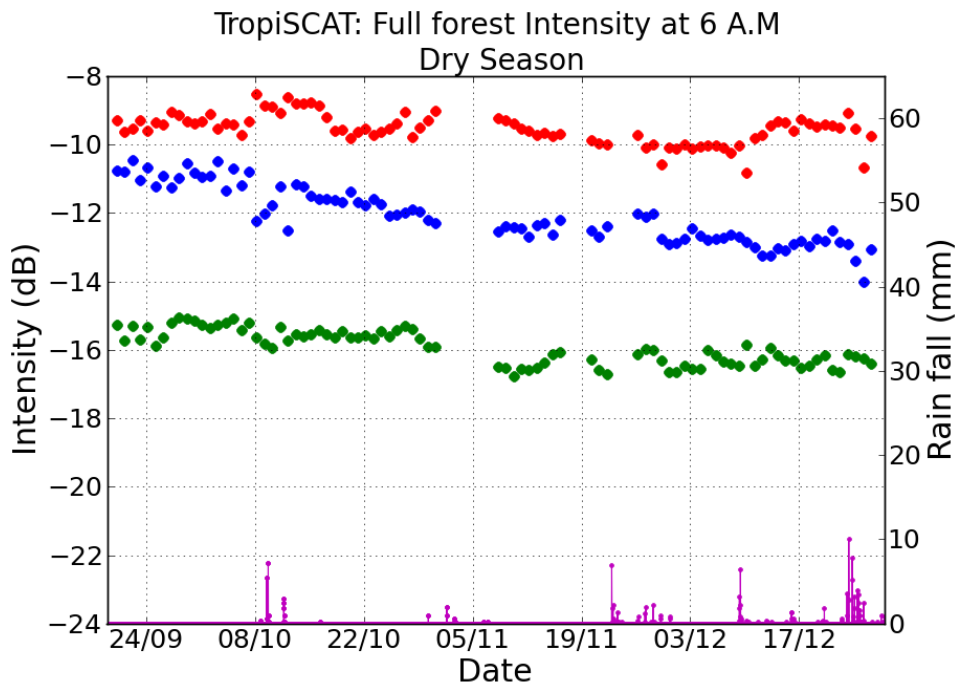


Figure 62: HH,VV and HV backscattering coefficient computed over the full forest at 6 a.m. and corresponding rain fall; dry season

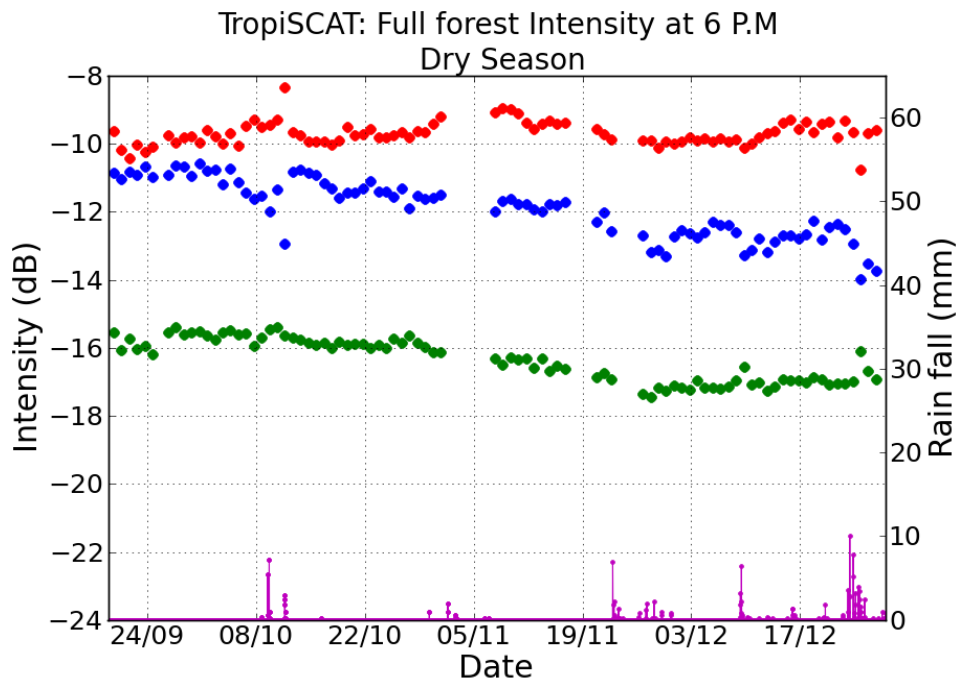


Figure 63: HH,VV and HV backscattering coefficient computed over the full forest at 6 p.m. and corresponding rain fall; dry season

5.1.4. CONCLUSION

The TropiScat campaign was installed at the Paracou field station in French Guiana since October 2011. The main goal of this campaign is to study the temporal coherence for the tropical forest at P Band. Three months of data in the rainy and dry period were analyzed with range impulse responses issued from various antennas pairs. Coherence exhibits a daily cycle showing a high decorrelation where the wind speed is greater than 2.5 m/s, which occur in both seasons systematically during day time. These cycles are perturbed by the rain. Therefore the analysis was limited to time from dusk to dawn (6 pm to 6 am). The long times series analysis showed that during the rainy season the observed decorrelation is weakly dependent on temporal baseline up to 20 days. On the contrary, during the dry season, there is a regular trend in the decrease of coherence with temporal baseline. The coherence in the dry season is much higher than in the rainy season at short term, is in the same order at long term and even becomes lower for very large baselines. It was also shown that decorrelation is somehow influenced by the time of acquisition during night time (between 6 pm and 6 am).

The backscattering coefficient exhibits also this daily cycle but presents a high stability/ and or a slow increase over the rainy period. In the dry period, the signal is more stable than in the rainy period and we observe a small decrease for the HV and VV polarization.

This set of results suggests the feasibility of coherent repeat pass processing like PolInSAR and Tomography over tropical forest at P-band during the dry season. During the rainy season further investigations appear to be necessary to assess such feasibility. Finally, the database provided by the TropiScat campaign constitutes an important contribution to study the retrieval algorithms for the BIOMASS mission over tropical forests.

5.1.5. REFERENCES

[Albinet et al., 2011a] Albinet, C.; Borderies, P.; Koleček, T.; Rocca, F.; Tebaldini, S.; Le Toan, T. et Villard, L.; "Temporal Backscattering of Forests: Ground Measurements", PIERS 2011, Suzhou, China.

[Albinet et al., 2011b] Albinet, C.; Borderies, P.; Koleček, T.; Rocca, F.; Tebaldini, S.; Le Toan, T.; Villard, L.; Mermoz, S. et Ho Tong Minh, D.; "TROPISCAT : A Multi-Frequency PolInSAR Data Campaign Of Acquisition For Vegetation Characterization", IGARSS 2011, Vancouver, Canada.

[Albinet et al., 2012a] C. Albinet, P. Borderies, T. Koleček, F. Rocca, S. Tebaldini, L. Villard, T. Le Toan, A. Hamadi, D. Ho Tong Minh, "TropiScat: A ground Based Polarimetric experiment in Tropical forests", IEEE Journal of Selected Topics in Applied Earth Observations and Remote Sensing, , vol. 5, no. 3, pp. 1060 – 1066, 2012.

[Albinet et al., 2012b] Albinet, C.; Borderies, P.; Koleček, T.; Rocca, F.; Tebaldini, S.; Le Toan, T. et Villard, L.; "Temporal Backscattering of Tropical Forest at P Band with Ground Experiment", PIERS 2012, Kuala Lumpur, Malaysia.

[Hamadi et al., 2013a] Hamadi, A.; Borderies, P.; Albinet, C.; Koleček, T.; Villard, Ho Tong Minh, D. and Le Toan, T.; "Temporal survey of polarimetric P-Band scattering of tropical forests", GRST, 2013. (Accepted)

[Hamadi et al., 2013b] Hamadi, A.; Borderies, P.; Albinet, C.; Koleček, T.; Villard, L.; Le Toan, T.; Ho Tong Minh, D. and Burban, B.; "Temporal Coherence of Tropical Forests at P-Band: Dry and Rainy Seasons", GRSL, 2013. (Submitted)

[Ho Tong Minh et al., 2012a] D. Ho Tong Minh, S. Tebaldini, F. Rocca, "Design of the ground based array for tomographic imaging in the TropiScat experiment", Synthetic Aperture Radar, 2012. EUSAR. 9th European Conference on, pp. 661-664, Apr. 2012.

[Ho Tong Minh et al., 2012b] D. Ho Tong Minh, S. Tebaldini, F. Rocca, T. Le Toan, P. Borderies, T. Koleček, C. Albinet, L. Villard and A. Hamadi. "Temporal Decorrelation in a Tropical Forest: Results from TropiScat and Implications for Repeat Pass Tomography". Geoscience and Remote Sensing Symposium (IGARSS), 2012.

[Ho Tong Minh et al., 2012c] D. Ho Tong Minh, S. Tebaldini, F. Rocca, C. Albinet, P. Borderies, T. Koleček, T. Le Toan, L. Villard, "TropiScat: Multi-temporal MultiPolarimetric Tomographic Imaging of Tropical Forests" Geoscience and Remote Sensing Symposium (IGARSS), 2012 IEEE International proceedings, pp. 1536-1539, 23-27 July 2012.

[Ho Tong Minh et al., 2012d] D. Ho Tong Minh, T. Le Toan, F. Rocca, M. Réjou-Méchain, J. Chave, Ho Tong Phuong Que, S. Tebaldini, T. Koleček, P. Borderies, C. Albinet, L. Villard, A. Hamadi, "Day-Night Tropical Forest Phenomenology through Tomographic Imaging: Paracou results", SELPER 2012.

[Ho Tong Minh et al., 2013] D. Ho Tong Minh, S. Tebaldini, F. Rocca, T. Koleček, P. Borderies, C. Albinet, L. Villard, A. Hamadi, and T. Le Toan, "Ground based array for tomographic imaging of the tropical forest in P-band," Geoscience and Remote Sensing, IEEE Transactions on, Vol. 51, No. 8, DOI.10.1109/TGRS.2013.2246795.

[Koleček et al., 2012] T. Koleček, P. Borderies, F. Rocca, C. Albinet, D. Ho Tong Minh, S. Tebaldini, A. Hamadi, L. Villard, T. Le Toan, "TropiScat: A polarimetric and tomographic scatterometer experiment in

French Guiana forests”, IEEE on Geoscience and Remote Sensing Symposium (IGARSS), 22-27 Jul. 2012, pp. 7597-7600.

[McDonald et al., 2002] McDonald E P, Erickson J E, Kruger E L.; “Can decreased transpiration limit plant nitrogen acquisition in elevated CO₂ ?”, Functional Plant Biology, 29(9): 1115–1120, 2002.

[Touzi et al., 1999] R. Touzi, A. Lopes, J. Bruniquel, P.W. Vachon “Coherence estimation for SAR Imagery”, IEEE Transactions on Geoscience and Remote Sensing, vol. 37, no. 1, pp. 135-149, 1999.

[Wagner, 2012] F. Wagner, “Confronting Satellite and Field Measurements Data to improve the understanding of Carbon Uptake by Tree In French Guiana”, SELPER proceedings, 19-23 Nov. 2012.

[Zebker et al., 1992] Zebker, H.A.; Villasenor " Decorrelation in interferometric radar echoes", IEEE Transactions on Geoscience and Remote Sensing, vol. 30, no. 5, pp. 950-959, Sep. 1992.

5.2.WP 32: TOMOGRAPHIC DATA PROCESSING

The aim of this section is to present the analysis results related to both of short term and long term temporal decorrelation in the frame of the TropiScat experiment.

5.2.1. TOMOGRAPHIC IMAGING

P-band tomograms for all polarimetric channels are shown in Figure 64. It should be noted that the terrain slopes down moving away from the tower, which is why targets appear at negative height values. The white line denotes an average topography from in-situ measurements. Up to about 50-70 m away from the tower the tomographic imaging shows scattering from the ground and from about 30 m above, which clearly reveals the structure of the vegetation in that area. It is interesting to note a substantial gap between the top and the bottom of the scattering layers, which suggest the most dense canopy layer is on top. Farther away from the VNA about 200m, the imaging is not as certain, due to both the increased distance (decreasing SNR) and the vertical resolution loss.

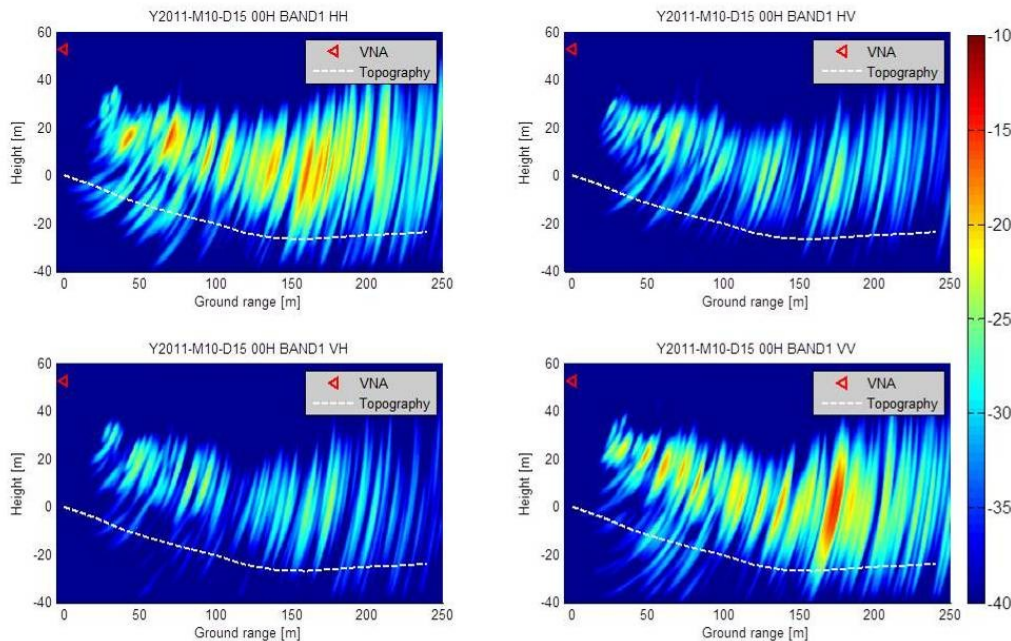


Figure 64: . Multi polarimetric tomogram (Y2011-M10-D15-00H00). The white line indicates terrain topography.

Accordingly, the near range area (i.e. up to 120 m away from the array) is certainly the most interesting for present and future analysis. In this area, vertical resolution is on the order of 6-12 m, which allows us to separate different vertical layers within the forest volume. On the contrary, physical interpretation becomes uncertain at far ranges, as vertical resolution increases with range. Furthermore, in the near range area the incidence angle varies from 20° - 60° , allowing combining and investigating the temporal backscatter of Airborne or Spaceborne P-band SAR data.

5.2.2. MULTI FREQUENCY TOMOGRAM

Data analysis mainly focuses on P band, which was defined as top priority. However, vertical imaging was also performed at higher frequency bands.. Figure 65 reports multi frequency tomograms at VV and also shows the exploitation of full bandwidth from 400 MHz to 1000 MHz. The best imaging quality is expected at 500 MHz. As expected, at higher frequencies volume contributions are dominant even at near range, due to reduced wave penetration. The best vertical resolution is achieved at 900 MHz due to the shortest wavelength. The ultra-bandwidth tomogram, see the right bottom panel, is observed to produce the highest range resolution thanks to 600 MHz bandwidth, witnessing that different bands are properly combined.

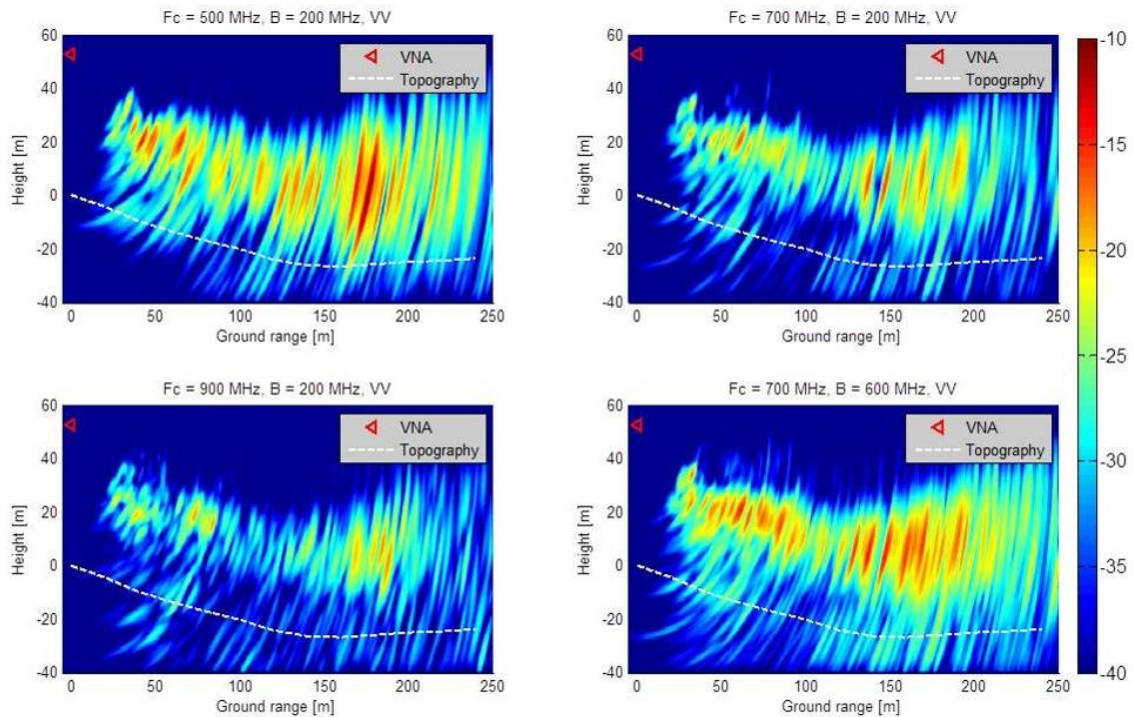


Figure 65: Multi frequency tomogram (Y2011-M12-D15-00H00).

5.2.3. MULTI TEMPORAL TOMOGRAM

Figure 66 reports a few snapshots from the “tomographic movie” obtained over time at P-band. In this case each panel has been generated in slant range - height coordinates, and flattened so as to bring terrain level at 0 m, in order to help visualization and interpretation of the results. As visible, acquisitions collected during day time are often characterized by a lower backscattering coefficient with respect to night hours. This phenomenon has been observed to be associated with wind speed, which reaches its peak during day hours and also with rain events as shown in Figure 67. Accordingly, the observed backscattering coefficient drop can be interpreted as being the result of defocusing phenomena arising from the fact that the 15 antenna pairs are operated at different times, hindering the coherent integration. As shown in section tower stability, the impact of eventual tower motions is not enough to justify this phenomenon, after which we conclude that it is due to the motion of the forest under the action of wind.

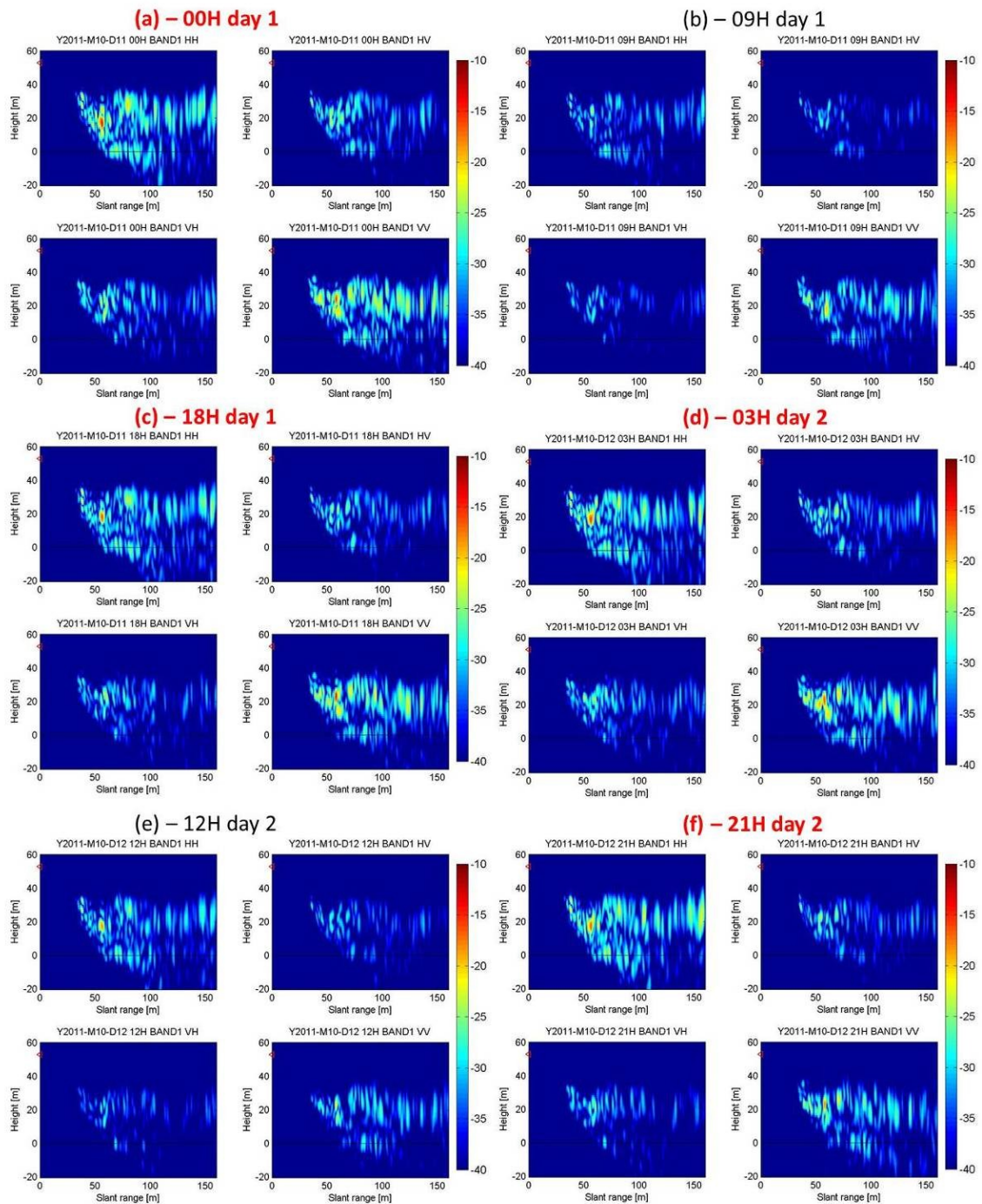


Figure 66: Polarimetric tomographic imaging as a function of acquisition time at P-band (500 MHz). Units are in dB.

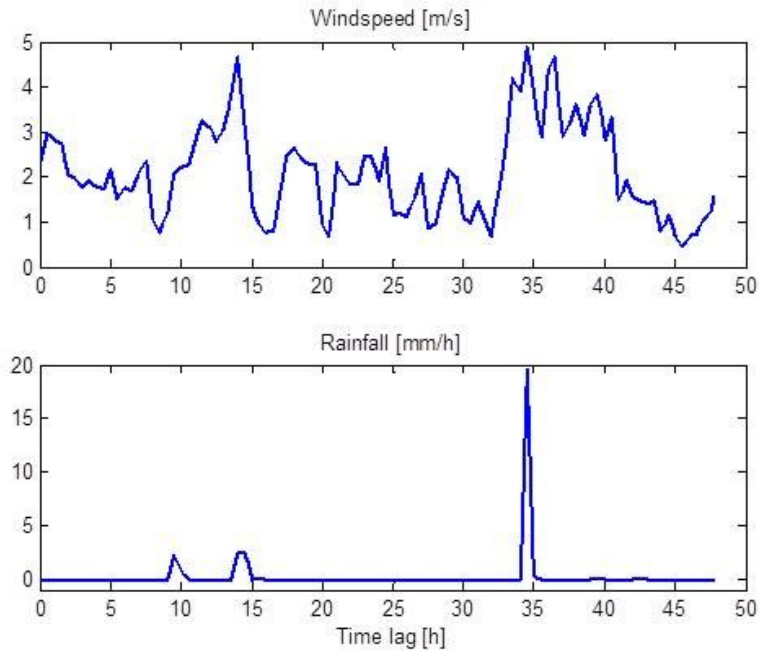


Figure 67: The wind speed and rainfall in-situ data corresponds with the measurements, starting from midnight Y2011-M10-D11 00H00.

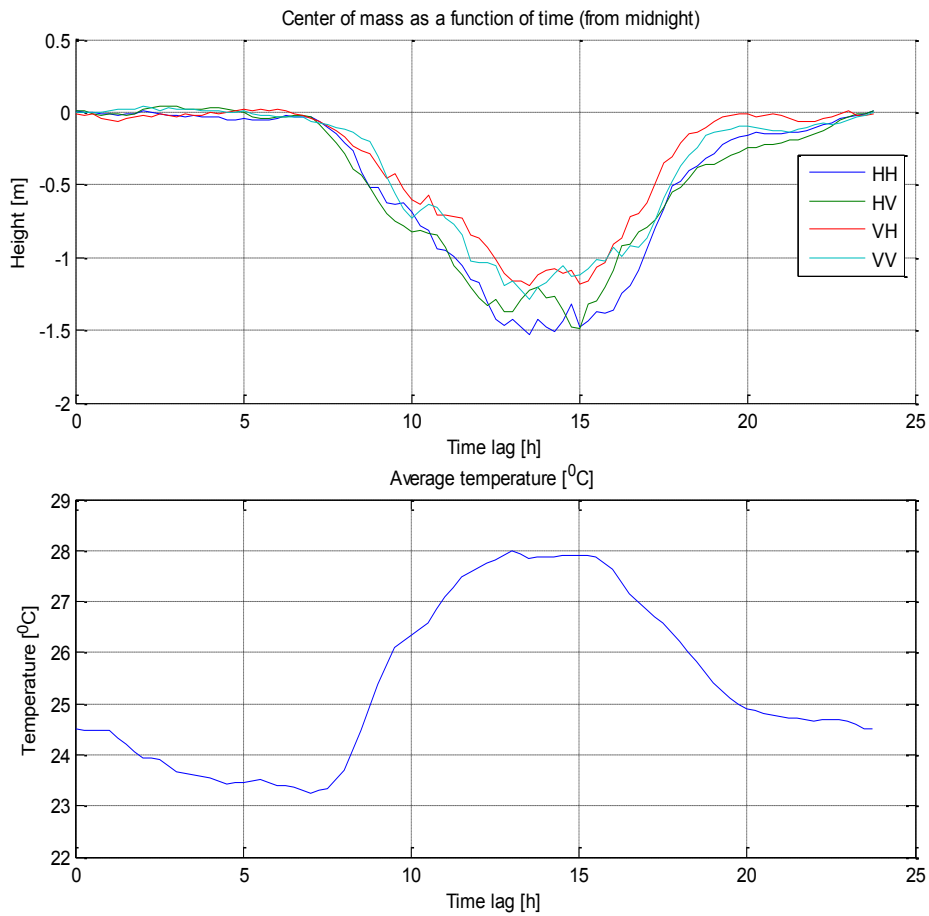


Figure 68: Top panel: Phase center height; Bottom: Temperature.

Another interesting finding resulting from the tomograms is that the location of the forest center of mass is observed to go up and down by more than 1 m during day hours, as shown in Figure 68.

The strong correlation with temperature variation over one day seems to suggest this phenomenon may be connected to the water content within the vegetation layer. One possible explanation considers evapotranspiration phenomena [Campbell00]. There is heat and mass transfer between forest organisms and their surroundings. With changing temperature, the exchange of oxygen and carbon dioxide between leaves and the atmosphere varies. This leads to changes of the water content inside the trunks. The forest stores water inside them overnight; in the morning, with higher temperatures and in the afternoon when the temperature goes down again, the center of mass shifts.

5.2.4. COHERENCE MATRIX ANALYSIS

As shown above, the TropiScat experiment makes it possible to produce a vertical section of the illuminated forest every hour. This means that it is possible to analyze the temporal behavior of the forest at different heights, allowing considering ground, lower, middle and upper vegetation separately.

The instrument used in this section to perform this analysis is the so-called *coherence matrix*. For a set of N acquisitions, the coherence matrix is defined as the NxN matrix obtained by taking the N^2 interferometric coherences of all available interferometric pairs. In the remainder we will discuss the temporal behavior at different height locations within the vegetation by considering the coherence matrix corresponding to each layer.

COHERENCE OVER 24 HOURS

In this section we examine temporal coherences over a time span of 24 hours. Figure 69 shows HV coherency matrices over one day at the ground layer (0 m), and at 10 m and 20 m above the ground. Each entry in the three matrices has been obtained by taking the interferometric coherence between two different acquisition times at one particular location within the forest. Coherence evaluation has been carried out by employing an averaging window of 5m x 40m (height-range), corresponding to about 50 looks. All the examined coherence matrices were extracted by considering the near range area (about 85 m away from the VNA), where vertical resolution is finer. The same analysis is extended to all polarizations in Figure 70

In both figures it is observed that the lowest coherence values are associated with day-time acquisitions. This result is consistent with the defocusing phenomena discussed in the previous section, where it was shown that day-time acquisitions are perturbed by the action of the wind. It is worth noting that this phenomenon is partly observed at the ground level as a result of defocused contributions from the rest of the vegetation layer. Night acquisitions are instead observed to produce the highest coherence values. However, the most relevant phenomenon is that night-time acquisitions yield high coherence values, not only at very short time lags (i.e.: few hours), but even at 20 hours or more.

This result suggests that performance over tropical areas can be optimized by gathering the data within a temporal window ranging from approximately 7 PM to 7 AM. For this reason, the next sections will be focused on the evaluation of the long term temporal coherence at dawn and dusk times.

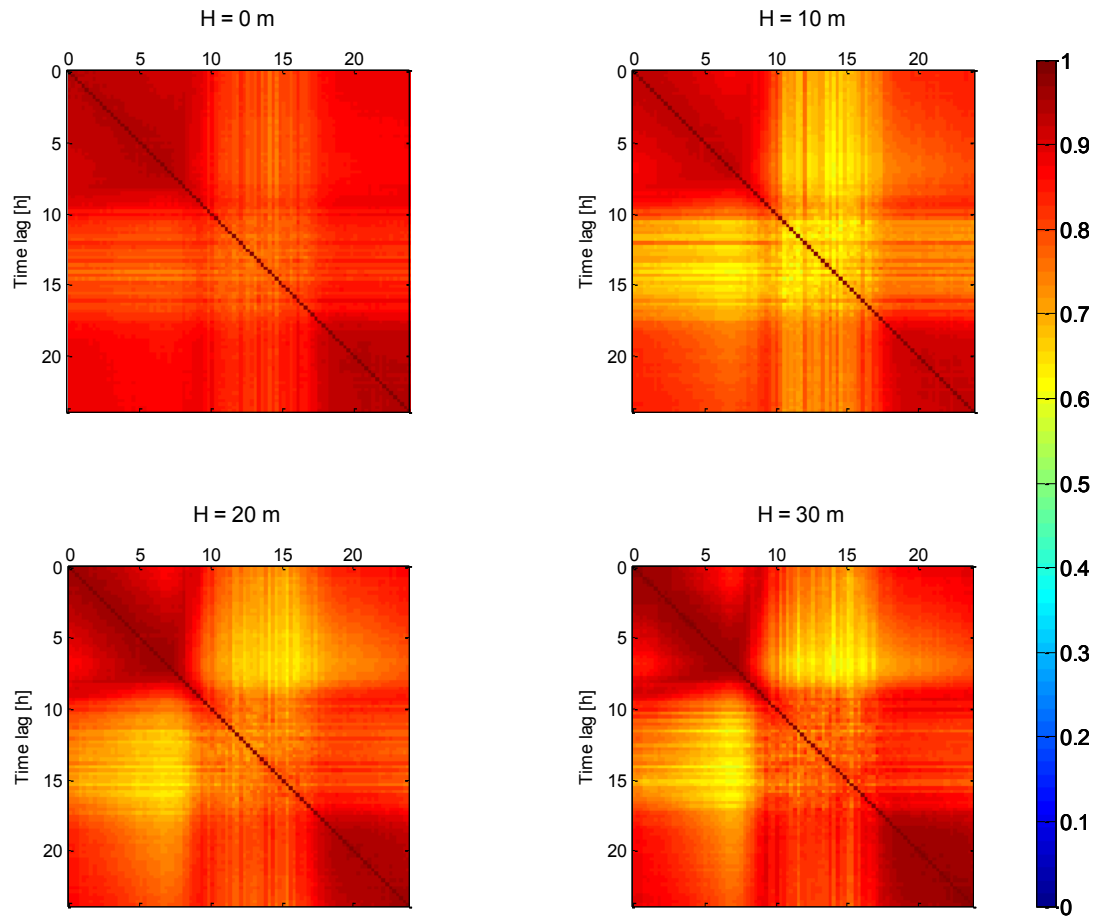


Figure 69: HV coherence matrices over 24 hours for four layers.

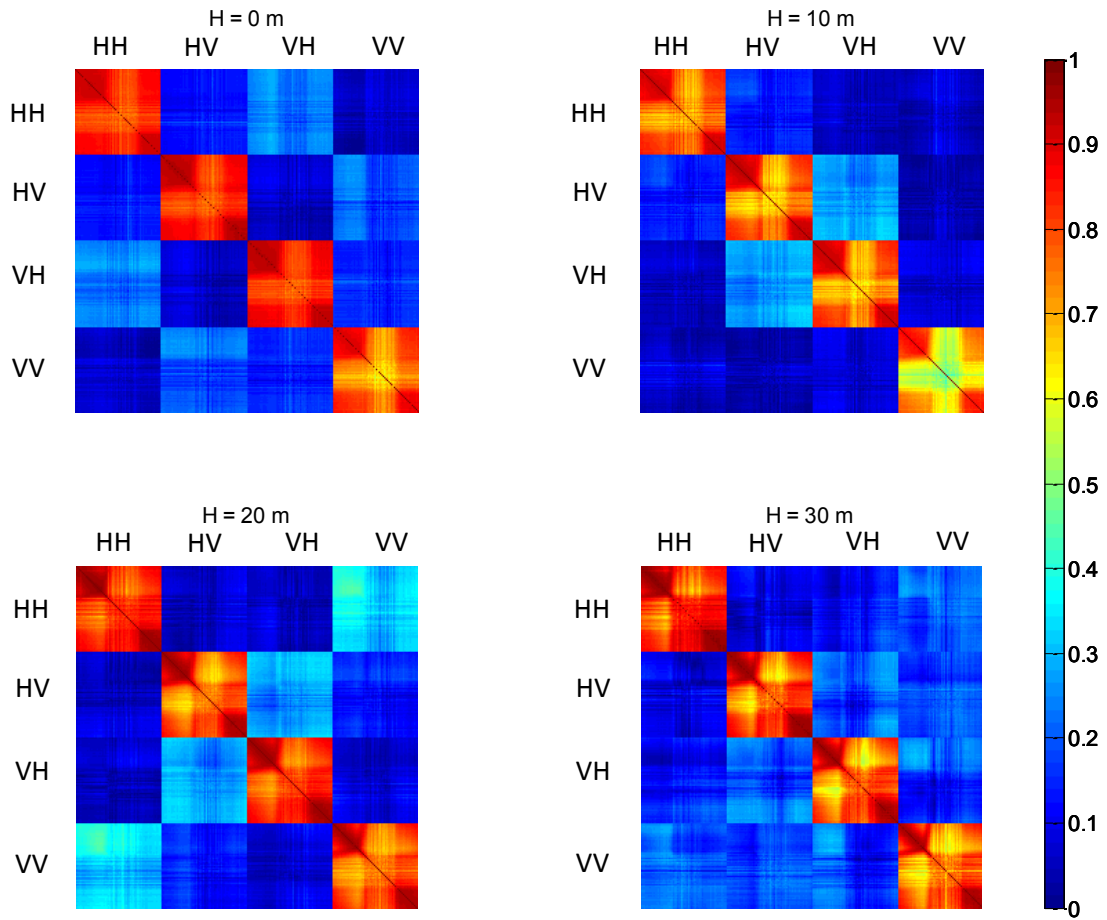


Figure 70: Full-pol coherence matrices over 24 hours.

DUSK-DUSK LONG TERM COHERENCE

Figure 71 shows the coherence matrix at HV as a function of forest height (0m - 10m – 20m and 30m). All acquisitions are gathered at 7 PM. The considered time span is 35 days, starting from is Y2011-M12-D07.

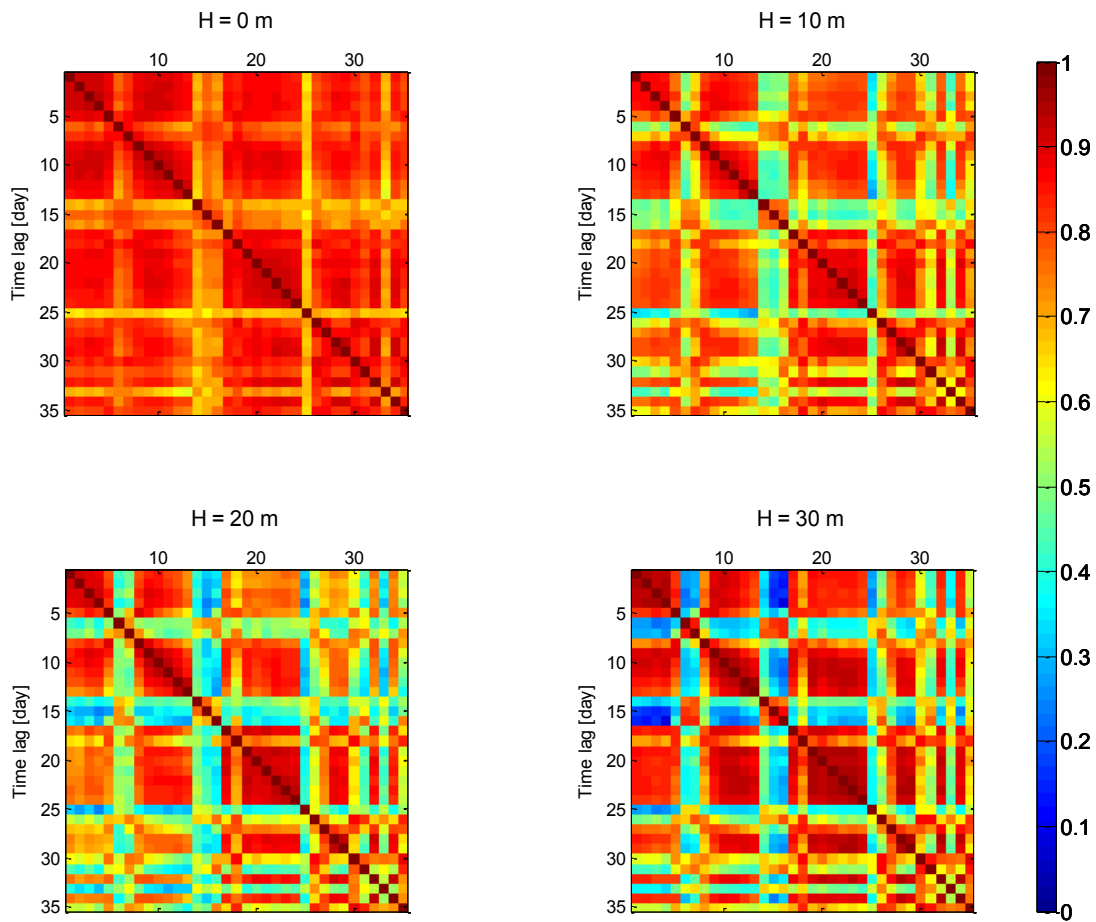


Figure 71: HV dusk-dusk coherence matrices over 35 days.

We again notice a regular decline of coherence moving away from the main diagonal which corresponds to increasing time lag. Still, the observed behavior looks a bit random, showing both high and low coherence values. This behavior was found to be associated to rainfall events. For this reason the analysis will be carried out in the remainder without considering rainy days.

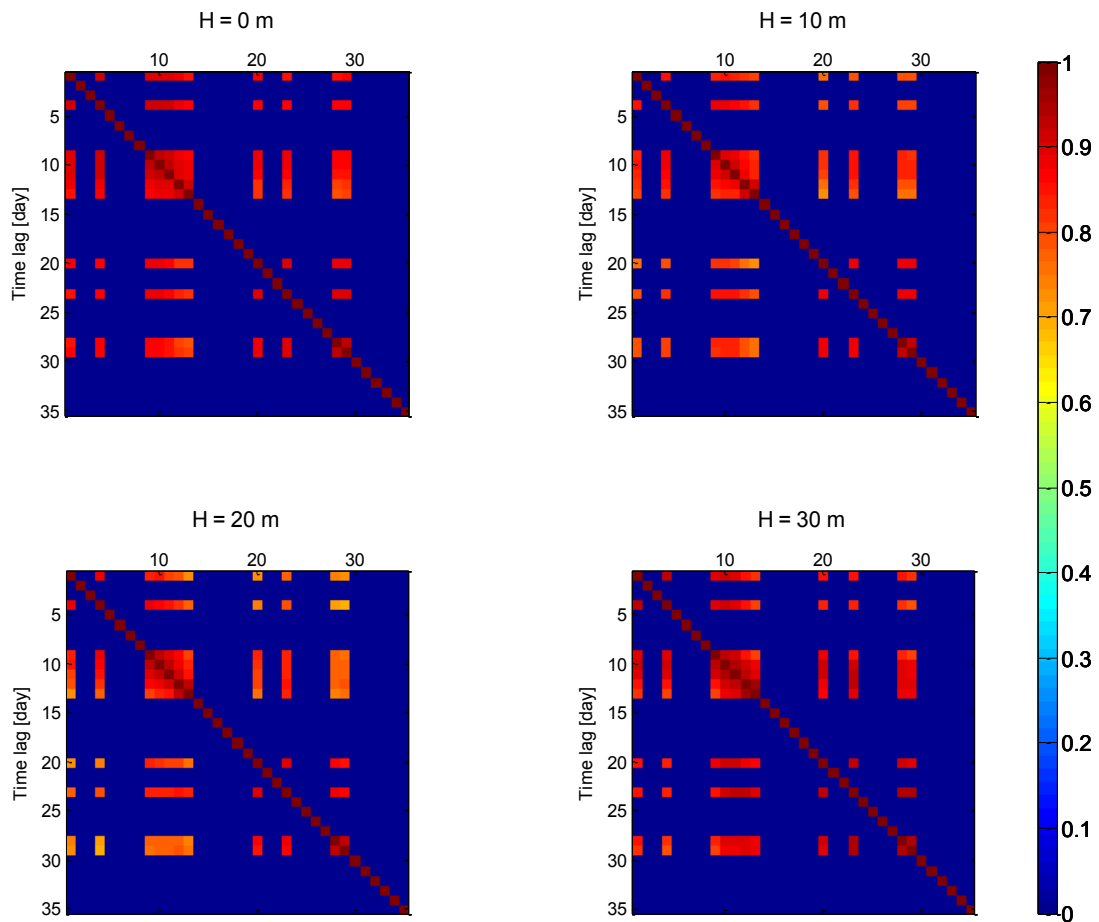


Figure 72: HV dusk-dusk coherence matrix with dry days.

The result is presented in Figure 72, where it is possible to see that temporal coherences gradually decrease as a function of the acquisition time. We then conclude that rainfall events do affect significantly the data. Still, rainfall effects vanish within a few hours after the rain stops, enabling long term coherence analysis.

The same analysis is extended to all polarization in Figure 73. It is easy to see that the same temporal behavior is observed in all polarimetric channels.

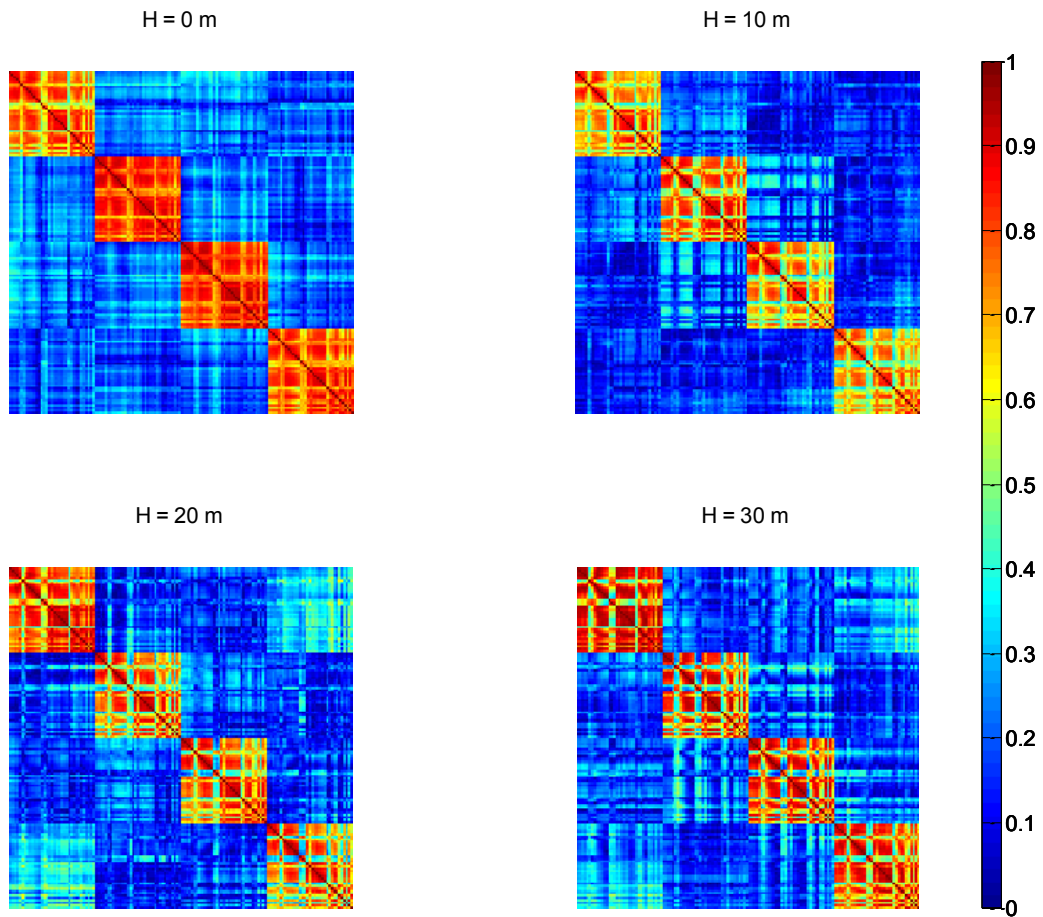


Figure 73: Full-pol dusk-dusk coherence matrices over 35 days.

DAWN-DAWN LONG TERM COHERENCE

Figure 74 shows the coherence matrix at HV as a function of forest height (0 m – 10 m – 20 m and 30 m). All acquisitions are gathered at 6 AM. The considered time span is 35 days, starting from is Y2011-M12-D07.

The observed coherence values are only slighter lower than in the dusk-dusk case. Beside this, it is easy to recognize the same behavior as in the dusk-dusk case.

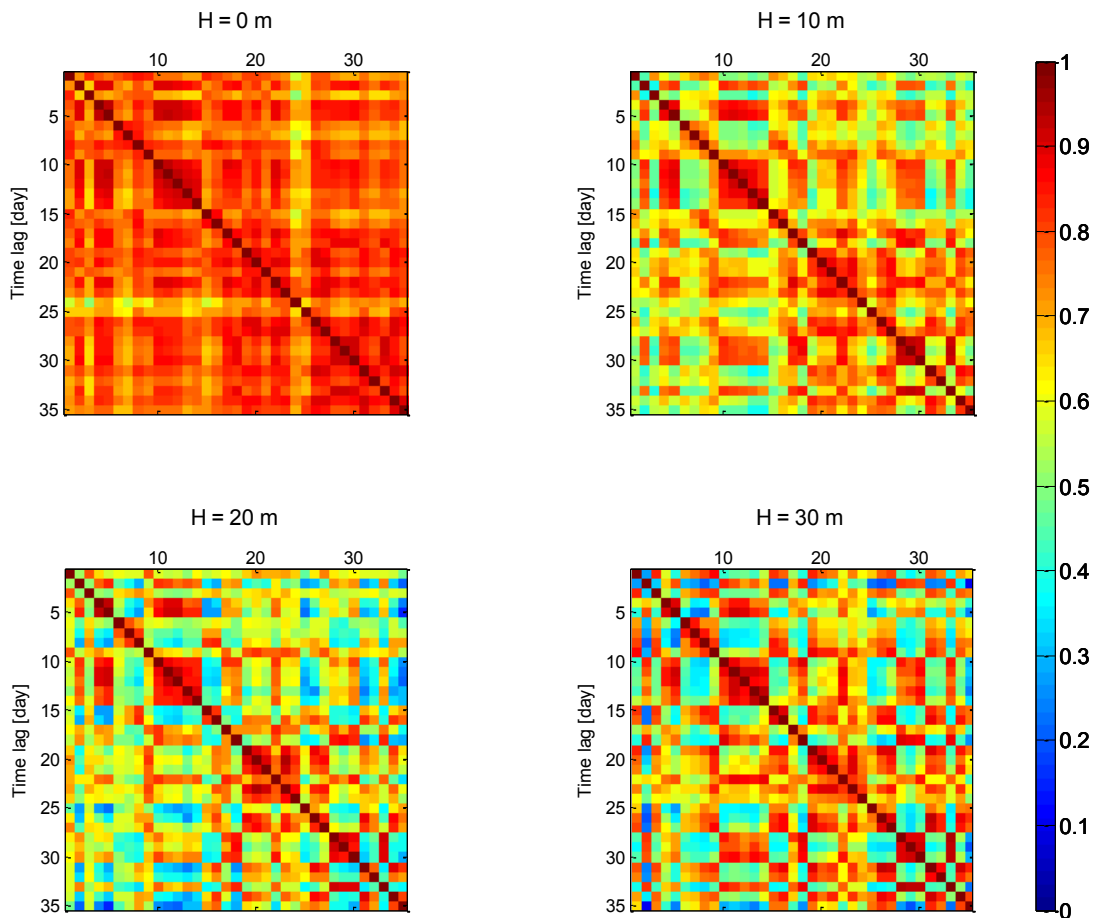


Figure 74: HV dawn-dawn coherence matrices over 35 days.

5.2.5. TEMPORAL COHERENCE AS A FUNCTION OF VERTICAL STRUCTURE

The aim of this section is to establish a link between temporal coherence and vertical structure by analyzing how coherence changes over time at different heights within the vegetation layer.

We decided to focus on dawn-dawn rather than dusk-dusk acquisitions since the ionospheric disturbances are much stronger at dusk-time. As highlighted above, rainfalls have been observed to affect the electromagnetic response of the tomographic array until a few hours (about 4-5 hours) after the rain stops. Accordingly, rainy days have been excluded from the analysis.

The analysis within this section covers the time span from December 2011 to March 2012. Data from the dry season will be discussed in the next section.

COHERENCE ESTIMATION

Coherence estimation was carried out through both spatial and temporal averaging. Spatial averaging was performed in a space varying fashion (see Figure 75), in order to have the same equivalent number of looks at each range, height location.

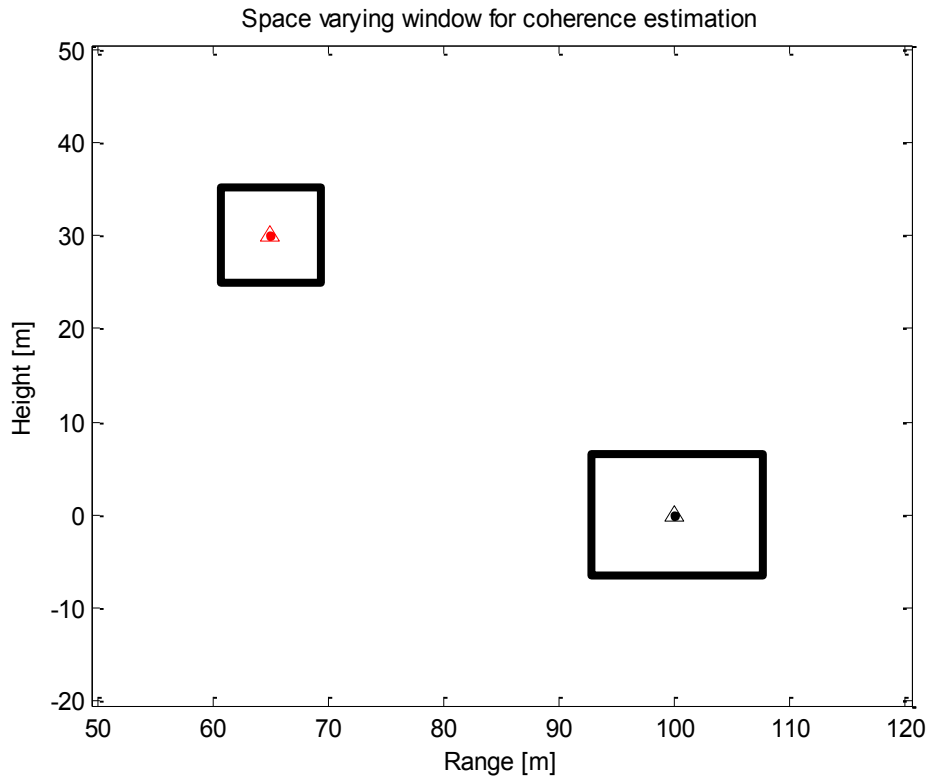


Figure 75: Space varying window for coherence estimation.

Temporal averaging was carried out by taking all pairs in the data set, spanning the same interval (for example, all the pairs with a temporal baseline of 3 days or 25 days), and averaging their coherence to make the estimates more robust.

The resulting number of looks due to spatial averaging is 20. This number is then incremented by using multiple temporal snapshots.

TEMPORAL COHERENCE MAP

The aim of this section is to produce a ground range, height map of the dawn-dawn temporal coherence of the illuminated scene.

The estimated coherence maps at 4 and 17 days at HV are reported in Figure 76. Coherence at 4 days is observed to be remarkably high both at ground and canopy level. Passing from 4 to 17 days the ground coherence is observed to stay high, whereas volume coherence tends to decrease, therefore witnessing coherence sensitivity to height.

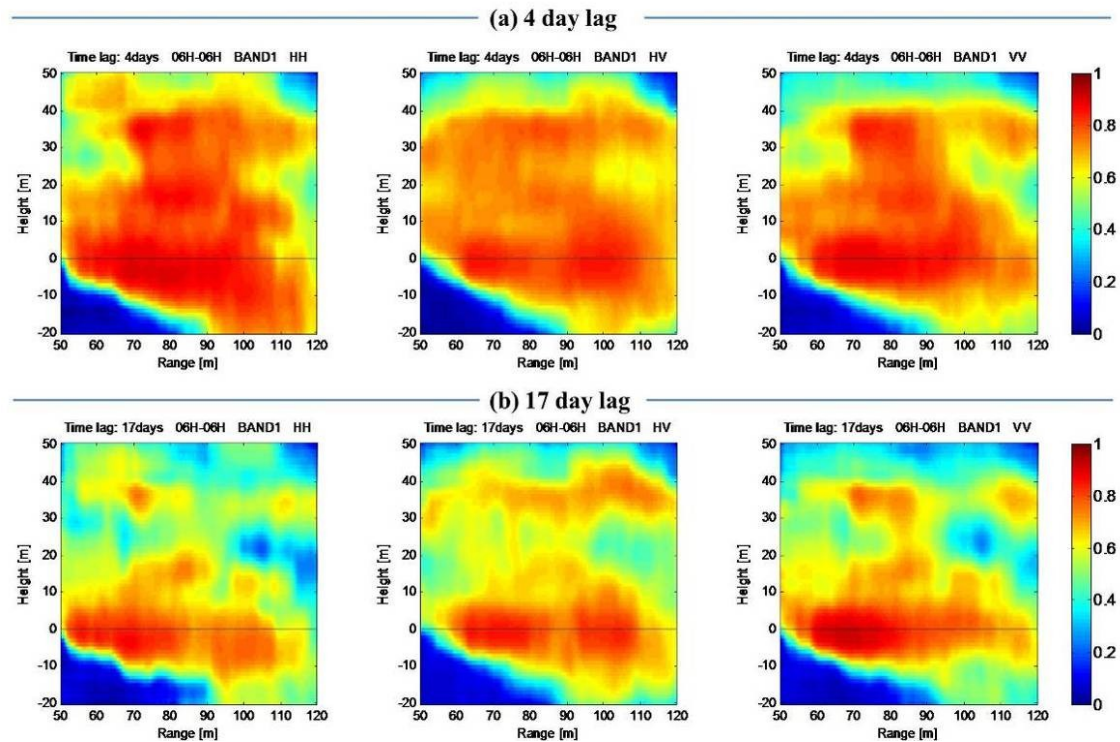


Figure 76: (a) Dawn-dawn temporal coherence after 4 days; (b) Dawn-dawn temporal coherence after 17 days.

TEMPORAL DECORRELATION MODELLING

The observed behavior of temporal coherence versus time suggests that it can be modeled effectively as an exponential decay with an initial value and a time constant. The time constant provides an idea of the lifetime of the scatterers, whereas the initial value accounts for short time changes, as well as for clutter.

We assume that the elemental scatterers in the resolution cell suddenly change their reflectivity, passing from complete coherence to zero. Once a start time is set ($t_0 = 0$), the scatterers are divided in two classes: those that have experienced at least one change and those that have not. The model simply can be written as follows:

$$\gamma(nT) = \gamma_0 e^{-nT/\tau_0}$$

Equation 13

The term γ_0 , the initial coherence, represents the fraction of the scatterers that did not suffer from a “quick decorrelation” mechanism and τ_0 is the time constant.

Parameter estimation was carried out through L1 norm minimization.

Figure 77 shows the initial coherence, which is observed to be quite uniform and pretty high. The time constant is instead observed to be much more varying, as shown in Figure 78. Again, it is easy to see the ground level is the most stable due to the long time constant.

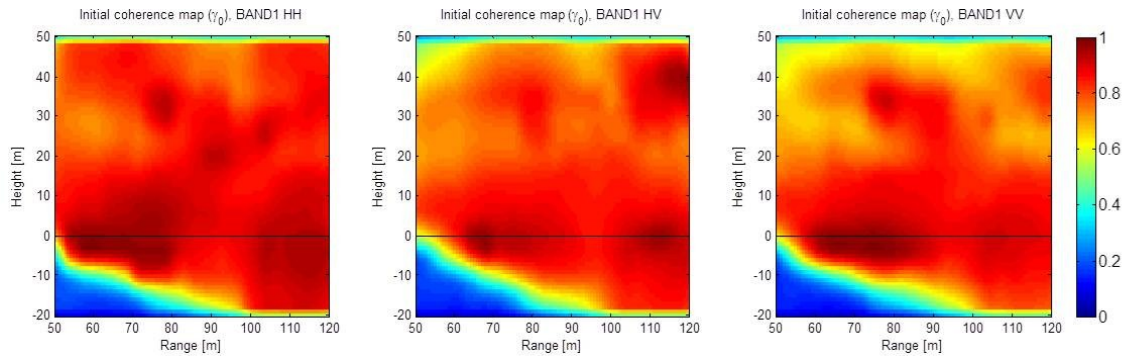


Figure 77: Initial coherence map

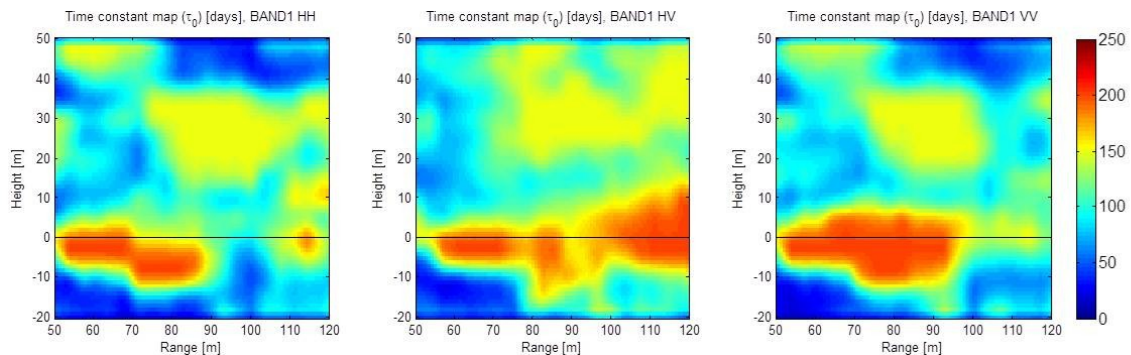


Figure 78: Time constant map

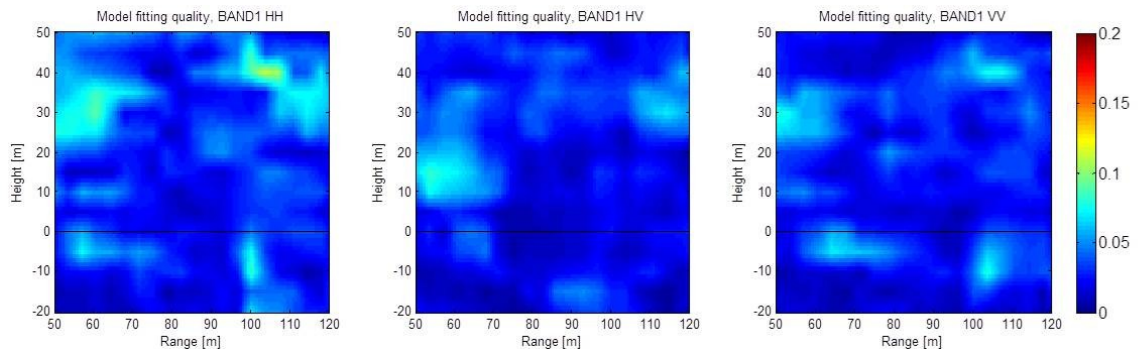


Figure 79: Model fitting quality map

Figure 79 reports the resulting figure of merit relative to model fitting, which is obtained as the average absolute difference between the estimated coherence model identified and the coherence. The difference is observed to be very low ($\ll 0.1$), showing that that the model is well fit to the data.

EXPECTED TEMPORAL COHERENCE (DECEMBER-MARCH)

The results shown in this section are here summarized in Figure 80 and in Table 1, which were obtained by averaging the estimated temporal coherence for each layer over an incidence angle span ranging from 20° to 40° . Based on this analysis, temporal coherence at the ground level is expected to stay higher than 0.8 at 27 days in all polarimetric channels. Coherence at canopy height is expected to be about 0.8 at 4 days and

about 0.65 at 27 days. The implications of these results on BIOMASS tomography will be discussed in the section dedicated to WP 40.

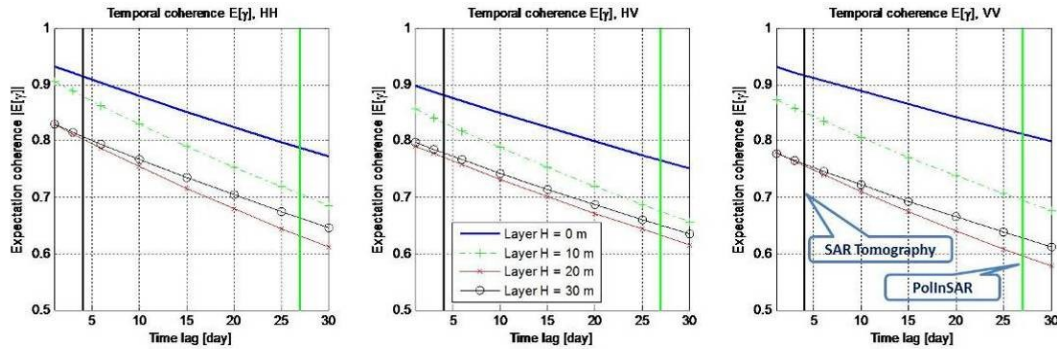


Figure 80: Dawn-dawn temporal coherence at P band (excluding rainfalls). The black and green vertical lines indicate the 4 and 27 day repeat pass time foreseen for the BIOMASS mission

Layer	HH		HV		VV	
	4 days	27 days	4 days	27 days	4 days	27 days
0 m	0.93±0.03	0.81±0.04	0.91±0.02	0.80±0.02	0.95±0.02	0.84±0.02
10 m	0.89±0.02	0.71±0.04	0.84±0.02	0.67±0.03	0.86±0.02	0.70±0.06
20 m	0.80±0.04	0.62±0.07	0.77±0.02	0.63±0.03	0.76±0.04	0.59±0.05
30 m	0.80±0.06	0.66±0.08	0.77±0.04	0.64±0.05	0.74±0.08	0.61±0.09

Table 1: Expected dawn-dawn temporal coherence (excluding rainfalls) as a function of height at 4 and 27 days.

5.2.6. TEMPORAL COHERENCE DURING THE DRY SEASON

This section aims at investigating the results of P-band tomography temporal coherence at dry period. The analysis here presented is based on considering dawn time acquisitions from September 2012 to November 2012, in the frame of the ESA campaign TropiScat.

ISSUE NOTE

This analysis is presented in a separated section as data from April to August 2012 do not appear to be fully consistent with those acquired previously; in that both amplitude and phase unbalances were observed that partly hindered the tomographic focusing. Such unbalances are most likely to be due to hardware problems occurred in spring/summer 2012.

Figure 81 reports the range response of the trihedral reflector in all 15 antenna pairs, as measured in October 2011 (top) and November 2012 (bottom).

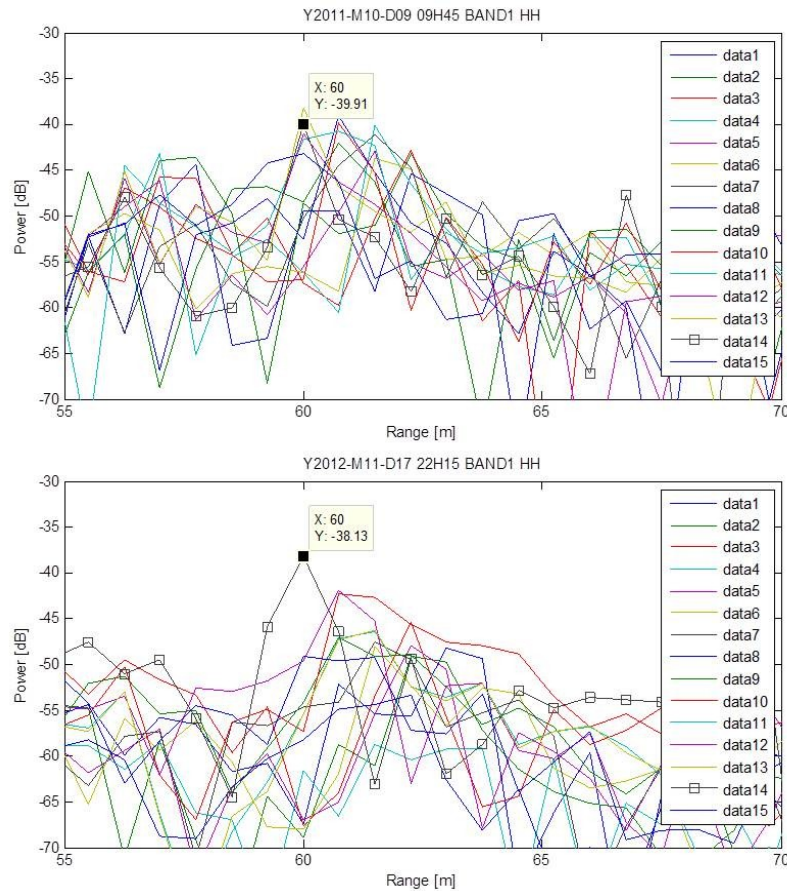


Figure 81: Trihedral range response in October 2011 (top) and November 2012 (bottom).

The data tip indicates pair 14 (Tx 5 – Rx 3), for which the power and the range location of the trihedral corner are the same. The other pairs, instead, show differences between the two acquisition times as for both power and range location. Such differences appear to have a space varying component, as it was not possible to compensate for them simply by using the information about the corner position and power.

RESULTS

Figure 82 reports the estimated dawn-dawn (6 AM) temporal coherence map at 4 and 17 days, as obtained by processing data from September to November 2012.

The first relevant observation to be made is that the estimated coherences exhibit values comparable or higher to those observed from November 2011 to March 2012, despite the aforementioned side-lobe problems. These results can be imputed to the fact that coherence was estimated through spatial and temporal averaging, which helped mitigating side-lobes.

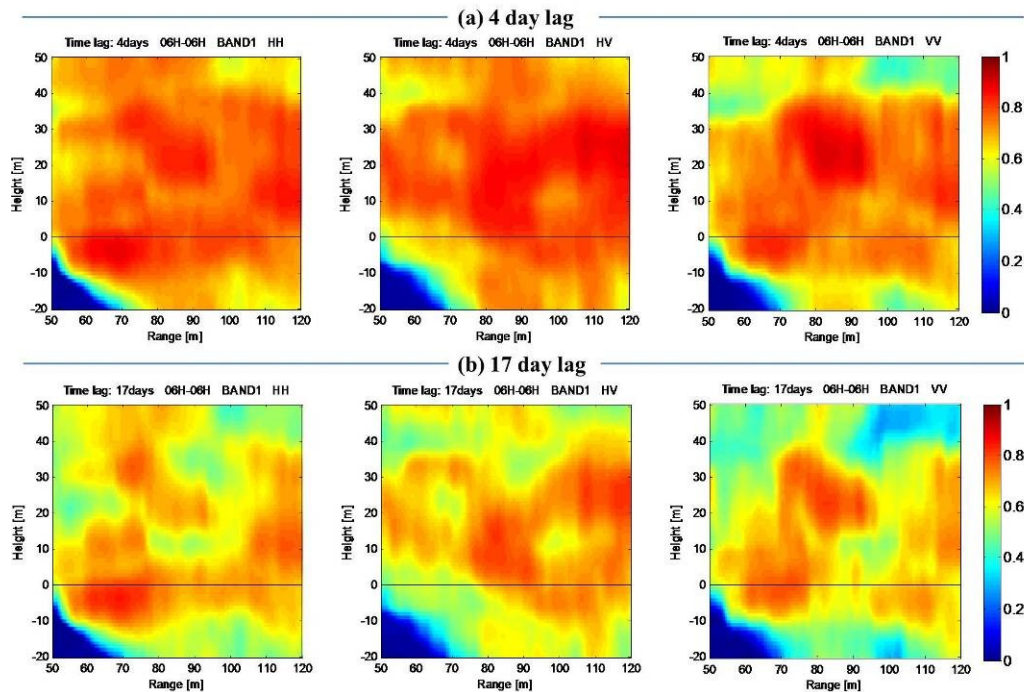


Figure 82: Dry season: (a) Dawn-dawn temporal coherence after 4 days ; (b) Dawn-dawn temporal coherence after 17 days

5.2.7. CONCLUSIONS

Tomographic processing was aimed at investigating the link between the variation of temporal decorrelation over time and forest vertical structure at P-Band. To this aim all available acquisitions were focused in the range, height plane so as to form a vertical section of the illuminated forest. Temporal coherence was then investigated by analyzing the time series composed by multiple tomographic snapshots.

The fine time sampling of the TropiScat experiment allowed observing the temporal variation of the forest accurately, resulting in the first (at least to our knowledge) tomographic movie capturing the forest daily change.

This analysis revealed a diurnal vertical motion of the forest center of mass. This phenomenon is strongly related to daily temperature variations, which suggests a connection with forest evapo-transpiration phenomena.

Concerning short time temporal coherence, the most relevant phenomenon is the coherence drop during daytime, due to the effect of the wind moving the forest canopy.

This result already appears to provide a very useful input concerning the BIOMASS mission, as it suggests that performance over tropical forest could be optimized by gathering acquisitions at dusk or dawn time.

Long term coherence was analyzed by considering the periods from November 2011 to March 2012 (rain season) and September 2012 to November 2012 (dry season). We decided to focus on dawn-dawn rather than dusk-dusk acquisitions since the ionospheric disturbances are more severe at dusk-time. Rainfalls have been observed to affect the electromagnetic response of the tomographic array until a few hours (about 4-5 hours) after the rain stops. Accordingly, rainy days have been excluded from the analysis.

The analysis has shown that the estimated temporal behavior does change within the forest volume, in that the highest coherence values are observed at the ground level. Temporal coherence at the ground level is expected to stay higher than 0.8 at 27 days in all polarimetric channels, whereas coherence at canopy height is expected to be about 0.8 at 4 days and about 0.65 at 27 days. Finally, we remark that no relevant

difference was observed between the rain and dry seasons. This is indeed due to the fact that we excluded rainy days from the analysis.

The implications of these results on BIOMASS tomography will be discussed in the section dedicated to WP 40.

5.3.WP 33: DATA INVENTORY

All data (RF measurements and in-situ data) collected during the experiment are stored in a MySQL database. By this way, we can easily apply SQL transactions to find, sort and filter the large amount of data files for processing.

For example, the following transaction return all filename containing RF data from date1 to date2 in HV polarisations:

```
SELECT filename FROM tropiscat WHERE DATE>date1 AND DATE<date2 AND POLAR='HV' ORDERED BY DATE
```

If we want to filter data without rain fall

```
SELECT filename FROM tropiscat WHERE DATE>date1 AND DATE<date2 AND POLAR='HV' AND insitu.rain=0 ORDERED BY DATE
```

A full description of the data list is given in the Data Acquisition Report.

6. WP 40 TROPISAR DATA REPROCESSING

This part as been added to the work by a Contract Change Notice (CCN). As proposed in the technical proposal, this study has been organized into 5 Work Packages:

- WP 41: Reprocessing of TropiSAR data
- WP 42: PolInSAR forest height retrieval
- WP 43: Performance analysis PolInSAR and Backscattering coefficient
- WP 44: Performance analysis tomography
- WP 45: Conclusions and recommendations.

6.1.WP41: REPROCESSING OF TROPISAR DATA

6.1.1. SAR DATA ACQUISITION SCHEDULE

The TROPISAR SAR acquisition campaign was focused on two specific sites in French Guiana [Dubois-Fernandez et al., 2012]. These two sites are Paracou and Nouragues. These sites were first defined in 1982 for Paracou and 1986 for Nouragues and have been extensively monitored and characterized since then under the responsibilities of CIRAD and CNRS.

The Airborne campaign took place in August 2009 with the SETHI airborne SAR system from ONERA. The TROPISAR campaign was organized around one validation flight and 6 data acquisition flights. Table 1 provides the schedule of the different flights.

Flight Identifier	Flight Description	Flight date	Frequency bands
VOL0	Validation	10/08/2009	P + L
VOL1	Standard Zero-baseline	12/08/2009	P + L
VOL2	Tomo Nouragues	14/08/2009	P + L
VOL3	Standard	17/08/2009	P + L
VOL4	Tomo-Paracou	24/08/2009	P + L
VOL5	Standard + marais de Kaw	30/08/2009	P + L
VOL6	Standard Zero-baseline	01/09/2009	P + L

Table 2: SAR data acquisition calendar

6.1.2. THE SETHI SAR SYSTEM AND ACQUISITION RADAR PARAMETERS

SETHI combines two pods positioned under aircraft wings which are able to carry heavy and bulky payloads of different kinds ranging from VHF to X band and/or optical sensors with a wide range of acquisition geometries (Figure 1) [Bonin et al, 2009]. The system parameters are listed in Table 2.



Figure 83: The Falcon 20 carrying the SETHI system. The two pods contain the radar antennas.

Parameter	P-band	L-band
<i>Geometry</i>		
Altitude [ft,m]	13000/ 3962	
Velocity [m/s]	120	
Antenna		
Elevation aperture [°]	100	20
Azimuth aperture [°]	60	16
<i>Waveform</i>		
Mode	Full-Polar	Full-Polar
Peak Power [W]	500	200

Actual PRF [kHz]	2.5	5
Sampling rate [MHz]	500	500
Bandwidth [MHz]	260-460	1250-1400
Processed wave length [m]	0.652 – 0.896	0.214-0.24
Processed Bandwidth [MHz]	335-460	1250-1400
Relative bandwidth [%]	31	11
Range Resolution [m]	1.2	1.0
Azimuth resolution [m]	1.5	1.0
Range pixel spacing [m]	1.0	0.75
Azimuth pixel spacing [m]	1.0	0.75
Near Range [m]	4350	4350
Nb of pixels in range	4000	2600
Incidence angle range [°]	24-62	24-47

Table 3: Radar system parameters.

The initial processing covered the frequency range 335MHz- 460MHz, resulting in a 125MHz bandwidth.

BIOMASS mission, because of international regulations on the use of radio frequency bands allocating the electromagnetic spectrum, is restricted to a bandwidth of 6MHz centred at 435MHz [Le Toan et al., 2010]

In this study, selected acquisitions from the TROPISAR campaign were reprocessed in order to match the 6MHz BIOMASS limited bandwidth.

6.1.3. SAR DATA ACQUISITION FLIGHT DESCRIPTION AND LIST OF REPROCESSED IMAGES

During the TropiSAR campaign, 7 flights were completed between the 10/08/2009 and the 1/09/2009.

Different planned baselines are available. ZB means Zero-baseline and corresponds to acquisitions along the reference trajectory. B1, B2, B3, B4, B5 indicates that the trajectory flown is lower than the reference one with a vertical shift of 50ft, 100ft, 150ft, 200ft and 250 ft respectively.

The images to be reprocessed are listed in Table 3:

Site	Acquisition identifier	Planned line	Date
Paracou	Tropi0007	ZB	10/08/2009
Paracou	Tropi0104	ZB	12/08/2009
Paracou	Tropi0208	ZB	14/08/2009
Paracou	Tropi0305	ZB	17/08/2009
Paracou	Tropi0402	ZB	24/08/2009
Paracou	Tropi0403	B1	24/08/2009
Paracou	Tropi0404	B2	24/08/2009
Paracou	Tropi0405	B3	24/08/2009
Paracou	Tropi0406	B4	24/08/2009
Paracou	Tropi0407	B5	24/08/2009
Paracou	Tropi0506	ZB	30/08/2009
Paracou	Tropi0603	ZB	01/09/2009

Table 4 : List of images to be reprocessed

6.1.4. PROCESSING WORKFLOW

We begin by detailing the initial processing steps and then describing the 6 MHz processing.

SUMMARY OF THE 125MHZ PROCESSING

The 125MHz processing can be summarised as follows:

- Archiving the raw data
- IMU-GPS trajectory hybridation
- Demultiplexing the data
- SLC processing
- SLC post processing (calibration)
- Ground projection to obtain the data in geographic projection.

The details of each individual steps can be found in the final report of the TROPISAR campaign [Dubois-Fernandez et al., 2011]. We chose to outline here only the points which are relevant for the reprocessing.

The SLC processing is performed with PAMELA software, the ONERA SAR processor. It was decided to use a flat earth geometry for focusing purposes for the following reasons:

- There is no precise DEM covering the full zone
- The SRTM DEM is signing the top of the vegetation and not the ground, introducing a variable vertical shift reflecting the vegetation height of the order of 30m or more.
- The topographic excursion is of the order of 30m, comparable to the error associated with the vegetation height.

The SLC data is then post-processed. The post-processing consists in the radiometric and polarimetric calibration. The calibration parameters are computed based on the data acquisitions over the calibration site. In this case, the calibration site was located on the Rochambeau airport and included up to 6 reference targets, distributed in the range direction. The calibration factors are set uniquely for the whole campaign, one set of parameters for each frequency and the multiple acquisitions over Rochambeau can be used to assess the stability of the system over the campaign period. The secondary bounce of the wave on the wing results in an antenna pattern deformation. This deformation depends on (1) the frequency, (2) the incidence angle and (3) the polarization state. In order to remove this effect, we used the corner reflectors that have been placed across the swath on the calibration area. 5 trihedral corner reflectors were installed and several acquisitions were gathered using parallel tracks so that we have the frequency response of the corner reflectors for 11 incidences. By measuring the frequency response of each corner reflector on the images and interpolating these frequency responses in between, the residual radar transfer function was estimated and removed from the different channels.

SLC PROCESSING FOR THE 6 MHZ

Two options were explored in order to process the 6 MHz:

- Filtering of 6 MHz among the 125MHz of the range bandwidth.
- Filtering the raw data and re-processing the full dataset

The first option appeared at first like being the most straightforward. However several flaws were identified. The proper filtering of the SLC dataset, as performed by our processing software, preserves the centre frequency. Therefore, we could only obtain a SLC image corresponding to a center frequency of 397.5 MHz. Furthermore, we observed that the antenna pattern correction established over the full range of frequencies was not satisfactory when looking only at a small percentage of the bandwidth and the filtered image displayed unexpected radiometric variation as a function of range. The last but not least problem was associated with interferometric processing. If we filter the SLC images to reduce the range bandwidth, the resulting image will not integrate the frequency shift linked to the change of geometry in an airborne configuration.

The second processing option was therefore selected as the resulting dataset (tomographic) will be at the BIOMASS center frequency (first advantage) and take into account the varying interferometric frequency shift and resulting spatial decorrelation (second advantage). The reprocessing is however more involved as it requires starting over again from the raw data. Furthermore, the antenna pattern correction had to be re-established on the corner reflectors over the Rochambeau site. This was not possible over the 6MHz data because the signature from the corner reflector was not sufficient to correctly estimate the parameters. We therefore perform an intermediate processing over the Rochambeau area with a chirp bandwidth of 50MHz.

From these images, we derived the antenna pattern correction to be applied to the 6MHz dataset. Furthermore, a unique calibration key was computed from the corner reflectors to be applied to the 6MHz dataset.

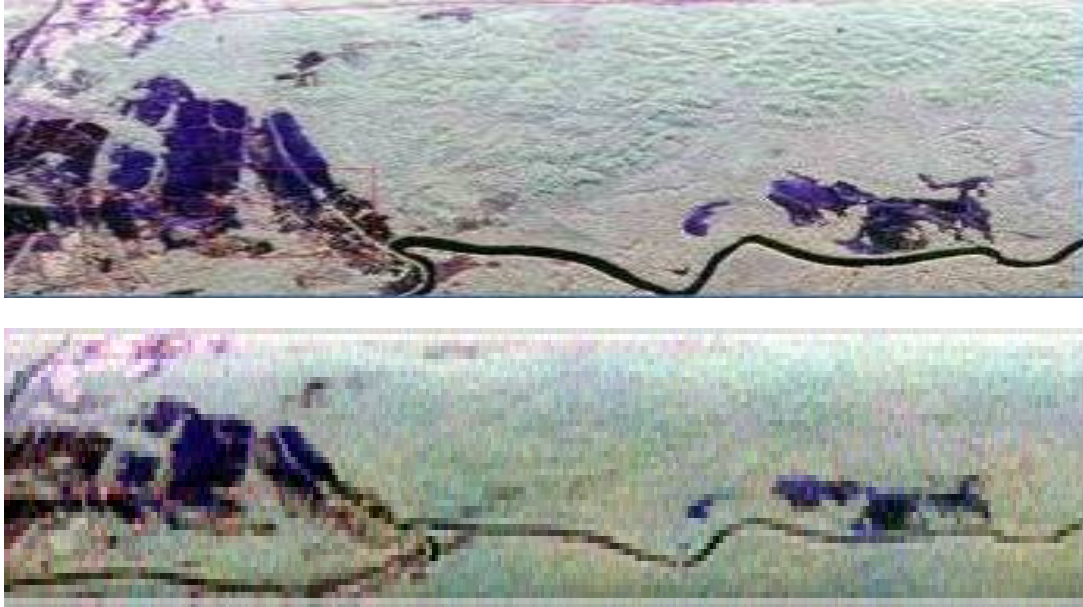


Figure 84 : Paracou images High resolution on top, low resolution on the bottom image – HH, HV, VV false color.

6.1.5. DATA QUALITY ASSESSMENT SUMMARY

The data quality parameters were estimated on the Rochambeau images (processed for the corner reflectors) for the calibration accuracy, on the Paracou image for the NE-Sigma0 and crosstalk level, the geometry accuracy is identical to the one associated with the TropiSAR full resolution delivery.

Calibration		
	Radiometric accuracy	+/- 0.8dB
	Co-polar phase accuracy	5°
NE-Sigma0 [dB]		
	25-50°	-34dB
Cross-Talk Level		-25dB
Geometric accuracy	(if altitude is known)	<10m

Table 5 : Data quality parameters

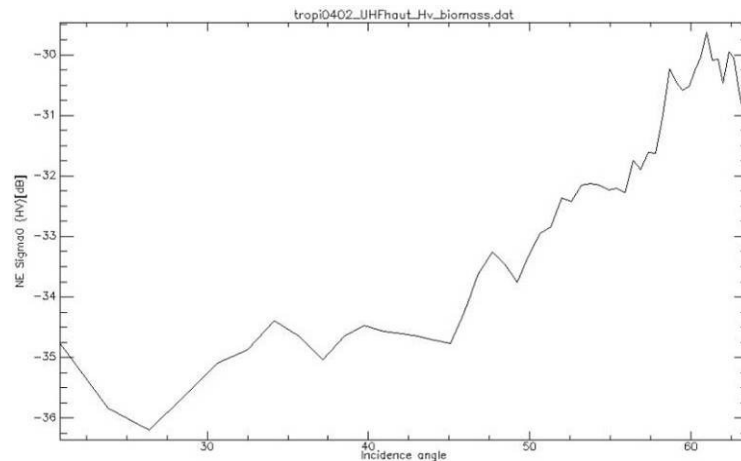


Figure 85 : Noise Equivalent Sigma0 as a function of incidence angle for the 6Mhz dataset

The noise equivalent sigma0 is computed based on the correlation between the HV and the VH channels.

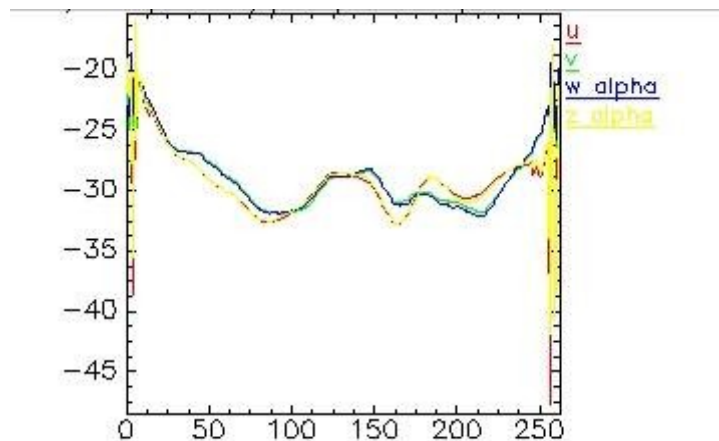


Figure 86 : Cross-talk parameters as a function of range bin

The cross-talk parameters are computed following the approach proposed in the Quegan paper [Quegan, 1994]

The data delivered to ESA and to the Partners are in the same format as the full resolution TropiSAR dataset. All the images are provided in the same radar geometry (they can be superposed readily). As a result, we have one grid file for the full dataset (*tropi0402_UHFhaut_biomass.grille*) and one ROI file (ENVI format Region of interest) (*tropi0402_UHFhaut_Hh_biomass.roi*)

The SLC dataset contains 8 files per dataset.

<i>tropi0402_UHFhaut_Hh_biomass.dat</i> ;	<i>tropi0402_UHFhaut_Hh_biomass.ent</i>
<i>tropi0402_UHFhaut_Hv_biomass.dat</i> ;	<i>tropi0402_UHFhaut_Hv_biomass.ent</i>
<i>tropi0402_UHFhaut_Vh_biomass.dat</i> ;	<i>tropi0402_UHFhaut_Vh_biomass.ent</i>
<i>tropi0402_UHFhaut_Vv_biomass.dat</i>	<i>tropi0402_UHFhaut_Vv_biomass.ent</i>

Transforming pixel position to latitude and longitude

Being able to link precisely one pixel on the image to one geographic location is essential. So is the reverse. In order to provide this correspondence independently of the altitude of the point (which we do not know

precisely as we do not have any precise DEM), we provide a file providing a transformation grid, called “*.grille”. The grid file allows to link a position in the image (x,y) associated with a height to a precise latitude and longitude. It can also be used to associate an image position and a height to a geographic position.

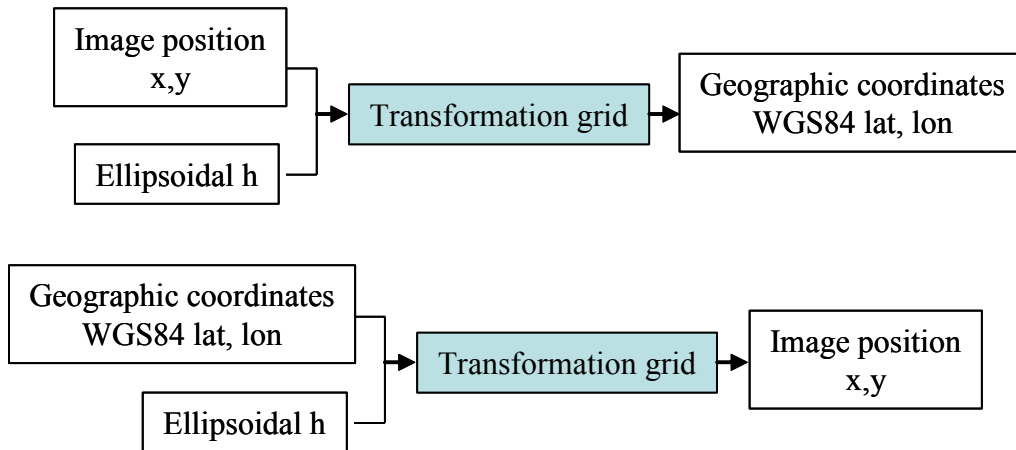


Figure 87: Geocoding process

This transformation grid file is a text file. The file starts with a short description indicating the relevant reference system, the desired accuracy. This value was used to compute the maximum step size in the three dimensions, range, azimuth and height such that the error resulting from a simple linear interpolation between the grid points will create an error below the requested accuracy. The first lines describe also the range of altitude as well as the number of steps in the line dimension (29 in the range direction), in the azimuth direction (129) in the altitude direction (58). The file contains then 29x129x58 lines listing x,y,h,lon,lat where x,y are the image pixel position in range and azimuth, h is the ellipsoidal height with respect to the GRS80 ellipsoid, and lon, lat are the longitude and latitude (E, N) in WGS84 system.

```

% Grille de georeferencement de l image tropi0402_Pcons_Hh_slc.1 calculee pour une
precision de 1.500000 m entre alt = -103.758803 m et alt = 301.638805 m

% format : ligne colonne altitude longitude latitude (longitude = latitude=0 si pas de
donnee )

% Les coordonnees geographiques sont exprimees en WGS84, les altitudes sont donnees par
rapport a l'ellipsoide de GRS 80

nb_lig 29
nb_col 129
nb_alt 58
10 0 -103.7588 -52.9161292218770 5.2460086137288
10 0 -103.5015 -52.9161376843845 5.2460097385163
...
  
```

Figure 88: beginning of a transformation grid file (...grille)

In order to use the grid, one way is to identify the two height levels framing the desired height. On each height layer, the desired localisation information is computed via a linear interpolation and a final interpolation is performed in the height direction to compute the localisation information.

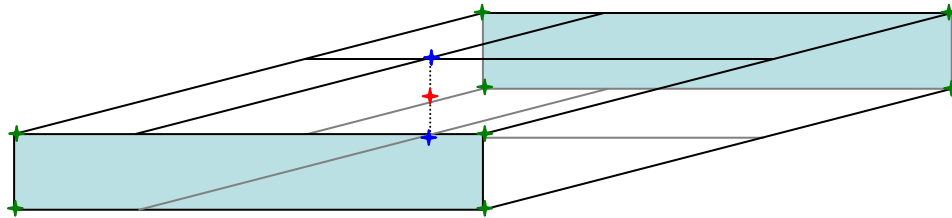


Figure 89: Computing the geographic position of the i,j,h pixel in red. First identifying the upper and - - lower layers, then on each layer, from the green points, compute the geographic position of the blue points, interpolate between the two blue points.

6.2.WP42 : POLINSAR FOREST HEIGHT RETRIEVAL

6.2.1. DISTORTION LINKED TO RADAR GEOMETRY AND PROPOSED COMPARISON APPROACH

The LIDAR canopy height information was provided by CIRAD and can be obtained directly from the Kourou Ecofog team. It was derived from the raw LIDAR information. The LIDAR canopy height information has a level of details not accessible to PolInSAR technique. The pixel posting is 1m for the DCM (Digital Canopy Model).

The PolInSAR inversion scheme will provide an undercanopy ground height and a vegetation height in radar geometry (by processing the SAR data using a sliding window). It is important to understand how this information can be analysed.

To illustrate the distortion caused by the radar geometry, let us assume a gentle topography with a constant vegetation height.

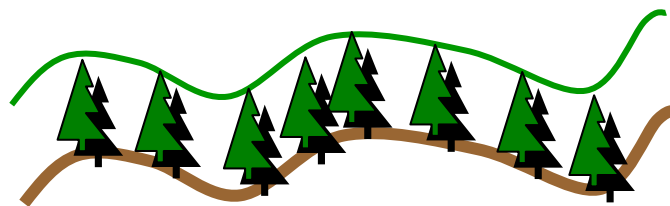


Figure 90 : Forest schematic for a constant vegetation height over a gentle topography.

The top of the tree is closer to the radar and as a result will be imaged in a range bin corresponding to a shorter range. If h_v is the vegetation height and θ the incidence angle, the ground shift is $h_v / \tan \theta$, e.g. a 69 m shift at 30° incidence for a 40m high canopy. The differential shift between the top of the tree and the base of the trunk is considered as constant in this illustration.

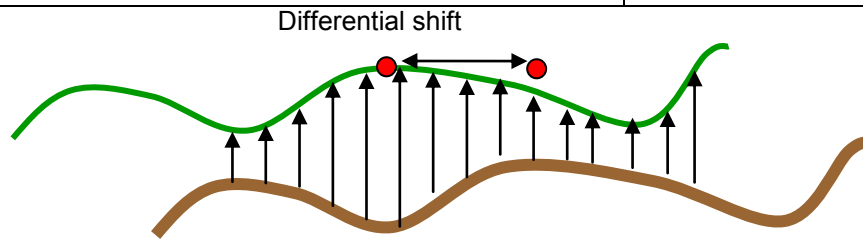


Figure 91 : Forest schematic in radar geometry for a constant vegetation height over a gentle topography. The differential range shift between the bottom of a tree and the top of its crown, (illustrated by the arrow) combined with the underlying topography will create an apparent vegetation height variation in the radar image.

The main consequence of the differential range shift between the top of the vegetation and the base of the trees in the case of underlying topography is that a constant vegetation height will translate into a varying observed vegetation height in radar geometry.

This needs to be taken into account when comparing the LiDAR and the PolInSAR inversion results.

Two options are then possible:

- Comparison in the radar geometry between the canopy height from LiDAR data and from PolInSAR.
- Comparison in the cartographic geometry or UTM map of the canopy height from LiDAR data and from PolInSAR

The schematic of the required projections and transformations is presented in Figure 10.

DEM is the digital elevation model associated with the ground surface under the canopy. DSM is the digital surface model, it corresponds to the elevation of the top of the tree. DCM is the digital canopy model, or vegetation height model. $DSM = DEM + DC$

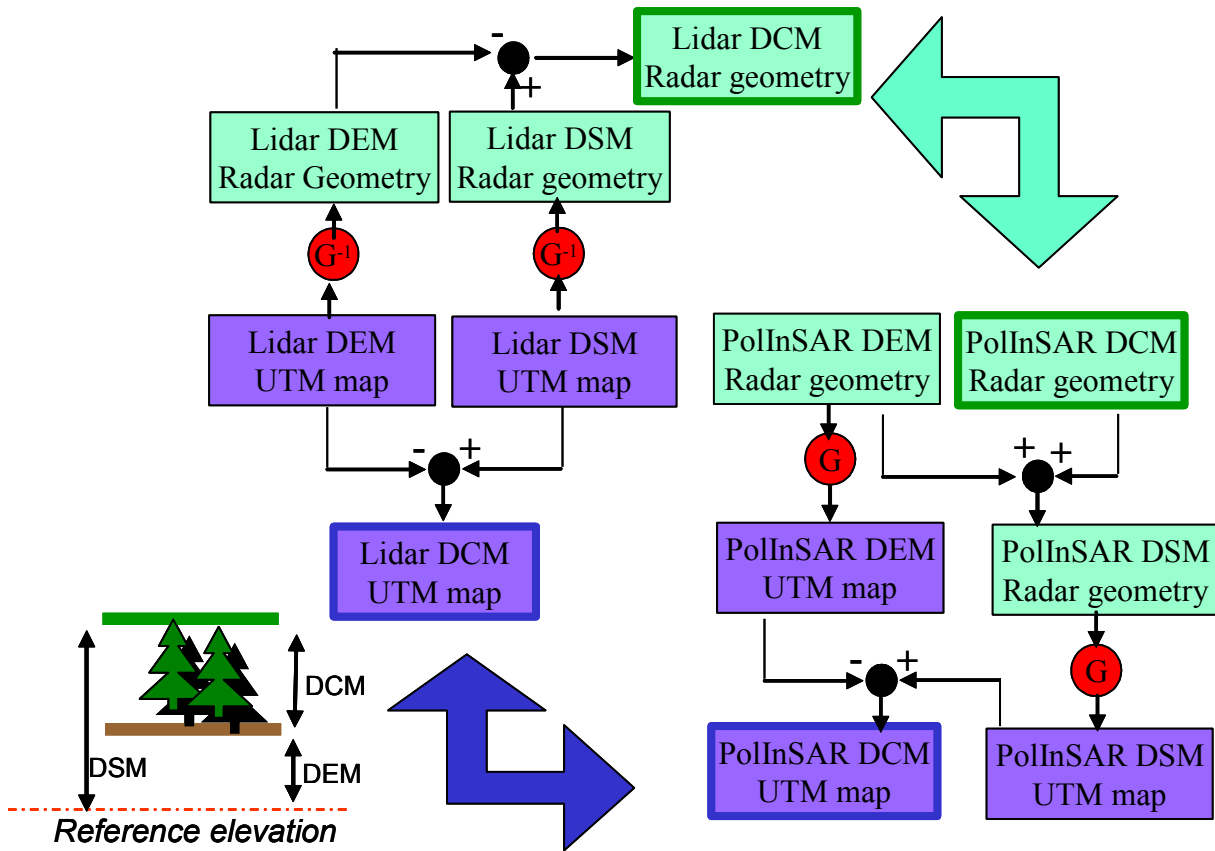


Figure 92 : Dealing with the two geometries. The PolInSAR information is in radar geometry and the LIDAR data is in UTM coordinates. The G transformation is the projection from radar geometry + WGS84 height to UTM geometry based on the grid file provided with the data. G^{-1} is the projection from UTM coordinates + WGS84 height to radar geometry also based on the grid file. DEM is the digital elevation model of the ground with respect to WGS84 height. DSM is the Digital elevation of the top of the tree with respect to the WGS84 height and DCM is the digital vegetation height (DSM-DEM).

As an illustration, one can observe the difference between the LiDAR data in UTM coordinates and in radar geometry in Figure 93.

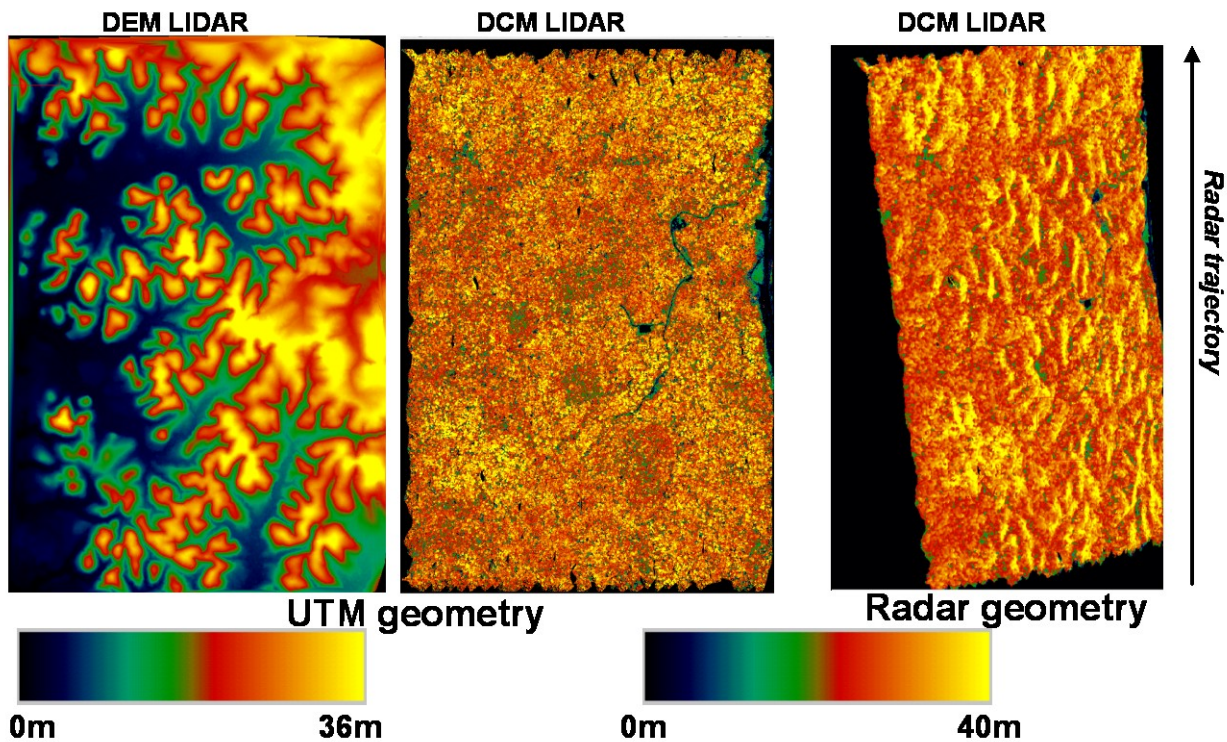


Figure 93 : Illustration of the distortion caused by the radar geometry to the vegetation height information. The left image is the digital elevation model, the middle image the canopy height map in a cartographic projection (UTM). In the right image, the radar perceived vegetation height in radar geometry (corresponding to the schematic of Figure 9) .

The left images, in UTM geometry show the DEM and DCM as provided by the LiDAR data. On the right of Figure 11, the LiDAR DCM in radar geometry clearly displays the strong variation linked to the radar geometry and the underlying topography. The artifacts are high vegetation zones, elongated along the trajectory line and corresponding to slopes facing the radar for which in the same range bin, one can find contribution from the top of trees lying on the higher part of the slope and from the ground at the lower part of the slope.

6.2.2. SINGLE BASELINE POLINSAR INVERSION TECHNIQUE

The PolInSAR height inversion scheme is based on the Random Volume Over Ground model first presented by Cloude and Papathanassiou [Cloude et al., 2003, Papathanassiou et al, 2003]. In a previous study [Dubois-Fernandez et al 2006, Dubois-Fernandez et al, 2008, Garestier et al. 2008.], the PolInSAR inversion at P-band has been addressed. The inversion algorithm based on the RVoG model had to be adjusted to take into account the specificity of P-band. The reasons for that are summarized as follows:

The RVOG model assumes that the contribution coming from the forest can be modeled as the sum of two contributions.

- The first one is the ground contribution attenuated by the crown layer and includes the double bounce return (ground-trunk). The interferometric phase associated with this contribution is simply the one corresponding to the ground height for all possible polarizations. The interferometric coherence is assumed to be 1, after geometric decorrelation correction.
- The second contribution is due to the crown layer only. If the crown layer is modeled as a random volume, it has been showed that the interferometric complex coherence associated with a random volume is independent of the polarization [Treuhaft et al., 1996].

When both contributions are present (they are assumed independent), the resulting interferometric coherence γ_T can be written as:

$$\gamma_T = f(\gamma_g, \gamma_v) = \frac{\sigma_{0g}}{\sigma_{0g} + \sigma_{0v}} \gamma_g + \frac{\sigma_{0v}}{\sigma_{0g} + \sigma_{0v}} \gamma_v$$

Equation 14

where γ_v is the volume-only coherence, γ_g is the ground coherence and σ_{0g} , σ_{0v} are the normalized backscatter coefficient associated respectively to the ground scattering (ground + ground-trunk contribution including the attenuation through the canopy) and to the volume return. Both are varying with polarization and the total coherence is simply the weighted average of the two coherences. As a direct consequence, the weighting factors will vary with polarization, and the locus of the interferometric coherences will describe a line segment between the point γ_g (ground) and γ_v (volume-only).

It can be shown from matrix theory that the locus of interferometric coherence will describe a convex set which will be aligned with the line between the two points. The spread around the line can be caused by the model not being an exact representation of the scattering mechanisms, and by the noises in the data.

In order to solve the problem in a single baseline case, the first studies assumed that the ground coherence is 1 (γ_g) and that the volume coherence (γ_v) is observed for the HV polarization. However at P-Band we have seen that the volume coherence is not observed, as even HV there contains a significant ground contribution.

Alternative approaches have been proposed to solve this problem.

- One assumes a given attenuation in the vegetation layer. This is the one we chose to implement.
- The non-uniqueness can also be solved by using two or more baselines.

THE POLINSAR INVERSION PROCEDURE

The inversion procedure includes several steps:

- For the full image, using a sliding window average, for each pixel, we compute the line based on the Ferro-Famil approach [Ferro-Famil, 2009]
- For each pixel, we have two intersections with the unitary circle. We select the ground coherence as being the one closer to the GammaHH+VV coherence.
- We compute the ground elevation. This ground height map is then smoothed.
- The vegetation height is then computed based on the smoothed version of the ground height.

The same procedure is applied to both the 125MHz and the 6MHz images.

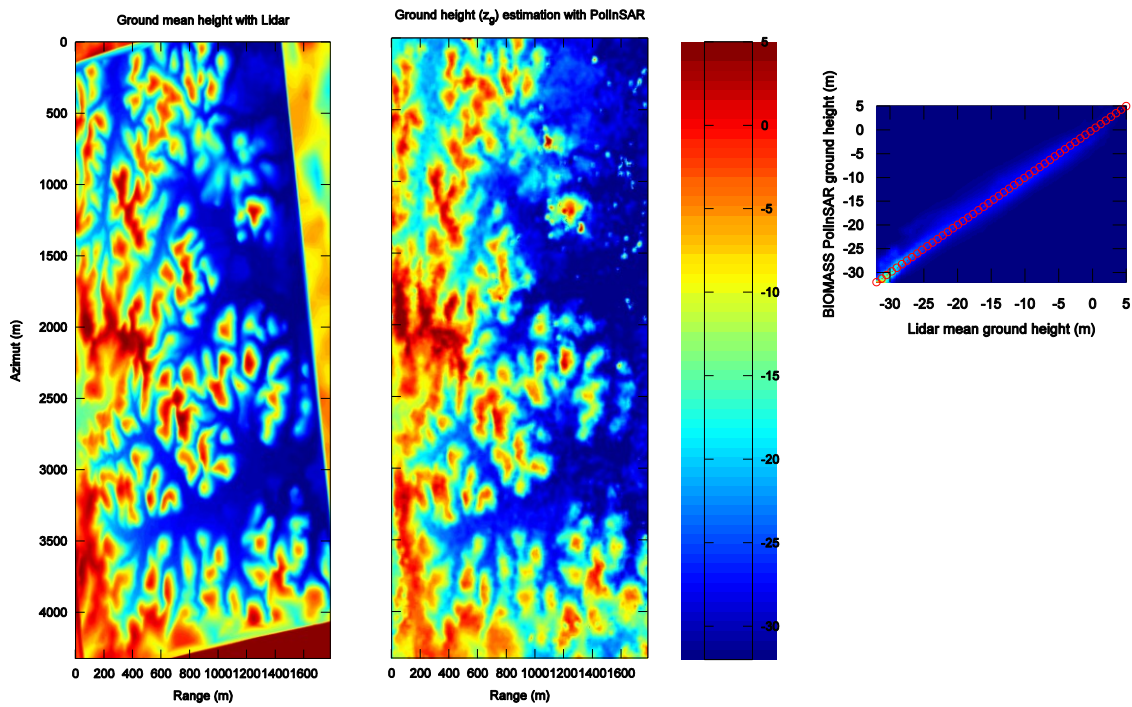
The comparison between the PolInSAR inversion data and the LiDAR data can be made in different geometries as described in Figure 10:

- Digital ground elevation in radar geometry or UTM geometry
- Digital canopy height in radar geometry or UTM geometry

We perform these comparisons both for the full resolution and the 6MHz bandwidth case which is the low resolution case.

6.2.3. GROUND ELEVATION

HIGH RESOLUTION



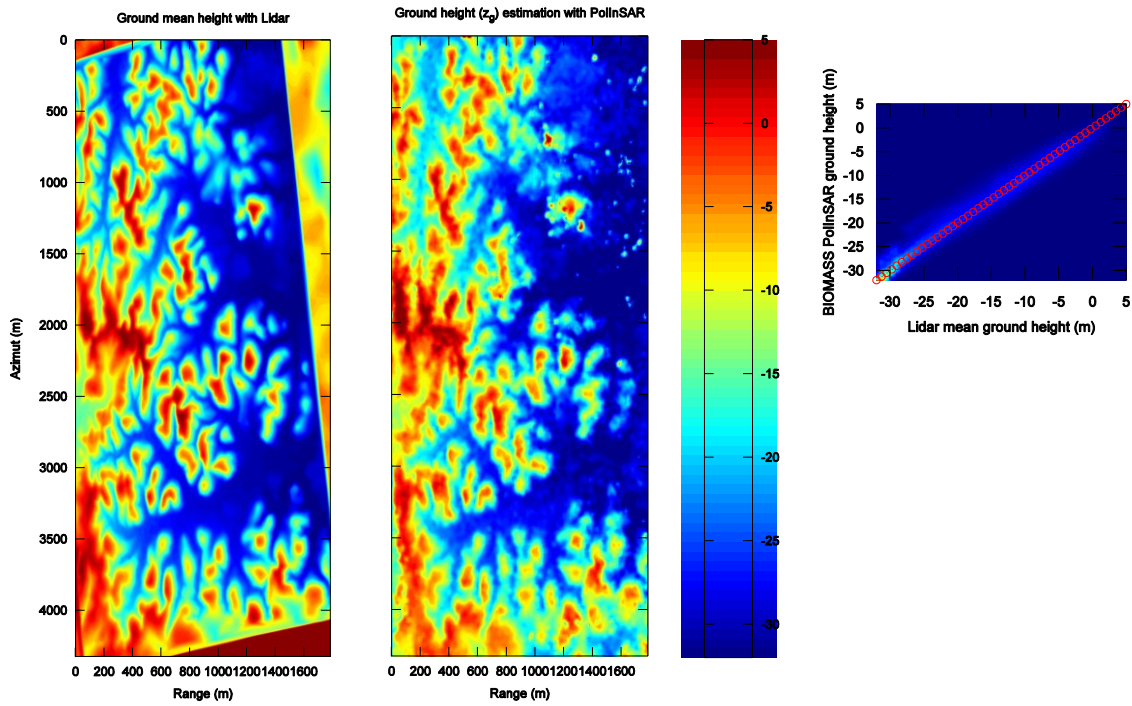
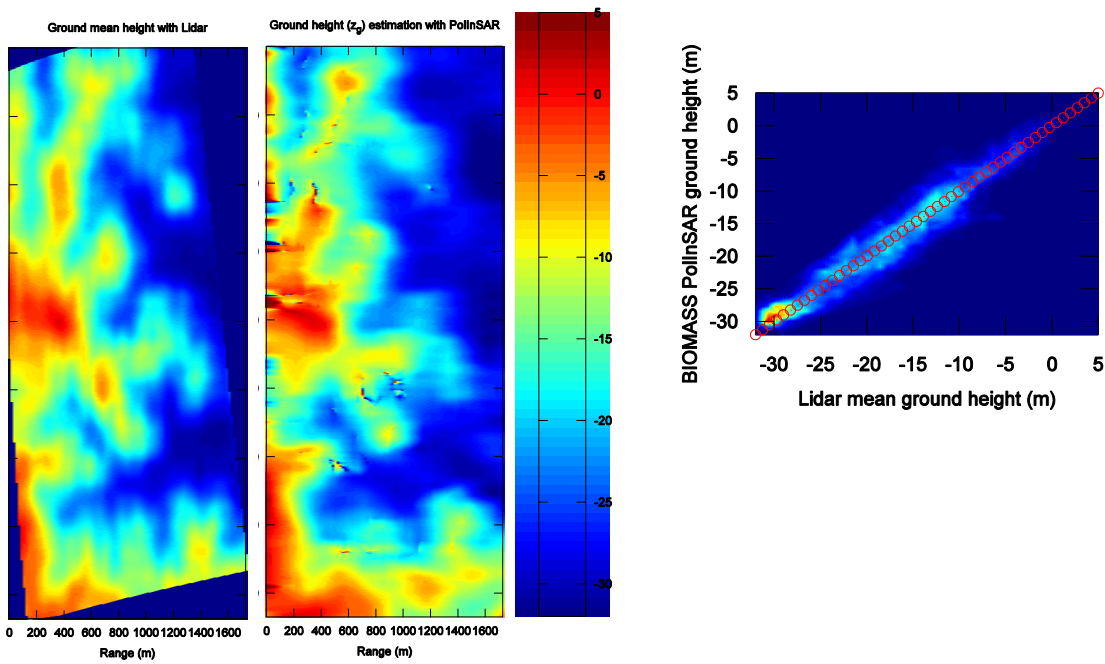


Figure 94: Ground elevation from LiDAR (left image) and PollnSAR high resolution (middle image) in radar geometry. 2D histogram comparing both DEMs on the right.

LOW RESOLUTION



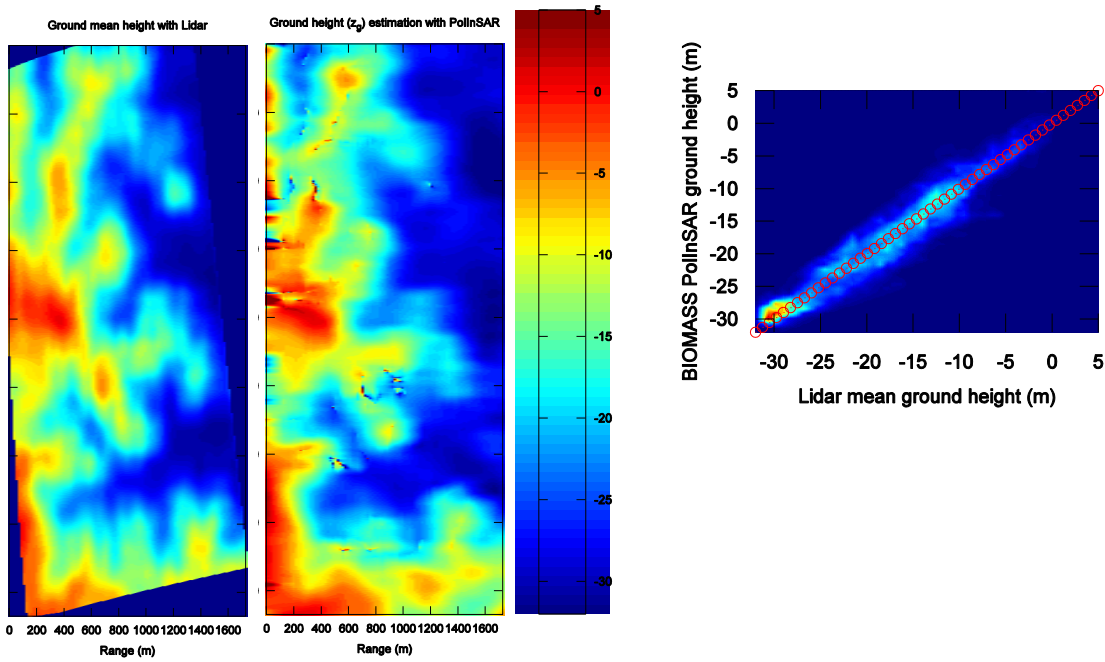


Figure 95 : Ground elevation from LIDAR (left image) and PollnSAR low resolution (middle image) in radar geometry. 2D histogram comparing both DEMs on the right

SUMMARY FOR THE UNDERCANOPY GROUND HEIGHT ESTIMATION

Resolution	Height Bias	Standard deviation
High resolution	0.6m	2.8m
Low resolution	0.0m	3.7m

6.2.4. VEGETATION HEIGHT

HIGH RESOLUTION

In radar geometry

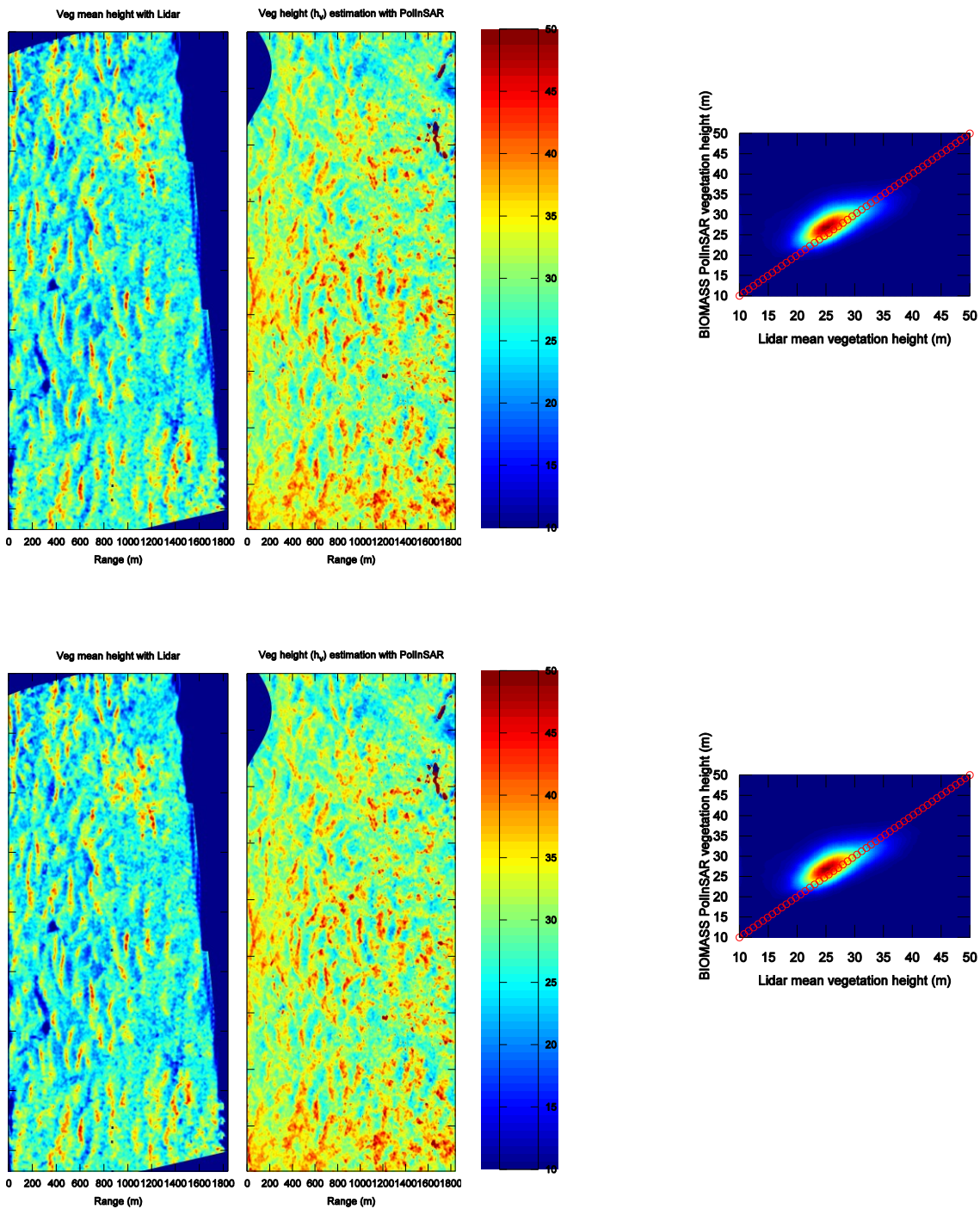
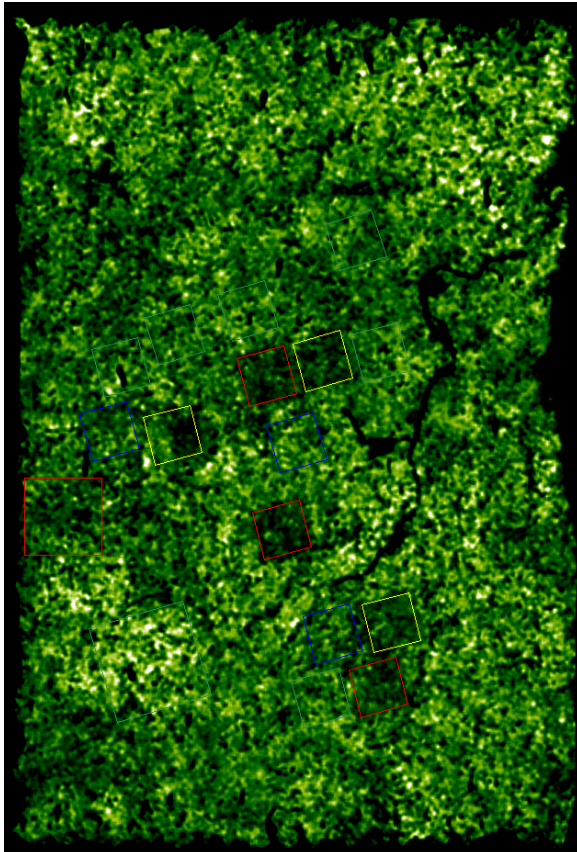


Figure 96 : Radar geometry – vegetation height from LiDAR data (left image) from PollnSAR high resolution data (middle image), 2D histogram(right image)

The topography is the dominating effect in the vegetation height map in radar geometry. The most striking features (ridges) are parallel to the trajectory (left of the images). The two images are plotted with the same color scale (between 10m and 50m). The PollnSAR vegetation height appears higher than the LiDAR vegetation height. Note that the LIDAR data was projected into the radar geometry and the vegetation height corresponding to each pixel is simply the average of all the LIDAR heights falling into this radar pixel. We then apply a sliding window average matching the window used in the PollnSAR inversion.

On the top part of the PolInSAR height, the estimation was not valid as the geometry of the interferometric acquisition was not appropriate.

LIDAR DCM



PolInSAR DCM

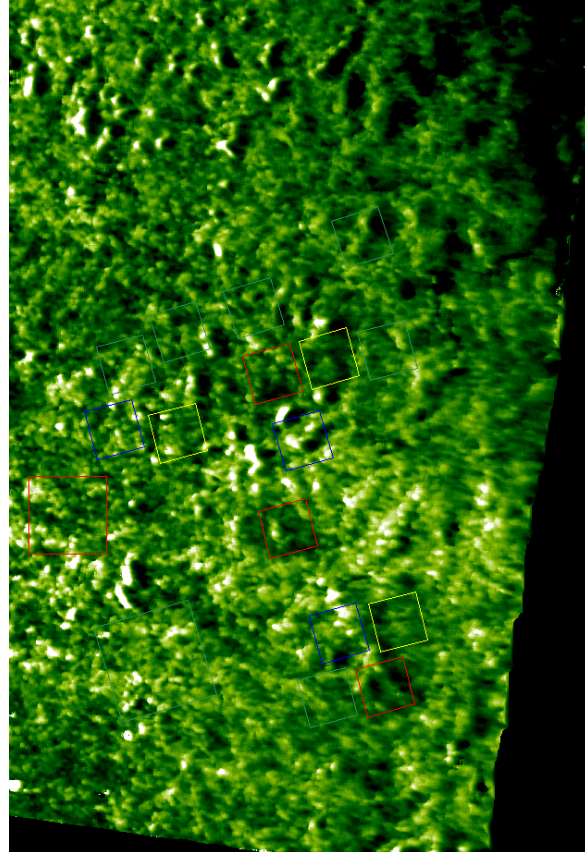
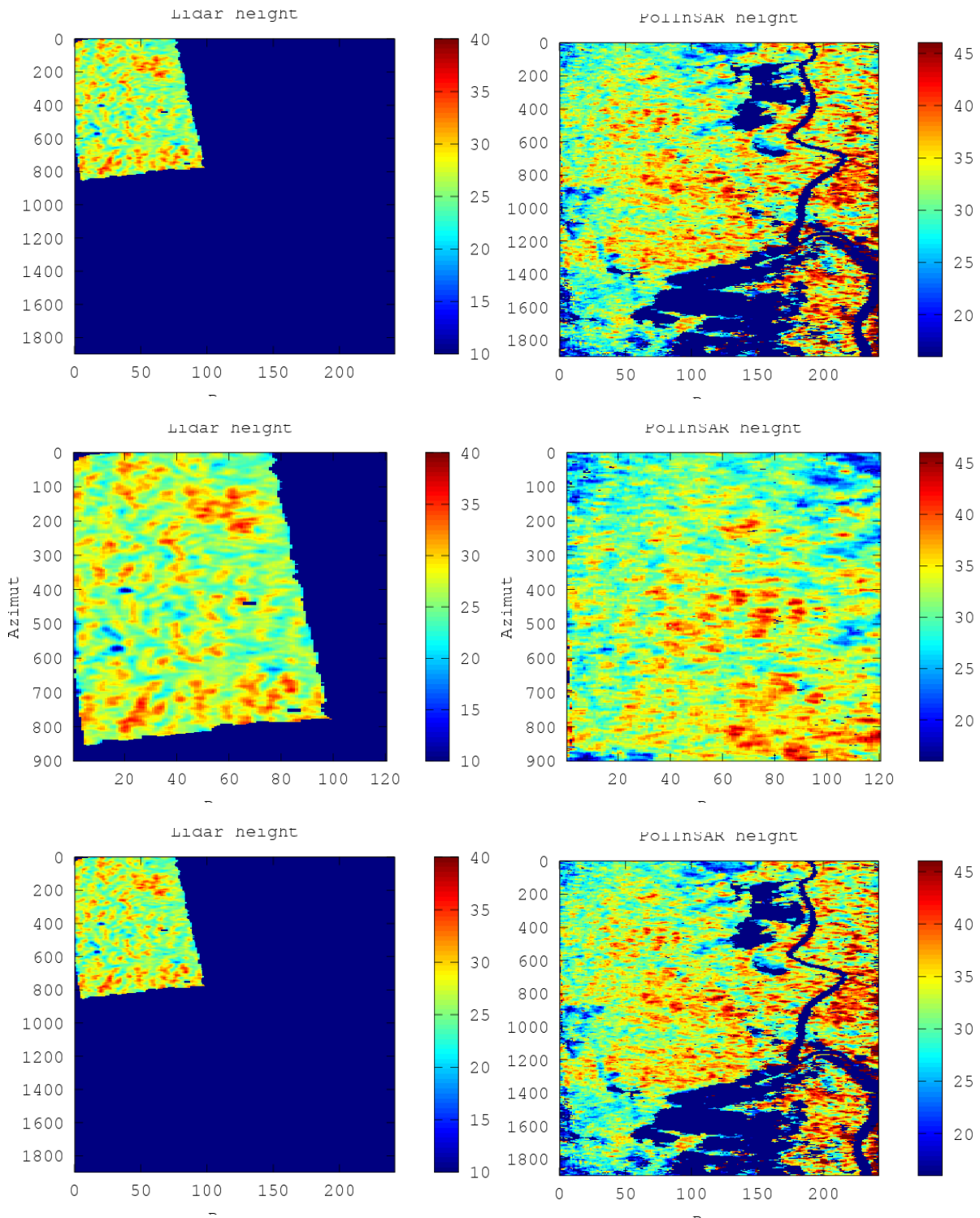


Figure 97 : Comparaison between the LiDAR vegetation height and the high resolution PolInSAR vegetation height with the same color table (20 to 40m) in UTM coordinates. The 16 regions of interest associated with 4 different logging practices can be identified with the green ones being the reference plots and the three treatments coded in blue, yellow and red for respectively small, medium and large logging.

On the above images, it can be observed that in the LiDAR height map, the red regions (corresponding to the most intense logging) have relatively lower trees. This effect can also be observed in the PolInSAR height maps. The PolInSAR height maps show some artifacts associated with the remaining effect of topography (the bright white areas). But overall, the global features are well correlated. On the top part of the PolInSAR height map, the interferometric geometry is not satisfactory and we can observe an underestimation of the height from these regions.

LOW RESOLUTION

In radar geometry



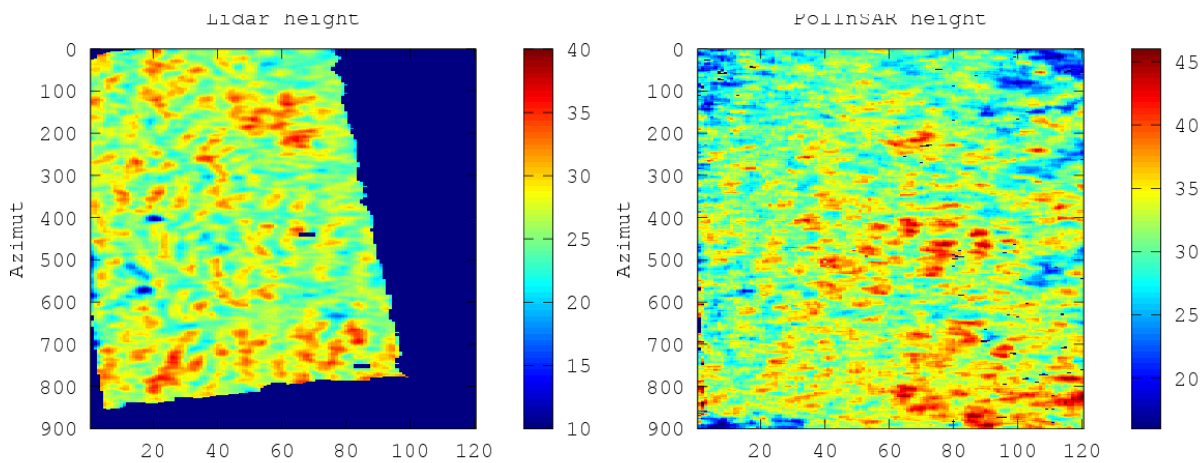
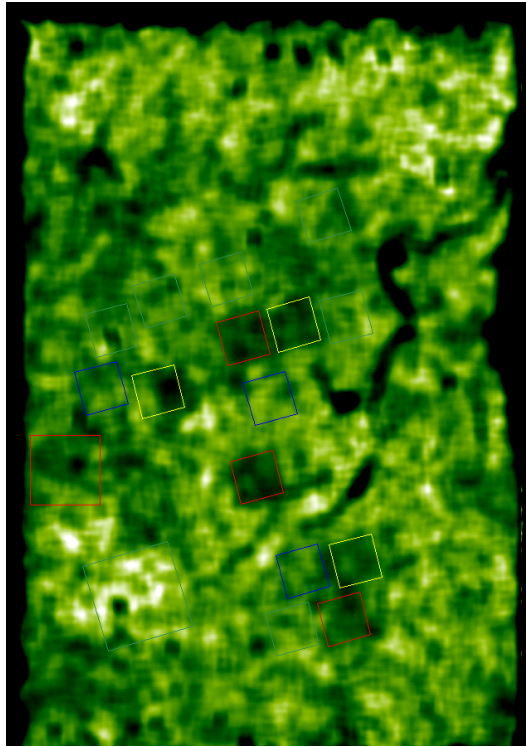


Figure 98 : The top row contains the two height maps corresponding to the full radar image. The LiDAR is only available on a small part of the image as can be seen in the top left image. The bottom row is a zoom of the tops images around the LiDAR area. The first column is the LiDAR derived vegetation height while the right column is the low resolution PolInSAR vegetation height map. These images are in radar geometry.

We chose in the previous images to use a different color scale for the LiDAR and PolInSAR maps as there is a definite bias between the two estimations.

Once again, we note that the topographic effects are dominating the height response in radar geometry.

LIDAR DCM



PolInSAR DCM

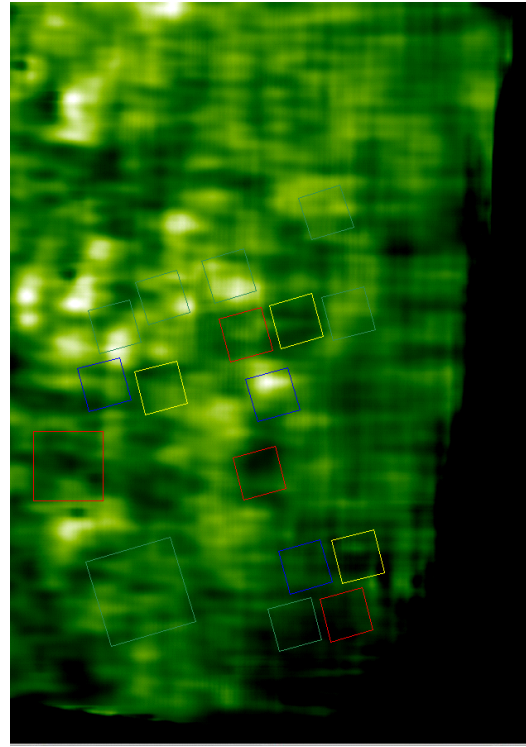
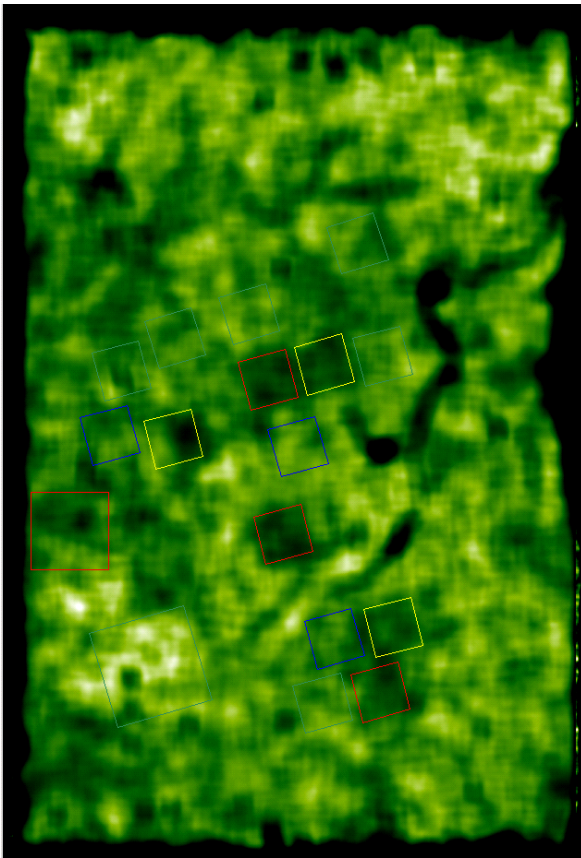


Figure 99 : Comparison between the LiDAR vegetation height and the low resolution PolInSAR vegetation height (tropi0403-tropi0405) with different color tables (20 to 34m for the LiDAR and 28 to 42m for the PolInSAR) in UTM coordinates. The 16 regions of interest associated with 4 different logging practices can be identified with the green ones being the reference plots and the three treatments coded in blue, yellow and red for respectively small, medium and large logging.

LIDAR DCM



PolInSAR DCM

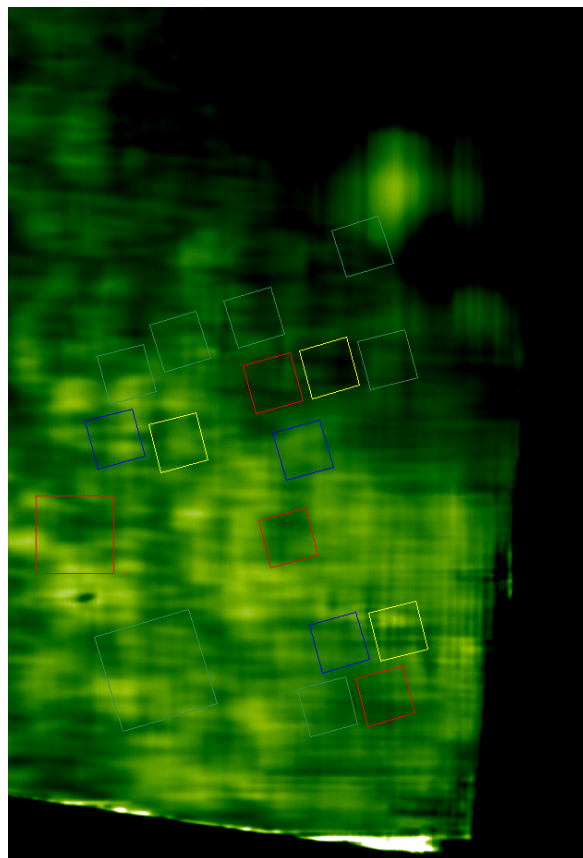


Figure 100 : Comparison between the LiDAR vegetation height and the low resolution PolInSAR vegetation height (tropi0402-trop0404) with different color tables (20 to 34m for the LiDAR and 28 to 42m for the PolInSAR) in UTM coordinates. The 16 regions of interest associated with 4 different logging practices can be identified with the green ones being the reference plots and the three treatments coded in blue, yellow and red for respectively small, medium and large logging.

As observed before, the height map derived from PolInSAR from the 402-404 acquisitions is degraded at the top right corner due to improper interferometric configurations.

In the two PolInSAR height maps derived from the low resolution data, we observed a bias in the height compared to the LiDAR information. This bias was of 1.2m when using the full resolution data and is 6m when using the low resolution data. This increase in bias is linked to the increased natural inhomogeneities in the sliding window of the estimation (same number of pixels but much larger spatial coverage for the low resolution), and associated with the increased spatial decorrelation in the interferometric data (larger relative shift in the bandwidth). At this stage of our analysis, we did not try to correct for any of these effects. We observe however that the overall structure is preserved and that the PolInSAR information is there.

The consistency of the two PolInSAR height maps using 2 independent pairs of images is another proof of the validity of the information and shows that the PolInSAR technique, even at low resolution and in dense tropical forest has a good potential.

SUMMARY FOR THE VEGETATION HEIGHT ESTIMATION

Resolution	Height Bias	Standard deviation
High resolution	2m	4.4m
Low resolution	5.8m	3.7m

6.2.5. CONCLUSIONS

ESA requested that we process the data with a 6 MHz range resolution and a 7.5m azimuth resolution. This corresponds to a 25m x7.5m range x azimuth resolution. The data is processed using a rectangular window which results into a better resolution 0.89*25m in range and 0.89*7.5m in azimuth).

The calibration was a real challenge as the reflectors which were on the ground were not large enough to provide a strong enough signal. An intermediate resolution (using 50MHz) was necessary to access the antenna variation across swath to be applied to the 6MHz data.

The calibration key was set uniquely for the full campaign.

We have processed and calibrates 12 polarimetric datasets (4 complex images + header HH,HV,VH,VV per datasets). We have also included in the delivery the Altitude of ambiguity files, the grid file and the 'ROI' file (Regions of interest).

The radiometric calibration is estimated to be around +/-0.8dB, the Noise-Equivalent sigma to be around -34dB and the cross-talk level to be of the order of -25dB.

The second part of the reports has presented the PolInSAR analysis which was performed on both the high resolution data and the low resolution data. We started by showing how the underlying topography can introduce important artifact in the vegetation height map when in radar geometry and we have described how this effect can be corrected a posteriori.

The PolInSAR analysis provides can provide two types of information: Ground elevation (DEM) and vegetation height or digital canopy model (DCM). The PolInSAR DEM is compared to the LiDAR DEM for the full resolution dataset and the low resolution dataset. In both cases, the PolInSAR DEM is shown to agree well with the LiDAR information, with a 2.7m and 3.8m standard deviation error.

The PolInSAR DCM is compared to the LiDAR DCM is radar geometry and in cartographic geometry. The overall vegetation structure unveiled by the PolInSAR technique is close to the vegetation structure described by the LiDAR data. For the high resolution data, the output of the polInSAR inversion is well correlated to the LiDAR information. For low resolution, the vegetation height information is overestimated by our current PolInSAR inversion algorithm relying on single baseline approach but the information is there as the overall shape is accessible by PolInSAR.

6.2.6. REFERENCES

- [Bonin et al., 2009] Gregory Bonin, Pascale Dubois-Fernandez, Philippe Dreuillet Olivier Ruault du Plessis, Sébastien Angelliaume, Hubert Cantalloube, , Helène Oriot, Colette Coulombeix and the RIM team "the new ONERA multispectral AIRBORNE SAR system in 2009", Radar Con 2010, Pasadena, May 2009.
- [Cloude and Papathanassiou, 2003] Cloude S.R. and Papathanassiou, K.; "A three stage inversion process for polarimetric SAR interferometry", IEE *Proceedings, Radar, Sonar and Navigation*, vol. 150, issue 03, pp. 125-134, June 2003.
- [Dubois-Fernandez et al., 2012] Dubois-Fernandez, P. C.; Le Toan, T.; Daniel, S.; Oriot, H.; Chave, J.; Blanc, L.; Villard, L.; Davidson, M. W. J.; Petit, M. "The TropiSAR Airborne Campaign in French Guiana: Objectives, Description, and Observed Temporal Behavior of the Backscatter Signal," *Geoscience and Remote Sensing, IEEE Transactions on* , vol.50, no.8, pp.3228-3241, doi: 10.1109/TGRS.2011.2180728.
- [Dubois-Fernandez et al., 2011] P Dubois-Fernandez, S Daniel, H Oriot, A Arnaubec, T Le Toan, Y Lasne, L Villard, J Chave, M Rejou-Mechain, L Blanc, M Petit, "Final report on the technical assistance for the deployment of airborne SAR and geophysical measurements during the TropiSAR 2009 experiment", ONERA-RF 1/17551 DEMR, March 2011.
- [Dubois-Fernandez et al., 2006] Dubois-Fernandez Pascale, Franck Garestier, Isabelle ChampionXavier Dupuis, Philippe Paillou," Forest parameter retrieval from PolInSAR data at L and P band", PolInSAR2006, Frascati January 2006.
- [Dubois-Fernandez et al., 2008] Dubois-Fernandez, P., J.-C. Souyris, and S. Angelliaume F. Garestier. The compact polarimetry alternative for spaceborne SAR at low frequency. *Geosciences and Remote Sensing, IEEE Transactions on*, 46(10):3208–3222, Oct. 2008.
- [Ferro-Famil et al., 2009] Ferro-Famil L., M. Neumann, Y Huang, "Multi-baseline PolInSAR statistical techniques for the characterisation of distributed media" in Proc. IGARSS09 , Cape Town, South Africa, pages 971-974, 2009.
- [Garestier et al., 2008] Garestier, P.C. Dubois-Fernandez & I. Champion, "Forest Height Inversion Using High Resolution P-Band Pol-InSAR Data", *IEEE Transactions on Geoscience and Remote Sensing*, vol 46, No. 11, November 2008.
- [Le Toan et al., 2010] Le Toan T., S. Quegan, M. Davidson, H. Balzter, P. Paillou , K. Papathanassiou, S. Plummer, S. Saatchi, H. Shugart, L. Ulander : 'The BIOMASS Mission : Mapping global forest biomass to better understand the terrestrial carbon cycle', in press, *Remote Sensing of Environment*, October 2010.
- [Papathanassiou and Cloude, 2003] Papathanassiou K.P., and S.R. Cloude, "The Effect of Temporal Decorrelation on the Inversion of Forest Parameters from Pol-InSAR Data", *Proceedings IGARSS'03 (CD-ROM)*, Toulouse, France, 2003.
- [Quegan, 1994] Quegan, S.; "A unified algorithm for phase and cross-talk calibration of polarimetric data – Theory and observations," *IEEE Trans. Geosci. Remote Sensing*, Vol. 32, pp 89-99, 1994.
- [Treuhaft, et al., 1996] Treuhaft, R.N., S.N. Madsen, M. Moghaddam, and J.J. van Zyl, "Vegetation Characteristics and Underlying Topography from Interferometric Data", *Radio Science*, vol. 31, pp. 1449-1495, 1996.

6.3.WP 43: PERFORMANCE ANALYSIS POLINSAR AND BACKSCATTERING COEFFICIENT

This section addresses the performance of the Pol-InSAR and intensity based forest height and biomass inversion for a tropical forest. The performance is assessed based on the algorithms developed for intensity based retrieval, Pol-InSAR retrieval and the retrieval combining both intensity and Pol-InSAR. The assessment using TropiSAR P-band SAR data, processed at 6 MHz bandwidth, together with the set of in-situ data at Paracou forest site.

Specifically, in this WP, CESBIO contribution based on the 6MHz TropiSAR data will aim at the following points:

- 1) Define metrics that allow to quantify the performance of the PolInSAR and intensity based forest height and biomass inversion.
- 2) Compare the retrieved biomass and forest height information against in-situ data collected during the TropiSAR campaign and derive quantitative statistics using the defined metrics.
- 3) Quantify the performance relative to topography and to changing environmental conditions.
- 4) Assess the use of multi-temporal filters on the performance of intensity based inversion schemes.

6.3.1. METRICS TO QUANTIFY THE PERFORMANCE OF POLINSAR AND INTENSITY BASED FOREST HEIGHT AND BIOMASS INVERSION

The following metrics are defined for computing the regression parameters and for comparison of the retrieved biomass with reference in situ data.

REGRESSIONS PARAMETERS :

Using log relationships between the above ground biomass AGB and SAR measurements (backscatter intensity and Pol-InSAR height), the regression parameters are deduced from the SAR and in situ data estimated over the reference forest plots. The regression parameters are based on the following minimization:

$$\min_{\beta_0, \beta_1} \left\{ \sum_{i=1}^n (Y_i - \beta_0 - \beta_1 X_i)^2 \right\}$$

with n as the number of observations Y_i (e.g. backscatter or Pol-InSAR height) corresponding to the values X_i (e.g. AGB). The minimum is obtained for $\beta_0 = a_0$ and $\beta_1 = a_1$ with :

$$a_1 = \frac{\sum_{i=1}^n (X_i - \bar{X}) \cdot (Y_i - \bar{Y})}{\sum_{i=1}^n (X_i - \bar{X})^2}$$

$$a_0 = \bar{Y} - a_1 \bar{X}$$

The linear correlation coefficient noted ρ is defined by the ratio between the covariance over the product of X and Y standard deviations :

$$\rho = \frac{\sigma_{XY}}{\sigma_X \sigma_Y}$$

with : $\sigma_{XY} = \sum_{i=1}^n (X_i - \bar{X}) \cdot (Y_i - \bar{Y})$ (covariance)

and : $\sigma_X = \sqrt{\frac{1}{N} \sum_{i=1}^n (X_i - \bar{X})^2}$ (standard deviation)

Under several assumptions on the observations Y_i , the following formulae can be used for the standard deviations of a_0 , a_1 :

$$\sigma^2(a_1) = \frac{MSE}{\sum_{i=1}^n (X_i - \bar{X})^2}$$

$$\sigma^2(a_0) = \frac{MSE \cdot \sum_{i=1}^n X_i^2}{n \cdot \sum_{i=1}^n (X_i - \bar{X})^2}$$

In addition, it can be also demonstrated that the quantities $\frac{\sigma(a_0)}{a_0}$ and $\frac{\sigma(a_1)}{a_1}$ follow a Student distribution, hence the following confidence intervals for the level $(1-\alpha)$:

$$IC_{1-\alpha}(\beta_{0,1}) = [a_{0,1} - t_{1-\alpha/2} \sigma(a_{0,1}); a_{0,1} + t_{1-\alpha/2} \sigma(a_{0,1})]$$

RETRIEVAL PERFORMANCE ASSESSMENT :

The retrieval performance is assessed by the following metrics relating the retrieved biomass to the in situ biomass as follows:

$$RMSE = \sqrt{\frac{1}{N} \sum_k (\hat{B}_k - \check{B}_k)^2}$$
 (Root Mean Squared Error)

$$MPE() = \frac{1}{N} \sum_k \frac{\hat{B}_k - \check{B}_k}{\check{B}_k}$$
 (Mean Percent Error)

with \hat{B}_k and \check{B}_k as for estimated and in-situ AGB values on a sample k, among the N forest plots.

6.3.2. RETRIEVAL ALGORITHM AND PERFORMANCE

The performance of the retrieval algorithms is assessed using P-band SAR data processed at 6 MHz bandwidth and at repeat cycle close to the conditions defined for the Biomass mission (e.g. 3 acquisitions every 6 months, cf. [Biomass,2012]).

RETRIEVAL ALGORITHMS :

INTENSITY-BASED RETRIEVAL ALGORITHM

Above Ground Biomass (AGB) estimation in tropical forest builds on earlier methods (e.g. [Hoekman, 2000; Saatchi, 2007] that exploited multiple polarisations and topographic correction to derive biomass in tropical forests with biomass less than 300 t/ha and with moderate topography. The TropiSAR campaign in French Guiana, was designed to provide multi-temporal datasets that would support the extension of these methods to higher biomass and steeper slopes, as is often encountered in tropical forests [Dubois-Fernandez et al, 2012]. A key finding from TropiSAR illustrates that different issues need to be addressed in tropical as compared to boreal forests, and provided basic insights underpinning the construction of the retrieval algorithms. Tropical rain forests are characterized by high biomass density (up to 500 t/ha or greater), and structured in different layers. However, little serious effort has been made in the past to recover values above 250-300 t/ha, because the sensitivity of backscatter to biomass in this range is easily masked by perturbing effects, particularly those related to topography. Recovering the biomass signal therefore needs careful correction for these effects. This has two aspects: (1) correctly accounting for the volume contained in the SAR resolution cell; (2) accounting for the varying contributions of the dominant scattering mechanisms, i.e., volume scattering and branch-ground double bounce scattering, arising from changes in local incidence angle [Villard et al, 2010].

ALGORITHM FOR FORESTS OVER TERRAIN WITH MODERATE TOPOGRAPHY:

For tropical forests with moderate topography (typically with slope less than 4°), the inversion is based on the use the normalised HV backscattering coefficient -- commonly referred to as γ_{hv}^0 -- as in the general case where volume scattering is dominant at HV. The HV backscatter has the highest dynamic range amongst all the linear polarisations (e.g., the contrast between grasslands and high biomass forests observed in TropiSAR data is 14 dB, 18 dB and 9 dB for HH, HV and VV respectively), and is best suited to biomass inversion (cf. [Le Toan et al, 2012]). Biomass is then derived from the normalised backscattering coefficient γ_{hv}^0 by the following equation:

$$\gamma_{hv}^0 [dB] = a_1 \bullet \log_{10}(AGB[t / ha]) + a_0$$

where B is biomass in t/ha and γ_{hv}^0 is given in dB. The parameters a_1 and a_0 can be derived using ground data. However, the value for a_1 is already available because the sensitivity of backscatter to biomass is stable, though local conditions may lead to some slight modification (cf. section 6.3.5). The absolute level term, a_0 (which accounts for variations in sensor, processing, site characteristics and temporal variation), can be estimated using a limited amount of ground data.

Concerning the log relationship, this model can be also formulated as a power law when intensity is expressed in natural values:

$$(\gamma_{hv}^0 [natural] - a_0) = (AGB[t / ha])^{a_1}$$

ALGORITHM FOR HIGH BIOMASS (E.G. $\geq 200 \text{ THA}^{-1}$) OVER HILLY TERRAIN AT STEEP RADAR ELEVATION ANGLE:

Statistical analysis of the relationship between the backscattering coefficient and biomass, together with information on the scattering mechanisms derived from tomography [Ho Tong M.D. 2012] and electromagnetic modelling using the MIPERS model [Villard L. 2010]), showed that at P-band double bounce scattering can be significant. This was particularly the case for higher biomass forests (exceeding 200 t/ha) in hilly terrain, as is typical of many of the world's tropical forests. Here topography acts to enhance a double

bounce contribution coming mainly from branches in the forest canopy. Such conditions apply to most of the forest plots studied in French Guiana; these have biomass ranging from 250 to 450 t/ha, and 70 out of the 90 plots of ≥ 1 ha are on mean slopes exceeding 4° .

Surface slopes not only affect the relative importance of the scattering mechanisms and a resulting specific angular behavior but also cause polarisation orientation changes, which can be established from non-reflection symmetric terms in the coherency matrix -- cf. methods developed by [Lee J.S 2000, Lee J.S 2011] based on the Polarization Orientation Angle (POA) compensation.

To improve the relationship between backscatter and AGB in the case of tropical dense hilly forests, the t^0 backscatter coefficient is introduced following the underlying ideas (cf. [Villard et al, 2013]):

- t^0 is based on backscatter terms which fulfill as far as possible the reflection symmetry property; which is supposed to hold for all the scattering contributions in which the ground is not involved.
- t^0 includes normalization of backscatter angular variations, adapted to cases for which the double bounce scattering contribution is significant with respect to the volume contribution.

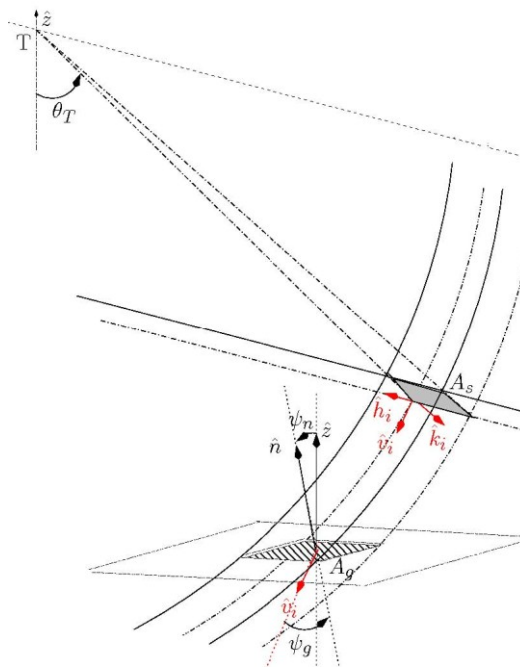


Figure 101 : Slant range radar geometry showing from transmitter T, the radar incidence angle θ_T , the slant and ground surfaces A_s and A_g , the transmitting polarization basis, the vertical and normal unitary vectors \hat{z} and \hat{n} , the slope angles ψ_n and ψ_g as well as the intercepted volume by a given range resolution cell.

The new indicator t^0 is defined by:

$$t^0 = \left\langle \frac{t_{33}^g}{2N^0} \right\rangle$$

where the brackets hold for the spatial and/or temporal multilook, t_{33}^g as the coefficient of the corrected coherency matrix (post rotation from polarization angle g) and N^0 as the angular normalization function, defined by:

$$\mathcal{N}^0 = \cos \psi_n^{rg} \cdot \frac{A_s}{\cos \psi_g} \cdot \cos \theta_i \cdot \cos^n \theta_i$$

with the angle ψ_n^{rg} derived as slope angle ψ_n (cf. Figure 101) but considering – instead of \hat{n} – its projection into the plane of incidence. It can be reminded that the angular normalization function accounts for changes in effective scattering volume related to the local geometry and to changes related to the specific angular variation of the backscatter in the case of a mix contribution from volume and double bounce scattering contributions (cf. [Villard et al., 2013]).

The AGB estimate from t^0 is based on a log relationship, as for γ_{hv}^0 , though with different coefficients a_1 and a_0 .

Since t^0 has been only validated on the test plots, that is in the case of dense and hilly forests from non grazing radar incidence angle (30-45°), both intensity based indicators γ_{hv}^0 and t^0 of biomass will be combined through the following linear weighting:

$$B = \alpha B(\gamma_{hv}^0) + (1 - \alpha) B(t^0)$$

where $B(t^0)$ and $B(\gamma_{hv}^0)$ are the biomass values derived from t^0 and γ_{hv}^0 , and the weight 'α' is defined by

$$\alpha = 1 - \frac{B(\gamma_{hv}^0)}{B_{max}}$$

Here B_{max} is the maximum value of $B(\gamma_{hv}^0)$ occurring in the scene.

ANALYSIS OF BACKSCATTERING COEFFICIENTS (γ_{hv}^0 , T^0) VERSUS BIOMASS

The 16 forest plots (15 plots of 250m x 250m and 1 plot of 500m x 500m) in Paracou have been used to analyse the relationship between AGB and the backscattering coefficients estimated from the TropiSAR data. Because of the coarse resolution of the 6MHz SAR data, the subplots – derived from 2*2 subdivisions of the original plots (i.e 125m x125m and 100m x100m) -- used in the analysis of the full resolution TropiSAR data, could not be used because of the low number of spatial looks.

In line with the Biomass scenario regarding revisit time and deliverables (2 estimates per year), sequences of 3 dates will be used to increase the number of looks for the estimation of backscatter intensity. Together with these 3 temporal looks, a 5*3 sliding window has been employed, along azimuth and range directions (it can be reminded that fully polarimetric P-band SAR data were acquired on August 10, 12, 14, 17, 24, 30th and September 1st 2009, with the aircraft keeping the same heading).

Based on this number of looks, images of γ_{hv}^0 and t^0 have been derived from the SLC data. Mean estimates have then been obtained using all pixels belonging to each in-situ plots. Concerning the relationship between γ_{hv}^0 and AGB, the correlation resulting from the fit to the power law model turns out to be not significant (cf. Figure 102): ρ ranges from 0.25 to 0.35 for the various combinations of dates, whereas the critical Pearson coefficient value at 5% risk is 0.5. As mentioned before, the sensitivity of backscatter to AGB is small for biomass above 300 t/ha so that perturbations brought by topographic effects are likely to hinder the γ_{hv}^0 -- AGB relationship.

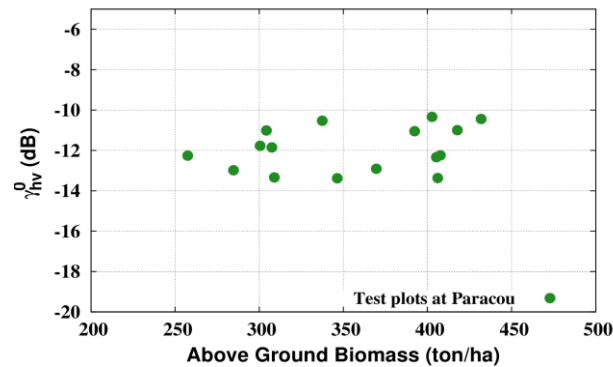


Figure 102 : backscattering coefficient γ_{hv}^0 versus in-situ AGB for the 16 plots at Paracou test site, showing a non significant correlation (ρ is about 0.3).

Using the ad-hoc AGB indicator t^0 , the relationship was found to increase significantly (ρ ranges from 0.64 to 0.88) as shown in Table 6 and Figure 103. In addition, it can be stressed that the sensitivity to AGB (slope a_1) is in the same order of magnitude than with full resolution data (i.e. 6.5 ± 0.98 for t^0). Among the 7 TropiSAR acquisitions, the August 14 data have been disregarded because of strong perturbations due to the wind in airborne flight data (which is consistent with the low coherence of all couples involving this data). These perturbations are however not critical since in this worst case, where t^0 is only based on the August 14 data, the correlation coefficient with AGB is just above the critical Pearson value (0.5).

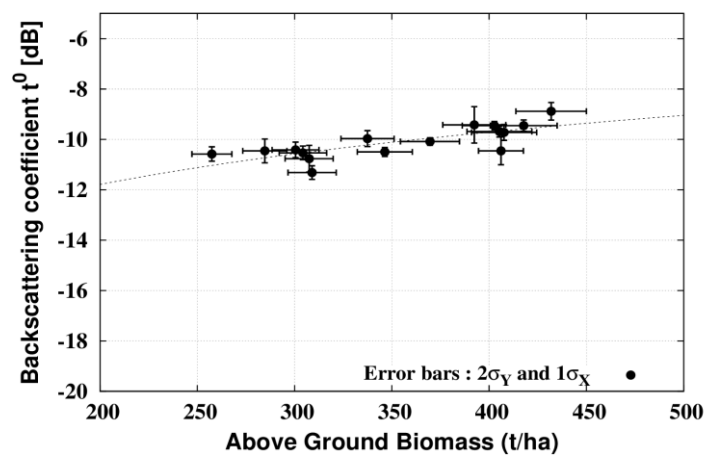


Figure 103 : backscattering coefficient t^0 versus AGB for the 16 reference plots. Vertical error bars (2σ level) are the standard deviation computed from the 4 sequences of 3 different dates. Horizontal error bars (1σ level) result from the uncertainties in in-situ AGB estimates (detailed in the text body). Levels of confidence (1 or 2σ) displayed above have been chosen for the sake of graph clarity.

Dates\RP	ρ	χ^2	a_1	IC(a_1)	a_0	IC(a_0)
0-1-3	0.64	3.68	5.88	2.54	-22.03	6.46
1-3-4	0.66	4.00	6.50	2.65	-23.62	6.74
3-4-5	0.81	2.10	7.32	1.92	-25.81	4.88
4-5-6	0.88	1.33	7.89	1.52	-27.17	3.88
$\langle t^0 \rangle$	0.77	2.45	6.90	2.01	-27.66	5.27

Table 6 : regression parameters (RP) associated to the log relationship between t^0 -AGB for the 4 sequence of 3 dates. Last line is for regression parameters of the mean value $\langle t^0 \rangle$ derived from the 4 sequences mentioned above. χ^2 is for the 'chi2' value to quantify the data dispersion, the other statistical parameters have been described in 6.3.1.

The method used to estimate in-situ AGB uncertainties have been described in [TropiSAR, 2011]. It can be reminded that the mean AGB for these degraded and undisturbed forest plots range from 260 to 430 t/ha. Depending on allometric and spatial errors, the associated uncertainties (at 2-sigma level) range from 7.9 and 8.4 % for 6.25 ha plots and 5.7 for the 25 ha plot (cf. 6.1.3 in [Dubois et al., 2012]). Allometric errors comes from uncertainties linked to models used to derive AGB from diameter and wood density, whereas spatial errors comes from the representativeness of the plot. The latter can be expressed as a decreasing function of the plot area (A) so that for the 25 ha plot, both errors are comparable whereas for 1.5625 ha plots (125 m*125 m) the allometric contribution can be neglected and the total 2-sigma error is between 15.3 and 15.6%.

POL-INSAR-BASED RETRIEVAL ALGORITHM

In order to test the relationship between the forest height and above ground biomass over the 16 forest plots, Lidar height has been used. Figure 104 shows the relationship between H_{50} (median resulting from all pixels belonging to the plot) and AGB, the correlation is $\rho=0.91$ ($\rho=0.89$ with the mean height). However, it can be noted that the correlation can be even higher for biomass less than 400 t/ha. Beyond this value, the fit is not clear and the relationship could be degraded, possibly because of the effect of emerging trees, expected to contribute more in the mean biomass of the plot than in the median/mean forest height.

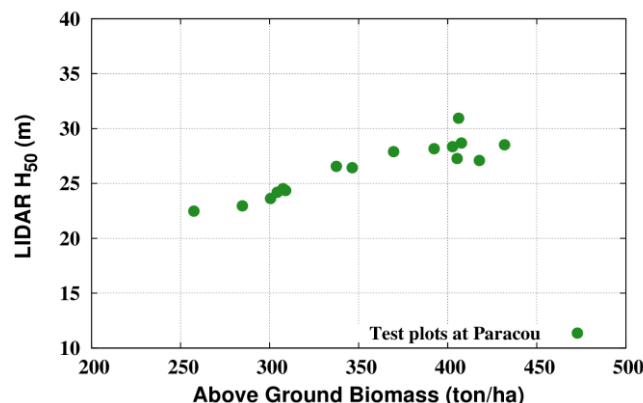


Figure 104 : Lidar height H_{50} (i.e median) as a function of forest AGB at 16 reference forest plots. Using the log relationship, the Pearson correlation is 0.91, slightly better than the correlation between the mean Lidar height and AGB (0.89).

Comparison between Pol-InsAR and Lidar heights have then be performed, using acquisitions 0403-0405 from the TropiSAR data at 6MHz, afore-detailed in WP42. The comparison (Figure 105) shows a bias of about 5m (RMSE~28%), and a correlation of 0.41 which is not significant. However, for a number of plots,

there is an issue of ambiguity height. For example, if plots 9 to 12 and 16 are discarded because of ambiguity height issues, the correlation reaches 0.81.

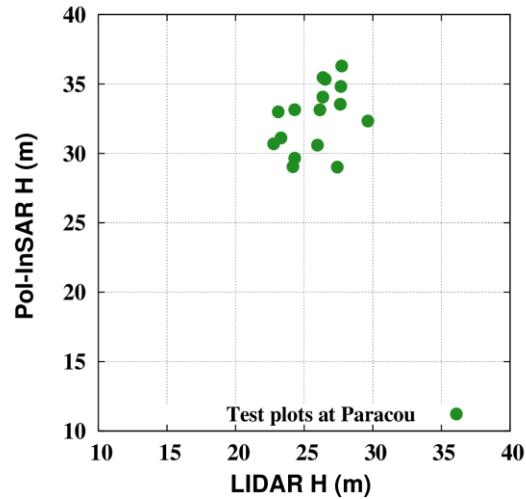


Figure 105 : Pol-InSAR versus LIDAR height. For both, the mean height value resulting from the pixels belonging to a given plot.

Concerning the relationship between Pol-InSAR height and AGB showed in Figure 106, a correlation of 0.5 (just significant) using the 16 plots at Paracou has been found based on the log relationship. As seen for Pol-InSAR against LIDAR height, regression results are much better without plots 9 to 12 and 16.

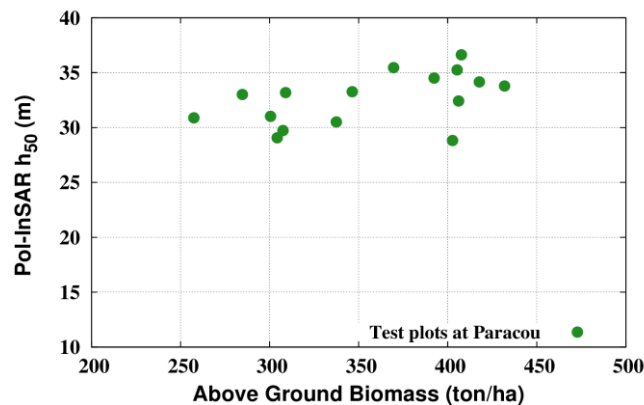


Figure 106 : Pol-InSAR height H50 versus AGB for the 16 plots at Paracou.

THE COMBINED RETRIEVAL ALGORITHM USING A BAYESIAN APPROACH :

The SAR measurements that are related to AGB are the intensity based coefficients γ_{hv}^0 and t^0 as well as the Pol-InSAR height. For each type of indicators (I^0 or H), a log relationship with biomass can be used, i.e:

$$I^0[dB]/H[m] = a_1 \log_{10}(AGB[t/ha]) + a_0$$

PIXEL TO PIXEL INVERSION

A Bayesian approach is proposed to handle the various noise sources that can affect the SAR measurements to be inverted to AGB. The required prior information is estimated using the available test plots for which the discrepancy between the observed measurements and their theoretical value (according to the direct model) can be assessed. The prior conditional probability density function (pdf) is built assuming a Gaussian distribution characterized by its empirical mean and standard deviation. Considering multiplicative noise sources, their impact can be modelled as follows:

$$D_{meas} = R \cdot D_{th}$$

linking the measured and the expected theoretical data. The expected data are derived from the theoretical model providing the link with the biomass B:

$$D_{th} = f(B)$$

Since the conditional mean (noted $E[B/D]$) minimizes the mean squared error (MME), this variable has been retained for our biomass estimator (noted B_{MMSE}) and can be written like:

$$B_{MMSE} = \int_B B \cdot P(B / D) \cdot dB$$

Using the Bayes theorem with the Jacobian transformation associated to the variable change above-mentioned (with R), it can be demonstrated that:

$$P(B / D_{meas}) = P(D_{meas} / B) \cdot P(B) / P(D_{meas}) \propto P(R) / P(D_{th})$$

since $P(B) / P(D_{meas})$ is a constant factor assuming a uniform biomass prior distribution.

Considering the estimation of the prior pdf P(R) from the test plots, the integral for the biomass estimator B_{MMSE} can then be performed.

This Bayesian formulation enables to combined various indicators, as long as a these indicators can be described as functions of AGB, such as intensity and Pol-InSAR height.

RETRIEVAL PERFORMANCE :

Retrieval performances can be quantified from the 16 in-situ plots, as shown in Figure 107 and Figure 108 with intensity, Pol-InSAR based methods and their combined use.

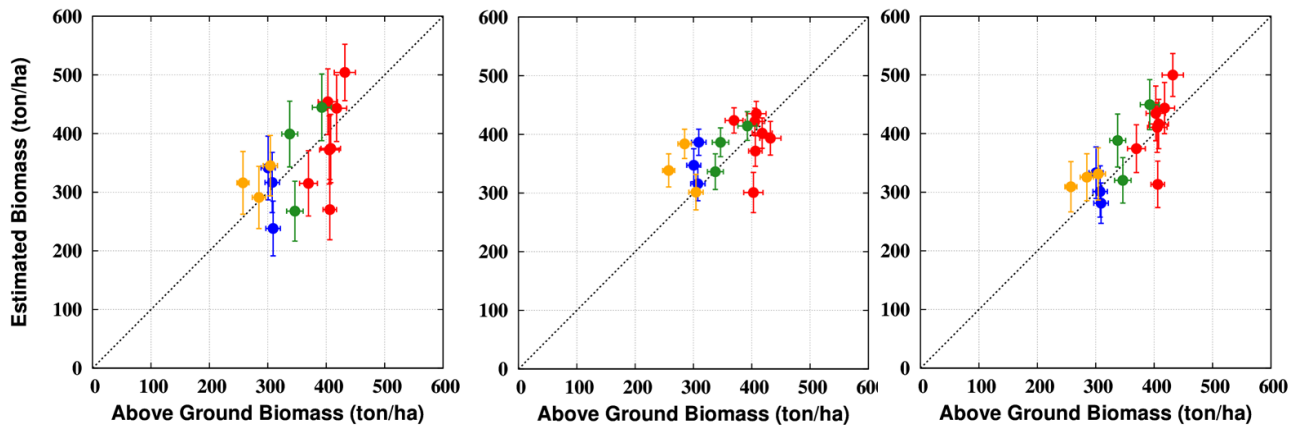


Figure 107 : from left to right are the scatterplots of retrieved AGB versus in-situ AGB from intensity and Pol-InSAR based methods, followed by their combination. For each retrieval, a-priori coefficients a_1 and a_0 have been chosen (e.g 6.5 and -28 respectively for t^0) and the mean values from the various sequences (cf. table 1) over the 16 test plots are used for training.

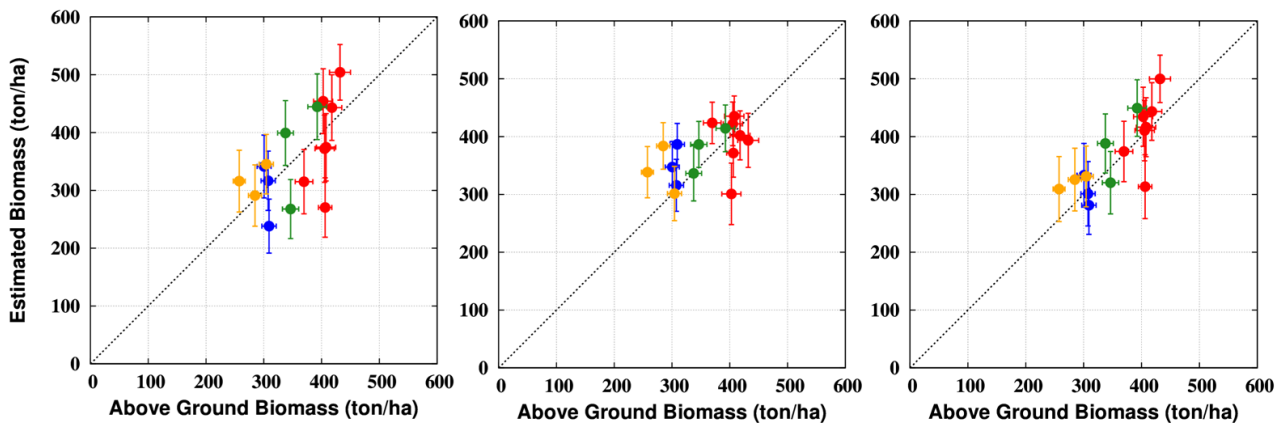


Figure 108 : as figure 7 but with uncertainties for AGB estimated from Pol-InSAR (middle scatterplot) using standard deviation of 4m i.o 2m. This change is also accounted for in the right scatterplot based on the combined estimates.

Error bars displayed in Figure 107 and Figure 108 for both retrieved and in-situ AGB correspond to the 1σ level. Uncertainties related to in-situ AGB estimates have been previously described, whereas uncertainties for the retrieved AGB result from the Bayesian formulation and have been derived as follows:

$$SD_{I_p}(\hat{B}_{MSE}) = \int_I \left(\int_B B \cdot p(B|I) dB - \int_B B \cdot p(B|I_p) dB \right)^2 \cdot p(I) dI$$

$$\hat{B}_{MSE} = E[B|I] = \int_B B p(B|I) dB$$

$$SD_I(\hat{B}_{MSE}) = \int_B (\hat{B}_{MSE}(i) - \hat{B}_{MSE}(I))^2 p(i) di$$

where $p(i)$ corresponds to a Gaussian probability density function centered on the value obtained at the pixel level and with an arbitrary standard deviation, depending on the AGB indicator : for γ_{hv}^0 and t^0 , standard deviations of 0.65 and 0.45 dB have been retained and are ensued from the respective maximum standard deviation from various dates and plots. For Pol-InSAR height, standard deviation of 2m (Figure 107) and 4m

(Figure 108) have been chosen, based on the expected height retrieval stability and on the cross comparison with Lidar heights.

Date\Metric	Intensity			Height			combined		
	rho	RMSE	MPE	Rho	RMSE	MPE	rho	RMSE	MPE
0-1-3	0.53	17.98	1.35	0.49	14.77	6.53	0.72	13.13	5.17
1-3-4	0.54	18.17	1.58	0.49	14.77	6.53	0.73	13.10	5.37
3-4-5	0.65	15.73	0.37	0.49	14.77	6.53	0.82	10.95	4.60
4-5-6	0.67	15.43	-0.03	0.49	14.77	6.53	0.85	10.42	4.22
<t ⁰ >	0.61	16.78	0.74	0.49	14.77	6.53	0.79	11.87	4.78

Table 7 : retrieval performances for the 4 sequences of 3 dates and last for the mean value. For each, a-priori coefficients a_1 and a_0 have been chosen (e.g 6.5 and -28 respectively for t^0) and the mean values from the various sequences (cf. table 1) over the 16 test plots are used for training.

Based on the pixel to pixel inversion Bayesian algorithm detailed above, maps of retrieved AGB have been performed using intensity, Pol-InSAR and their combination. For each, a-priori log-models have been used which are refined through the Bayesian estimator, accounting for bias and dispersion obtained on the 16 reference plots (cf. Bayesian formulation). As a matter of comparison, these maps are displayed in Figure 109, together with the one resulting from tomoSAR. The latter has been derived without using the Bayesian estimator but from the regression parameters obtained the fit between tomoSAR HV backscatter of the top forest layer and the in-situ AGB. These parameters are given in 6.3.3 whereas the overall tomoSAR method is described in [Ho Tong,2012] and WP 44.

RETRIEVAL MAPS :

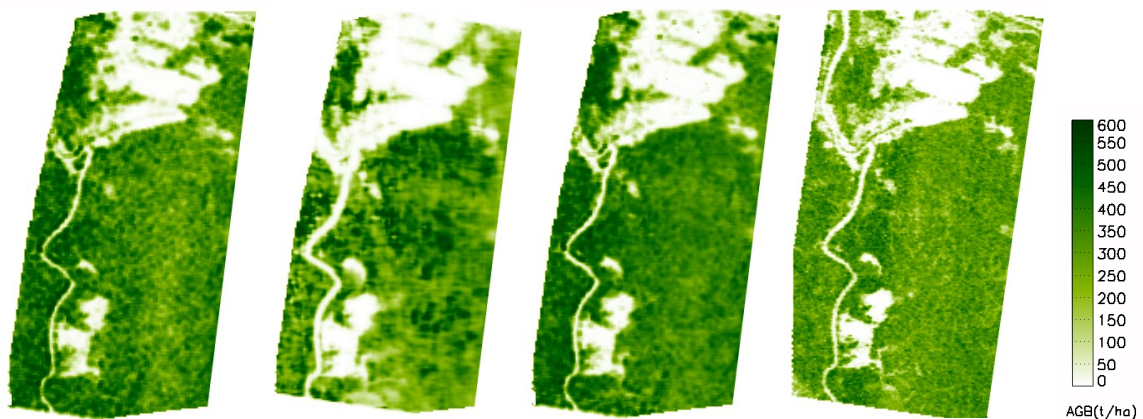


Figure 109 : from left to right are the 200m * 200m resolution images of retrieved AGB from intensity and Pol-InSAR based methods, followed by their combination and the 100m* 100m resolution image from tomoSAR.

6.3.3. IMPACT OF TOPOGRAPHY

As shown by the improvement brought by t^0 in comparison with γ_{hv}^0 (at 6MHz or 125MHz), topography can originate severe perturbations and hinder the backscatter-AGB relationship. Since the sensitivity to AGB and dispersion are about the same for t^0 or γ_{hv}^0 on the plots over moderate topography (cf. [Villard et al, 2013]),

topography effects are likely to be mostly removed. In addition, no significant correlation have been found between the retrieved AGB and topographic features, whether with the slope angles ψ_n , ψ_n^{rg} or ψ_n^{az} .

To assess the remaining errors on the estimated AGB, retrieved AGB from the combined method and from tomoSAR can be compared to in-situ AGB values on 16 reference plots (cf. Figure 110). As mentioned before, retrieval performances are in the same order of magnitude ($\rho \sim 0.8$ and $RMSE \sim 10\%$), though the training methods are different.

In figure 10, errors bars for the combined intensity/Pol-InSAR method result from the afore-detailed Bayesian formulation whereas for tomoSAR, the errors bars result from the statistical uncertainties related to the regression. Using a power law between tomoSAR HV backscatter and AGB, a correlation coefficient $\rho = 0.84$ has been obtained according to the following relationship:

$$[I_{hv}^{tomo} [dB] + 36.59(\pm 5.56)] = AGB[t/ha]^{11.64(\pm 2.18)}$$

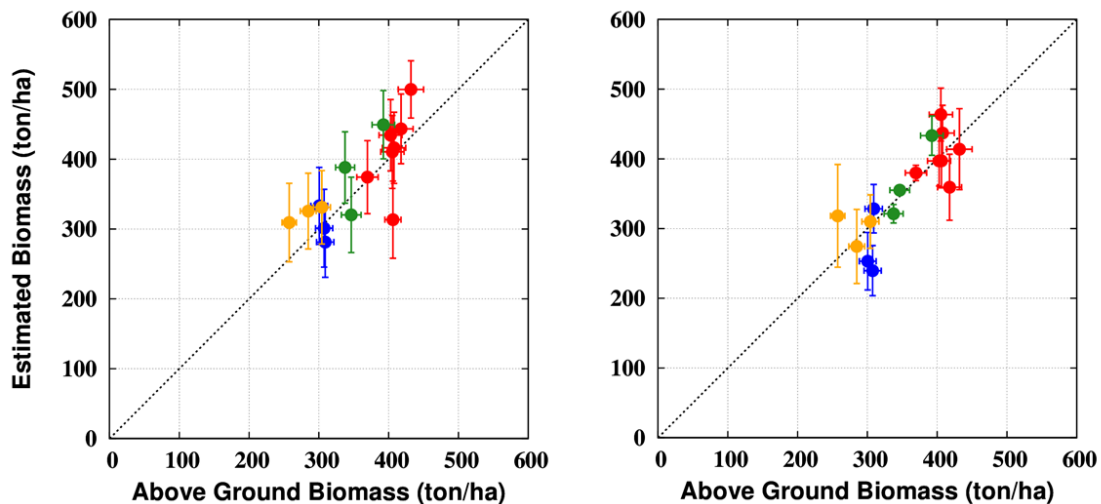


Figure 110 : Retrieved versus in-situ AGB using the combined Bayes method from intensity and Pol-InSAR on the left and using the tomoSAR backscatter on the right.

6.3.4. IMPACT OF FILTERING/TEMPORAL VARIATIONS

To assess the impact of a smaller number of looks, only one date (i.o sequence of 3 dates) has been used to derive t^0 . Except for the third acquisition (August 14) -- which has been previously explained and flagged -- retrieval performances keep the same order of magnitude and the effects of lower intensity based retrieval performances are mitigated by the combined use with Pol-InSAR height.

[Table to be added: retrieval performance from t^0 estimated using a single date/temporal look]

6.3.5. CONCLUSIONS

As for 125MHz data, the ad-hoc backscattering coefficient t^0 is required to reduce topographic effects and recover the small sensitivity to AGB for values above 300 t/ha.

Regarding relationship between t^0 and AGB, a power law can be used as for the 125 MHz data with in addition regression parameters (slope and intercept) in the same order of magnitude (especially for the slope/sensitivity about 6.5 ± 2).

Retrieval based on intensity at 6MHz has been shown feasible, with correlation coefficients ranging between 0.53 and 0.67 and RMSE between 15 and 18%, according to the various sequences of dates. To get these results, it can be stressed that a general log relationship has been used (with a-priori slope and intercept values) in the Bayesian formulation, which was tuned with the 16 reference plots. In addition, the use of only one acquisition is mostly not critical, excepted for one date for which the wind conditions originate a significant noise to estimate the backscatter coefficients.

Retrieval based on Pol-InSAR height at 6MHz has been also shown feasible, with slightly better performance than intensity in terms of RMSE (~15%) but with much lower correlation coefficient ρ (~0.5), especially due to some outlier plots. As for intensity, training plots are required when using a general or a-priori log-relationship.

Finally, significant improvements of the performance results have been demonstrated with the combined use of intensity and Pol-InSAR height. Indeed, perturbations sources for both methods are mostly independent so that their effects are mitigated and thereby reduced. Retrieval performances of the combined method are in the same order of the ones based on tomoSAR technique, though the training algorithms are different.

6.3.6. REFERENCES

[Biomass, 2012] "Report for Mission Selection: BIOMASS", *ESA SP-1324/1* (2012).

[Dubois-Fernandez et al., 2012] Dubois-Fernandez, P. C. and Le Toan, T. and Daniel, S. and Oriot, H. and Chave, J. and Blanc, L. and Villard, L. and Davidson, M. W. J. and Petit, M., "The TropiSAR Airborne Campaign in French Guiana: Objectives, Description, and Observed Temporal Behavior of the Backscatter Signal", *Geoscience and Remote Sensing, IEEE Transactions on* (2012), 1 -14.

[Hoekman et al, 2000] DH Hoekman, M. Quinones . «Land cover type and biomass classification using AirSAR data for evaluation of monitoring scenarios in the Colombian Amazon». 2000, *IEEE Trans. Geosci. Remote Sensing*, pp. p685-696, vol 38.

[Ho Tong et al., 2012] Dinh Ho Tong Minh and Thuy Le Toan and Fabio Rocca and Stefano Tebaldini and Mauro Mariotti d'Alessandro and Ludovic Villard, "Relating P-Band SAR Tomography to Tropical Forest Biomass", *IEEE Transactions on Geoscience and Remote Sensing*, 2012.

[Saatchi et al, 2007] S.S. Saatchi , K. Halligan, Despain DG and Crabtree RL. «Estimation of forest fuel load from radar remote sensing.» *IEEE Trans. Geosci. Remote Sensing*, 2007: p1726-1740, vol 45, no. 6.

[TropiSAR, 2011] P. Dubois-Fernandez, H. Oriot, T. Le Toan, J. Chave, S. Cherchali, and M. Davidson, "Technical Assistance for the Development of Airborne SAR and Geophysical Measurements During the TropiSAR 2009 Experiment". ESA Communication Production Office, Feb 2011, vol. ESA contract N 22446/09/NL/CT, CNES contract N92929 03/08/09.

[Lee et al, 2000] J-S Lee, D.L. Schuler, T.L. Ainsworth, E. Krogager, D. Kasilingam, and W-M. Boerner. «On the estimation of radar polarization orientation shifts induced by terrain slopes.» *Geoscience and Remote Sensing, IEEE Transactions on*, 2000: p30–41, vol. 40, no 1.

[Lee et al, 2011] J.S Lee, T.L. Ainsworth «The effects of orientation angle compensation on coherency matrix and Polarimetric Target Decomposition.» *IEEE Trans. Geosci. Remote Sensing*, 2011: vol. 49, January.

[Le Toan et al., 2011] Le Toan, T. and S. Quegan and M. Davidson and H. Balzter and P. Paillou and K. Papathanassiou and S. Plummer and F. Rocca and S. Saatchi and H. Shugart and L. Ulander, "The BIOMASS Mission : Mapping global forest biomass to better understand the terrestrial carbon cycle", *Remote Sensing of Environment* (2011), 2850-2860.

[Villard et al, 2010] L. Villard, P. Borderies, T. Le Toan, T. Koleček and C. Albinet. «Topographic effects on forest radar scattering, consequences on biomass retrieval.» *Proceedings in IGARSS*, 2010.

[Villard et al, 2013] L. Villard and T. Le Toan. «Relating P-band SAR Intensity to Biomass for Tropical Dense Forests in Hilly Terrain : γ^0 or t^0 ?» submitted to Journal of Selected Topics in Applied Earth Observations and Remote Sensing (JSTARS) 2012.

6.4.WP 44: PERFORMANCE ANALYSIS TOMOGRAPHY

6.4.1. 6 MHZ DATA GENERATION

As discussed in the introduction, two different approaches can be considered to derive a data-stack consistent with BIOMASS specifications from the TropiSAR airborne data-set.

One is to operate on each image from TropiSAR at a time in such a way as to reduce its resolution and make it consistent with BIOMASS specifications. The resulting data is consistent with BIOMASS concerning spatial resolution, whereas system geometry (i.e.; LOS) is the same as in the airborne case. This kind of data-set has been provided by ONERA in the frame of this CCN.

The other approach consists in emulating a spaceborne geometry as well. This can be done in two steps:

1. jointly processing the TropiSAR data stack through TomSAR techniques, to recover a high resolution three dimensional reconstruction of the scene reflectivity at Paracou;
2. Employ a 3D SAR simulator to project the result onto BIOMASS geometry.

Step 1 was already performed by PoliMi during previous researches; see [Mariotti and Tebaldini, 2012]. Step 2 was implemented in the frame of this CCN to generate emulated BIOMASS data at the Paracou forest site. Step 2 was carried out by modifying the BIOMASS simulator employed in [Ionosphere, 2012] so as to take as input the 3D scene reflectivity at the Paracou test site.

We will hereinafter refer to the two kinds of BIOMASS data depicted above simply by the names of airborne geometry and spaceborne geometry.

A full discussion about spaceborne geometry data generation is provided in the remainder of this next section.

SAR DATA MODEL

BIOMASS SAR data have been simulated in such a way as to synthesize a stack of Single Look Complex (SLC) SAR images in radar geometry (slant range, azimuth), taking as input the parameters of the acquisition system (carrier frequency, pulse bandwidth, resolution, look angle etc.), platform orbits, and the scene to be imaged. The input scene, that is the key of feature of this simulation, was derived from the TropiSAR airborne data-set through SAR Tomography techniques; see [Mariotti and Tebaldini, 2012].

The data stack is simulated by synthesizing each pixel in each SAR image according exactly to the well-known forward model [Bamler and Hartl, 1998]:

$$y_n(\mathbf{r}, \mathbf{x}, AB) = \int f(\mathbf{r} - \mathbf{r}', \mathbf{x} - \mathbf{x}') S(\mathbf{r}', \mathbf{x}', \xi; AB) \exp\left(i \frac{4\pi}{\lambda} R_n(\mathbf{r}', \mathbf{x}', \xi)\right) d\xi$$

Equation 15

Where:

(r,x,ξ) are the slant range, azimuth and cross range coordinates with respect to a fixed master image,

$AB = \{HH, HV, VH, VV\}$ indicates the polarization,

$y_n(r,x,AB)$ is the complex valued pixel at slant range, azimuth location (r,x) , in the SLC SAR image corresponding to track n , polarization AB ,

$S(r,x,\xi;AB)$ is the wide-band complex reflectivity, i.e. the complex reflectivity of the elementary scatterer at location (r,x,ξ) in polarization AB ,

$R_n(r,x,\xi)$ is the zero-Doppler distance between the orbit of the n -th acquisition and the elementary scatterer at location (r,x,ξ) ,

$f(r,x)$ is the end to end impulse response function of the BIOMASS system.

The wide-band complex reflectivity was characterized by using the 3D scene reflectivity derived from TropiSAR data, see [Mariotti and Tebaldini, 2012], [Ho Tong et al., 2012]. Its statistics are set in such as to emulate both the vertical structure and the polarimetric behavior of forest scattering at each range and azimuth location. As a result, the simulation is consistent with real data from the TropiSAR campaign.

For sake of simplicity we have neglected system noise and clutter, and assumed electromagnetic reciprocity (i.e.: $S_{HV} = S_{VH}$).

A block scheme of the simulator is shown in Figure 111.

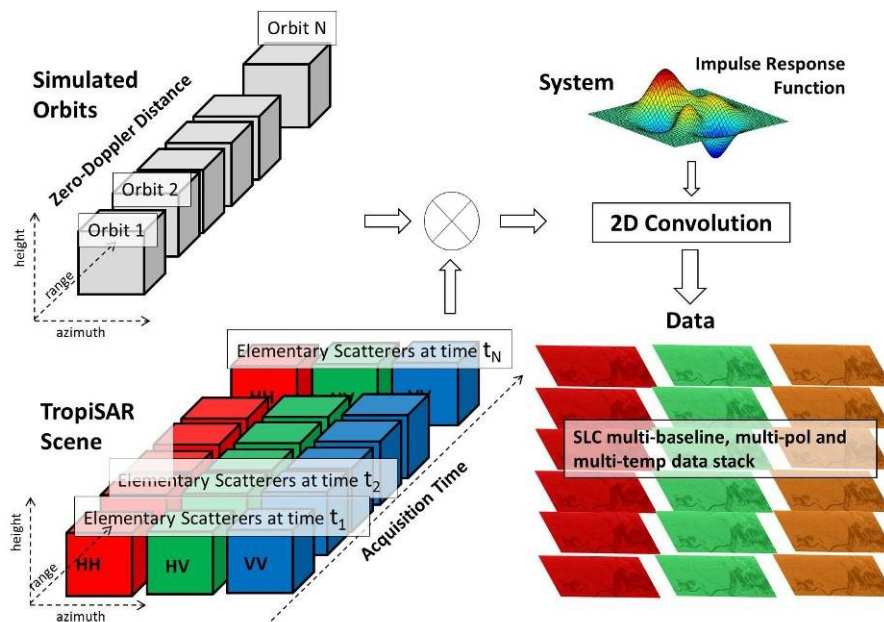


Figure 111: BIOMASS SAR simulation

IMPULSE RESPONSE FUNCTION

The system end to end impulse response function is simulated through a separable model with respect to the azimuth and range axes, i.e.:

$$f(r,x) = f_r(r) \cdot f_a(x)$$

The range impulse response function f_r , and the azimuth f_a , both belonging to the raised-cosine function family, are shown in Figure 111 and Figure 112. Range pulse envelope has been modeled so as to ensure an attenuation of 40 dB at ± 3 MHz. Each image is generated with an oversampling factor of 4 in both the slant range and the azimuth directions.

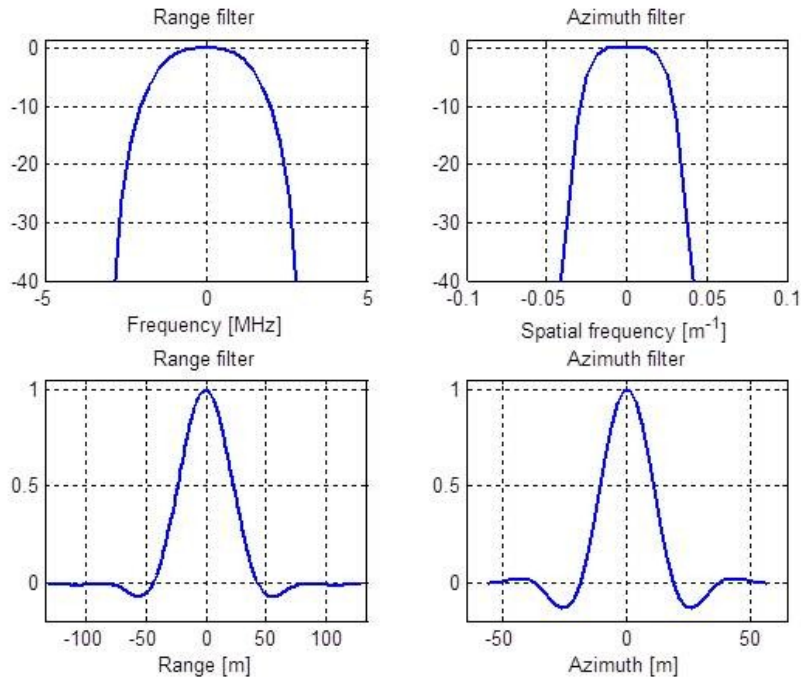


Figure 112: Range and azimuth IRF for BIOMASS SAR simulation

BIOMASS PARAMETERS

Baseline aperture and spacing have been set based on the achievable resolution and height of ambiguity. As shown in [Tebaldini and Rocca, 2010], vertical resolution depends not only on baseline aperture but also on system bandwidth. Projecting the slant range and cross range extent of the resolution cell along the vertical direction, one easily gets that the vertical resolution is limited as:

$$\Delta z^{(bandwidth)} = \frac{c}{2B} \cos\theta$$

Equation 16

$$\Delta z^{(baseline)} = \frac{\lambda r}{2A_z} \sin\theta$$

Equation 17

Equating the two limits to vertical resolution ($\Delta z^{(bandwidth)} = \Delta z^{(baseline)}$), it is readily obtained that:

$$A_z = \frac{B}{f_c} r \tan\theta = b_{crit}$$

Equation 18

Therefore, we get the result that the finest vertical resolution is obtained by letting the overall baseline aperture equal the critical baseline.

Baseline spacing determines the height of ambiguity, according to the well-known relation:

$$z_{amb} = \frac{\lambda r \sin\theta}{2 \Delta b}$$

Equation 19

In a TomSAR campaign, height of ambiguity has to be larger than the expected forest height, so as to avoid superposition of the replicas. A safe choice is typically to set the height of ambiguity equal to at least twice the forest height. Assuming a vegetation layer of 50 m, the resulting number of passages for tomographic imaging can be assessed in about 6 tracks (height of ambiguity 110 m) per site, by letting baseline aperture equal the critical baseline.

Item	Characteristics
Satellite altitude	650 km
Incidence angle	25°
Carrier frequency	435 MHz
Bandwidth	6 MHz
Critical baseline	4610 m
Range resolution	25 m
Azimuth resolution	12.5 m
Number of passes	7
Baseline aperture	4610 m (critical)

Table 8 : BIOMASS parameters for simulation

BIOMASS parameters used for data generation are summarized in Table1.

The employment of a 6 MHz bandwidth and a 25° Incidence angle result in a ground range resolution on the order of 60 m (assuming flat terrain) and a vertical resolution on the order of 20 m.

The implemented TomSAR processing is aimed at converting the *multi-baseline* stack of SAR images into a *multi-layer* stack of SAR images, where each image represents the complex reflectivity associated with a layer at a certain height above the ground.

The processing chain is hereafter briefly recalled for sake of completeness. For more details, the reader is referred to [Mariotti and Tebaldini, 2012], [Ionosphere, 2012].

Data phase calibration is carried out according to the two-step procedure proposed in [Tebaldini and Rocca, 2009]. In the first step the Algebraic Synthesis technique is used to recover the matrix of interferometric coherences associated with ground-only contributions [Tebaldini, 2009]. In the second step the Phase Linking algorithm is used to retrieve the best estimate of the ground phases [Tebaldini and Rocca, 2009].

Phase calibration is then performed by removing the retrieved ground phases φ_n^{ground} from the SLC data stack. It is important to note that the retrieved ground phases are directly related to the optical paths from the ground layer to the N sensor positions, and are therefore determined not only by terrain topography, but also by the phase disturbances deriving orbit inaccuracies, atmospheric and ionospheric propagation [Iono]. Accordingly, removing the ground phases brings two advantages. The first is the removal of the propagation disturbances, which allows a correct focusing along the vertical direction. The second is the removal of terrain topography, resulting in the contributions from the terrain to be automatically focused at 0 m, independently of the actual topography. In formula:

$$\hat{y}_n = y_n(r, x) \exp\left(-j \varphi_{nm}^{ground}\right)$$

Equation 20

$$\varphi_{nm}^{ground} = \varphi_n^{ground} - \varphi_m^{ground} = \frac{4\pi}{\lambda r \sin\theta} b_n z_g$$

Equation 21

Where b_n is the normal baseline relative to the n-th image.

After phase flattening, at a given azimuth plane x and slant range r , in the n-th SLC SAR image, the complex valued pixel $y_n(r, x)$ can be expressed through :

$$y_n(r, x) = \int S(\xi, r, x) \exp\left(+j \frac{4\pi}{\lambda r} b_n \xi\right) d\xi$$

Equation 22

Equation 22 states that SAR multi-baseline data and the cross range distribution of the scene reflectivity constitute a Fourier pair. Hence, the latter can be retrieved by taking the Fourier Transform of the data along the baseline direction. The final conversion from cross range to height is then obtained through straightforward geometrical arguments.

Such a focusing approach provides resolution capabilities consistent with the well-known Rayleigh limit [Reigber and Moreira, 2000], [Lombardini and Reigber, 2002]. A common issue of SAR tomographic surveys is that the resolution allowed by the Rayleigh limit is often too coarse if compared to the vertical extent of the observed scene. For this reason, tomographic processing is usually carried out by employing super-resolution techniques; see for example [Gini et al., 2003]. Although such techniques allow recovering details not accessible otherwise, they result in poor radiometric accuracy in the case of distributed targets, which limits their application to the aim of yielding quantitative measurements in a completely model-free fashion. This task, however, becomes possible whenever the available baseline set allows it, as it is the case of the TropiSAR data-set, resulting in the possibility to carry out model-free, unbiased measurements of the vertical

distribution of the backscattered power. For this reason image formation along the vertical direction has been carried out in simply by coherent focusing, that is by Fourier transforming the data with respect to the normal baseline. This way of processing does not optimize vertical resolution. Yet, it grants radiometric accuracy along the vertical direction, which is a mandatory requirement to the aim of linking forest biomass to backscatter measurements.

The result of this operation is a multi-layer SLC set, where each layer is referred to a fixed height above the terrain. We will hereinafter refer to each image within the multi-layer data stack simply by the associated height (i.e.: 10 m layer, 20 m layer...), or as ground layer for the image focused at 0 m.

6.4.3. TOMSAR RESULTS

Figure 113 shows the HH backscattered power for the layers at 0 m, 15 m, 30 m at 45 m, as derived by processing the airborne geometry data. As noted in [Mariotti, 2012] the ground layer (0 m) and top layer (45 m) show strong topographic effect, whereas the 30 m layer m is observed to be less affected by topography.

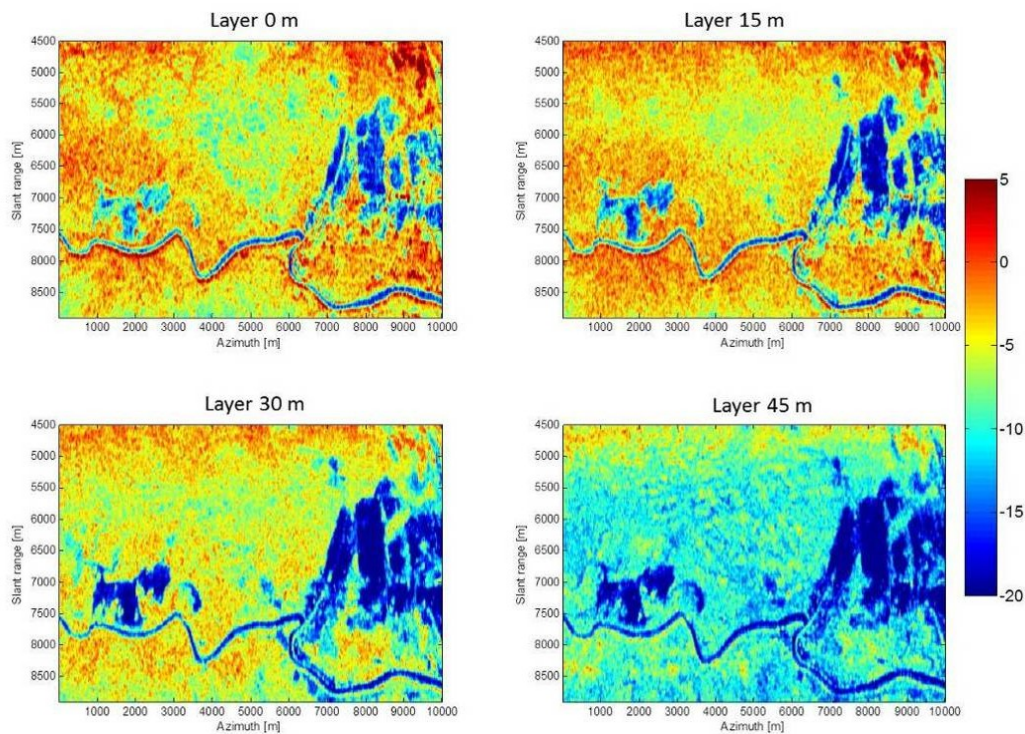


Figure 113: HH backscattered power for the layer at the four levels in airborne geometry.

Figure 114 reports a tomographic profile along a constant azimuth section in the HV polarization, considering three cases: 125 MHz data (top panel), 6 MHz airborne geometry data (middle panel), 6 MHz spaceborne geometry data (bottom panel). The white line denotes the LiDAR height measurements, shown for comparison with the TomSAR profile. Neither ionospheric disturbances nor temporal decorrelation have been considered.

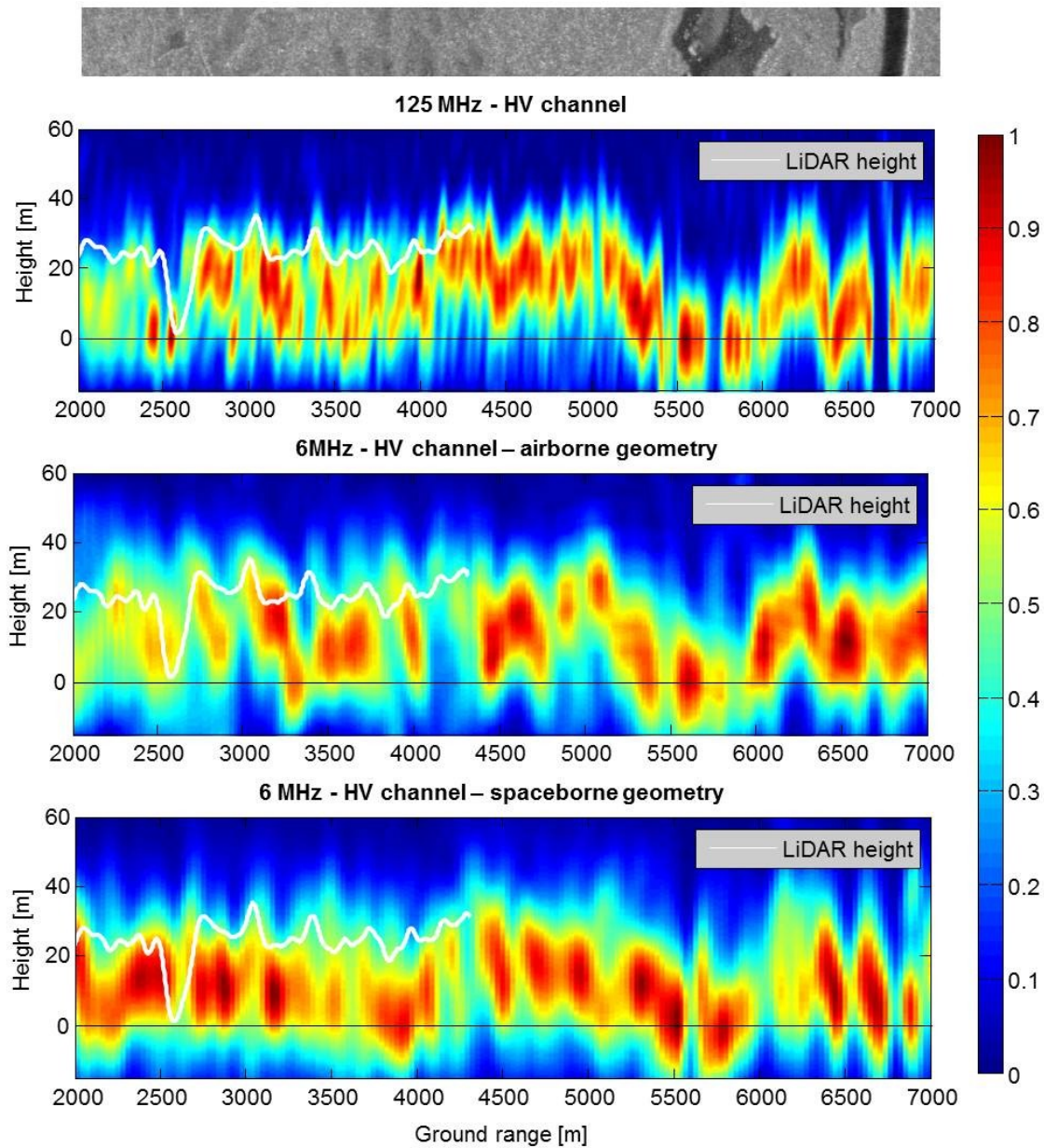


Figure 114: Tomographic reconstruction along the same azimuth cut in HV polarizations at 125 MHz and 6 MHz in both geometries. The white line denotes the LiDAR height measurements. All panels have been normalized in such a way that the sum along height is unitary.

A vertical resolution loss is clearly noticeable in the passage from 125 MHz to 6 MHz, concerning both airborne and spaceborne geometry data. The airborne geometry tomogram is clearly characterized by a vertical resolution variation with respect to range, whereas vertical resolution is observed to be uniform in the spaceborne geometry case, as expected.

6.4.4. CORRELATION BETWEEN TOMSAR AND ABOVE GROUND FOREST BIOMASS

The analysis in this section is focused on the relationship between the backscattered power associated with layers at different height and in-situ AGB measurements.

In-situ measurements consist of 16 permanent plots established starting 1984 in the Paracou primary forest. These are 15 plots of 250x 250 m (6.25 ha) each and one plot of 500x500 m (25 ha). In order to increase the number of plots, these have been subdivided into subplots. In this report, plots 1 to 15 are subdivided into 4 subplots of 125x125 m (1.5 ha), while plot 16 is divided into 25 subplots of 100 times 100 m (1 ha), resulting in 85 independent subplots for which AGB data are available.

Figure 116 displays the backscatter power in HV plots as a function of in-situ AGB as measured over the 2.5 ha plots, considering 9 layers varying from 0 m to 40 m, at 5 m interval.

Similarities between two geometries are observed. For the layers under 20 m, the Pearson linear correlation r_P between the backscatter backscattering coefficient and AGB is very weak (and negative). For layers from 20 m 40 m the correlation between backscatter and AGB becomes instead highly significant.

The 30 m layer exhibits the highest correlation value with respect to in-situ data and no bias phenomena over AGB values ranging from 250 t/ha to 450 t/ha. For the 35 m layer, the backscatter dynamic range is larger, but the correlation is reduced and the dispersion is increased. For the top layer (40 m), the correlation decreases and the dispersion increases as well. This result indicates that the 30 m layer appears to be the most suited for biomass retrieval at the Paracou test-site, by virtue of its high correlation with in-situ measurements. This result is consistent with the one obtained by processing the full-bandwidth (125 MHz) TropiSAR data [Ho tong et al., 2012].

Based on the results and the discussion provided above, an estimator was defined to retrieve AGB based on the backscattered power in HV at 30 m above the ground. Performance assessment is carried out by evaluating the Root Mean Square Error (RMSE) between in-situ measurements and estimated AGB values. Results are reported in Figure 116. The RMSE turned out to be lower than 10% on the 6 ha plots, and lower than 20% on the 1.5 ha plots, with no significant difference between the airborne geometry and spaceborne geometry cases.

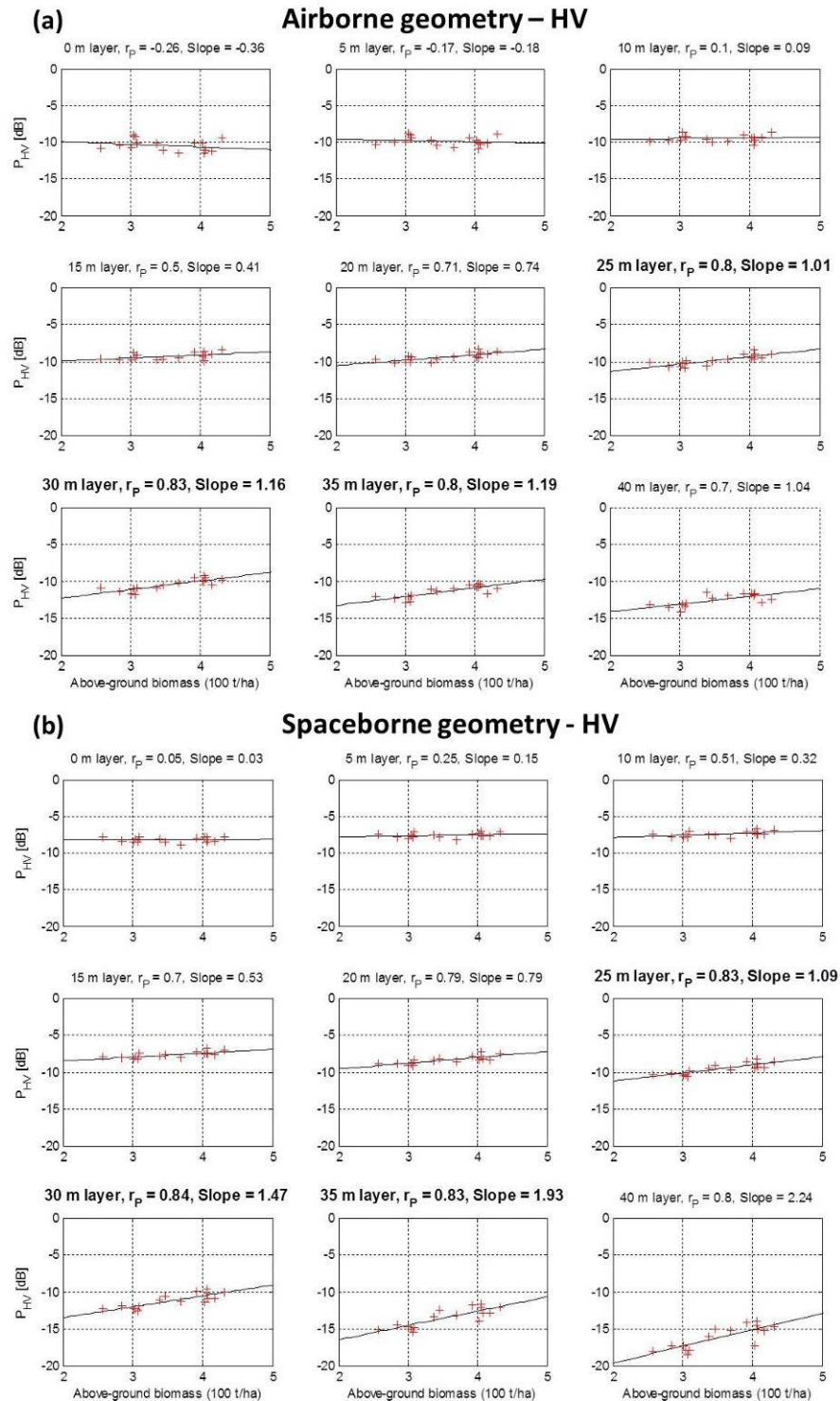


Figure 115: Sensitivity of backscatter power at different layers to above-ground biomass in HV channel in both geometries. r_p is the Pearson correlation coefficient. The term “slope” is referred to the angular coefficient of the linear regression. Plot size is 250x250 m.

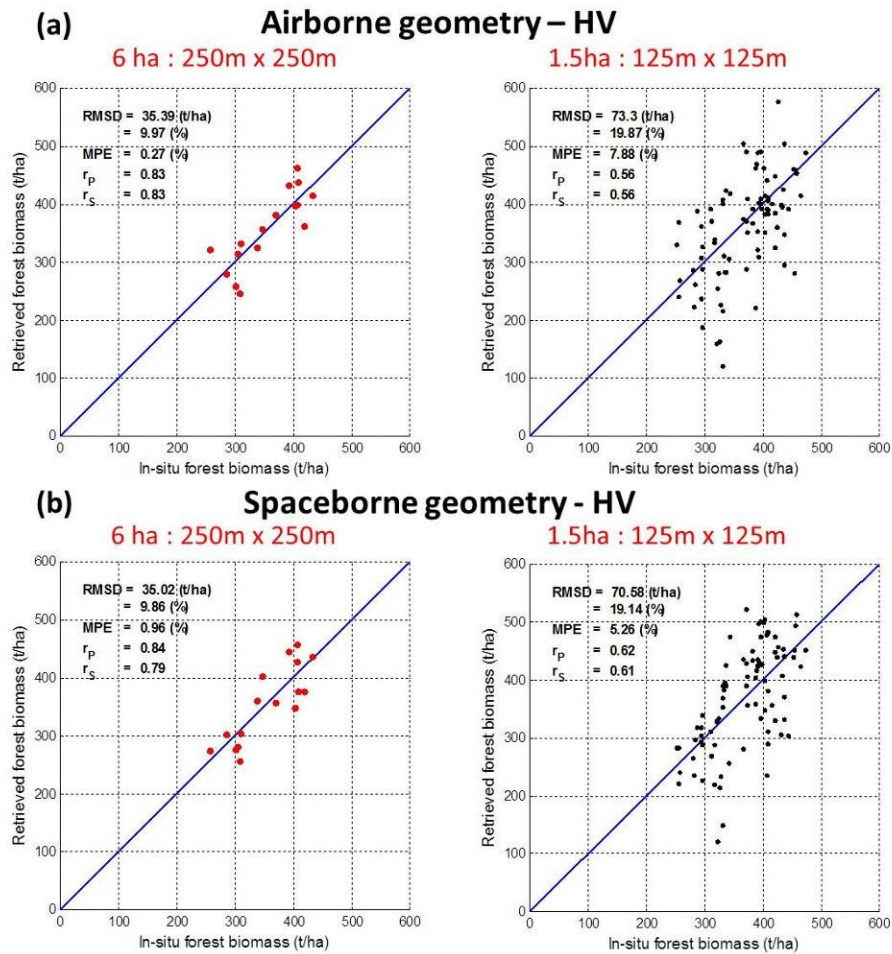


Figure 116: Comparison between in-situ biomass and biomass derived from inversion of the P-band HV 30 m layer in both geometries.

6.4.5. FOREST HEIGHT ESTIMATION

The retrieval of forest height has been assessed through a direct investigation of the shape of the 3D backscattered power distributions from the multi-layer SLC at each location, considering the HV polarimetric channel.

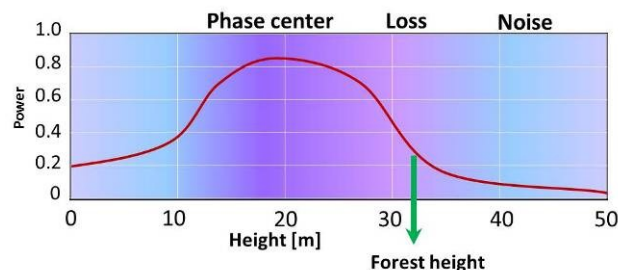


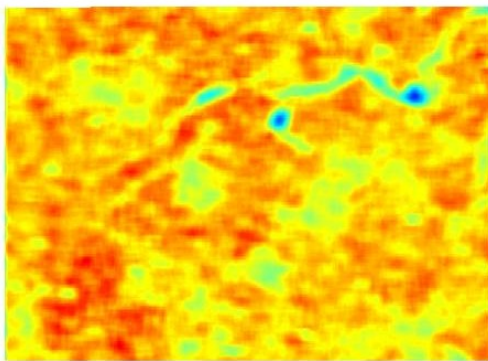
Figure 117: Criterion for the retrieval of forest height

The criterion adopted in assessing forest top height follows after the basic assumption that the shape of the backscattered power distribution can be roughly divided into three zones, see Figure 117. One is found in correspondence with the phase center location, where most of the backscattered power is concentrated.

Then, the backscattered power undergoes a loss due to both the point spread function of the tomographic processors and the (eventual) tapering of forest density. Further away along the vertical direction, the backscattered power is mostly contributed by noise, resulting in this zone not to be likely associated with physically relevant components. Accordingly, forest height has been retrieved by evaluating the power loss from the phase center location (Tebaldini and Rocca, 2012).

Results relative to height estimation area are shown in Figure 118. Forest height as measured by LIDAR is shown in Figure 118 a) to facilitate the interpretation of the results. . Both LIDAR and tomographic forest height are filtered by an average window of 100 x 100 m. A good agreement with LIDAR is observed both in airborne and spaceborne geometry cases, see Figure 118 b) and c). The average relative error was assessed in about 13% in the airborne geometry case and 10% in the spaceborne geometry case.

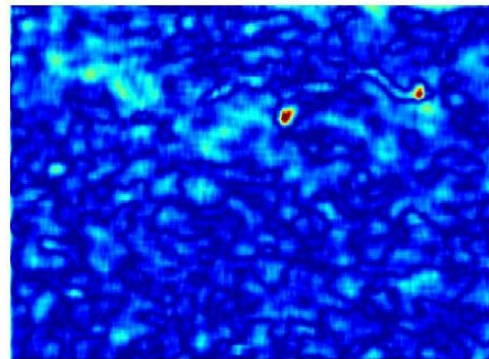
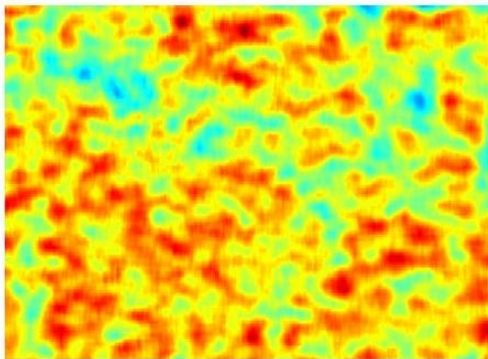
(a) LiDAR



Relative error

$$\frac{|H_{\text{tomography}} - H_{\text{LiDAR}}|}{H_{\text{LiDAR}}}$$

(b) Airborne geometry



(c) Spaceborne geometry

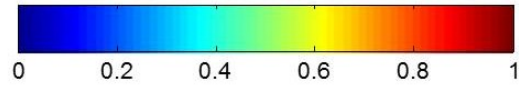
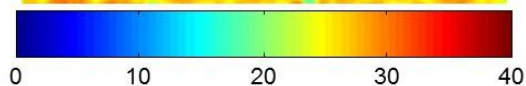
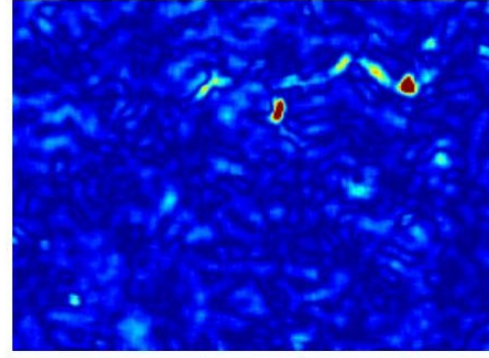
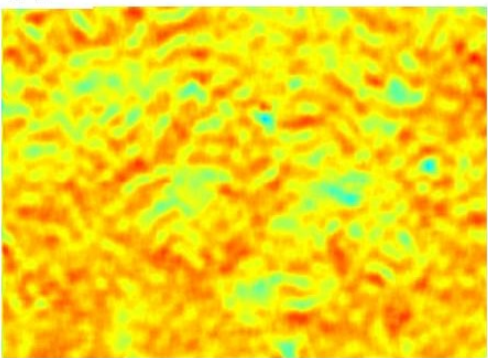


Figure 118: Comparison between LiDAR and tomography retrieval of forest height in both geometries. Both LiDAR and tomographic forest height are filtered by an average window of 100 x 100 m.

The joint distribution of forest height as measured by LiDAR and TOMSAR is shown in Figure 119. The distribution has been normalized such that the maximum is unitary along each column. The estimation appears to be reliable for vegetation layers ranging from 20 m to nearly 35 m. For this range height, standard deviation has been assessed in about 4 m.

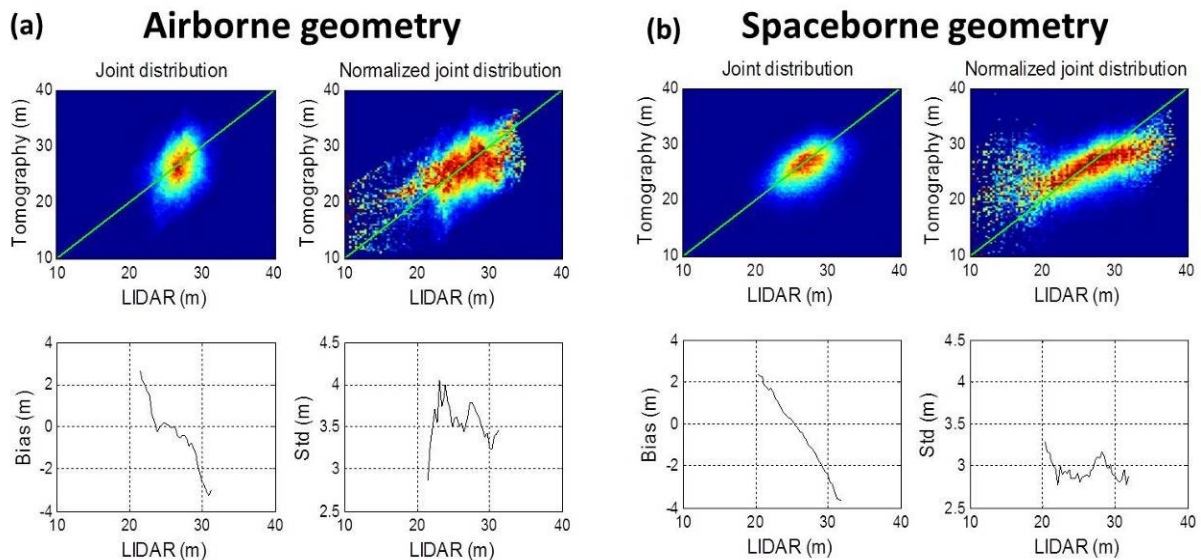


Figure 119: Joint distribution between LiDAR and TomSAR (6 MHz) forest height. (a): airborne geometry. (b) spaceborne geometry.

Slightly better results can be obtained by modifying the TomSAR processor by employing the Capon filtering techniques. Results are shown in Figure 120.

Algorithm : Capon spectrum (With CBF)

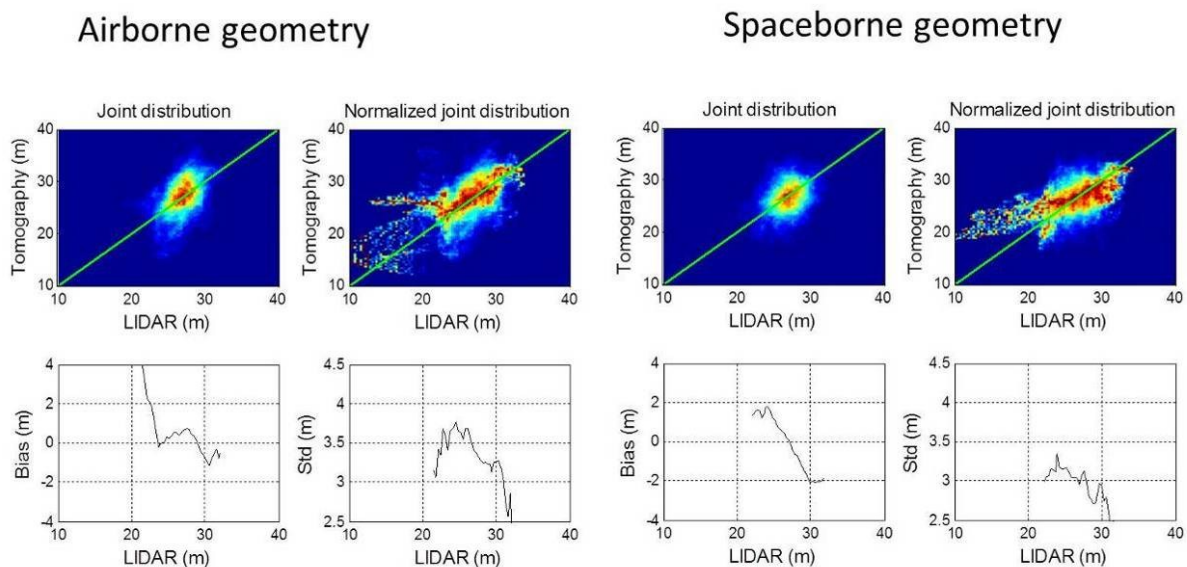


Figure 120: Joint distribution between LiDAR and TomSAR (6 MHz) forest height. (a): airborne geometry. (b) spaceborne geometry. TomSAR processing is carried out through Capon filtering techniques.

For sake of completeness we recall here results relative to forest height estimation obtained by processing the 6 MHz emulated BIOMASS data produced by DLR in the frame of the ESA campaign BIOSAR 2008, see [Rocca and Tebaldini, 2009]. The illuminated scene is the boreal forest within the Krycklan river catchment, Northern Sweden. In this case standard deviation was observed to be about 3.5 m, with no significant bias between 12 and 20 m.

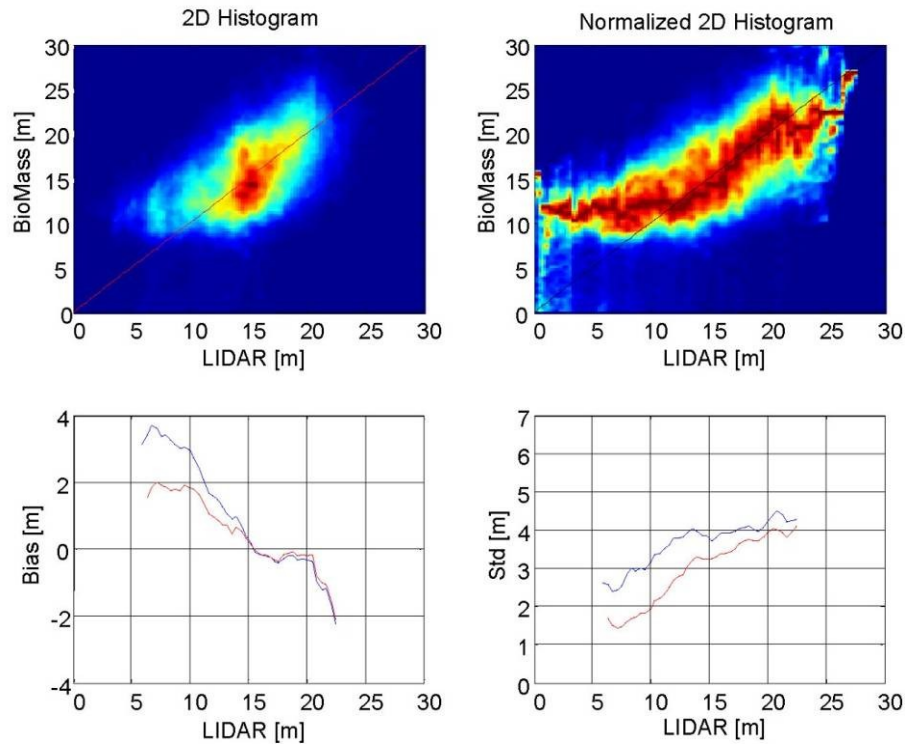


Figure 121: Joint distribution between LiDAR and TomSAR (6 MHz) forest height at Krycklan, Northern Sweden. The red line has been obtained by discarding pixel associated with a relative error larger than 0.5. Results are relative to the 6 MHz emulated BIOMASS data produced by DLR in the frame of the ESA campaign BIOSAR 2008.

6.4.6. CONCLUSIONS

This work has focused on assessing the performance of P-Band multi-baseline TomSAR about the retrieval of forest biomass and height in tropical forests, accounting for the 6 MHz bandwidth limitation imposed by ITU regulations to the BIOMASS mission. As a result of such limitation, 6 MHz tomography is hindered by two different factors compared to airborne tomography, that is: i) a significant reduction of the number of looks to be used for coherence evaluation, ii) a significant vertical resolution loss.

The data considered in this work were derived from the airborne data-set TropiSAR. Two different kinds of 6 MHz data were considered:

Airborne geometry data were derived by degrading the resolution of airborne data through linear filtering. This approach has the main advantage of being fast, although it does not allow having the same LOS as the emulated spaceborne system along the whole imaged swath. This approach was pursued by ONERA, which provided a 6 MHz data stack generated according to this procedure.

Spaceborne geometry data were derived by first recovering the 3D distribution of the scatterers at high resolution, which was then re-projected onto BIOMASS geometry accounting for the available

radiofrequency bandwidth. This procedure allows obtaining a data stack that is consistent with BIOMASS concerning not only spatial resolution, but also geometrical features, i.e.: system LOS.

The same TomSAR processor was used to process both the airborne and spaceborne data-sets, resulting in two data cubes providing a 3D reconstruction of the Paracou forest site at 6 MHz.

The most relevant difference between the airborne and spaceborne data-sets was observed relatively to the vertical profiles yielded by the TomSAR processor, in that airborne geometry data were clearly affected by a varying vertical resolution with respect to range.

Though, no relevant difference was observed between the airborne and spaceborne cases concerning the sensitivity to Above Ground Biomass (AGB), as obtained through in-situ measurements over forest plots. The 30 m layer was found to exhibit a correlation value with respect to AGB higher than 0.8 for AGB values ranging from 250 t/ha to 450 t/ha. This result is consistent with the one obtained by processing the full-bandwidth (125 MHz) TropiSAR data [Ho Tong et al., 2012].

An estimator was defined to retrieve AGB based on the backscattered power in HV at 30 m above the ground. The achieved relative accuracy turned out to be better than 20% at 1.5 ha resolution and better than 10% at 6 ha resolution.

Forest height was estimated by tracing the upper envelope of TomSAR vertical profiles, as averaged over a 100 m x 100 m window. Height estimation turned out to be reliable for vegetation layers ranging from 20 m to 30-35 m, which is consistent with the relative high forest height in tropical forest areas. For this range of forest height, standard deviation has been assessed in less than 4 m.

The results of this study prove that the 6 MHz bandwidth limitation is not to be considered critical concerning TomSAR analyses of tropical forests. This can be qualitatively understood by considering that the employment of a 6 MHz bandwidth and a 25° incidence angle results in a ground range resolution on the order of 60 m (assuming flat terrain) and a vertical resolution on the order of 20 m. Accordingly, TomSAR processing can be successfully employed to decompose the backscattered power from a tropical forest into two-three layers, and hence provide valuable information about the forest structure.

The same conclusion cannot be straightforwardly extended to the case of boreal forests, whose average height is about 20 m, despite the good results obtained at 6 MHz in the frame of the BioSAR 2008 campaign, see [Rocca and Tebaldini, 2009].

We remark that ionospheric disturbances and temporal decorrelation have not been considered in BIOMASS data generation.

6.4.7. REFERENCES

[Bamler and Hartl, 1998] Richard Bamler and Philipp Hartl, "Synthetic aperture radar interferometry" (1998), R1-R54.

[BIOMASS, 2012] "Report for Mission Selection: BIOMASS", *ESA SP-1324/1* (2012).

[Dubois-Fernandez et al., 2012] Dubois-Fernandez, P. C. and Le Toan, T. and Daniel, S. and Oriot, H. and Chave, J. and Blanc, L. and Villard, L. and Davidson, M. W. J. and Petit, M., "The TropiSAR Airborne Campaign in French Guiana: Objectives, Description, and Observed Temporal Behavior of the Backscatter Signal", *Geoscience and Remote Sensing, IEEE Transactions on* (2012), 1 -14.

[Gini et al., 2002] Gini, F. and Lombardini, F. and Montanari, M., "Layover solution in multibaseline SAR interferometry", *Aerospace and Electronic Systems, IEEE Transactions on* (Oct 2002), 1344-1356.

[Ho Tong et al., 2012] Dinh Ho Tong Minh and Thuy Le Toan and Fabio Rocca and Stefano Tebaldini and Mauro Mariotti d'Alessandro and Ludovic Villard, "Relating P-Band SAR Tomography to Tropical Forest Biomass", *Geoscience and Remote Sensing, IEEE Transactions on* (Submitted, 2012).

[Ionosphere, 2012] Study of Ionospheric Mitigation Schemes and their Consequences for BIOMASS Product Quality, ESA/ESTEC Contract No. 22849/09/NL/JA/ef.

[ITU, 2004] ITU-2004, "Article 5 (Frequency Allocations) of the radio regulations", International Telecommunication Union (2004).

[Le Toan et al., 2011] Le Toan, T. and S. Quegan and M. Davidson and H. Balzter and P. Paillou and K. Papathanassiou and S. Plummer and F. Rocca and S. Saatchi and H. Shugart and L. Ulander, "The BIOMASS Mission : Mapping global forest biomass to better understand the terrestrial carbon cycle", *Remote Sensing of Environment* (2011), 2850-2860.

[Lombardini and Reigber, 2003] Lombardini, F. and Reigber, A., "Adaptive spectral estimation for multibaseline SAR tomography with airborne L-band data", *Geoscience and Remote Sensing Symposium, 2003. IGARSS '03. Proceedings. 2003 IEEE International* (2003), 2014-2016.

[Mariotti and Tebaldini, 2012] Mariotti d'Alessandro, M.; Tebaldini, S.; , "Phenomenology of P-Band Scattering From a Tropical Forest Through Three-Dimensional SAR Tomography," *Geoscience and Remote Sensing Letters, IEEE* , vol.9, no.3, pp.442-446, May 2012.

[Reigber and Moreira, 2000] A. Reigber and A. Moreira, "First demonstration of Airborne SAR tomography using multibaseline L-band data", *IEEE Trans. on Geoscience and Remote Sensing* (2000), 2142-2152.

[Rocca and Tebaldini, 2009] F. Rocca, S. Tebaldini, "BioSAR2008 – Data Analysis II", ESTEC Contract No. 22052/08/NL/CT, 2009.

[Tebaldini and Rocca, 2009 a] S. Tebaldini and F. Rocca, "On the impact of propagation disturbances on SAR Tomography: Analysis and compensation", RadarCon 2009, Pasadena , 2009.

[Tebaldini, 2009 b] Tebaldini, S.; "Algebraic Synthesis of Forest Scenarios From Multibaseline PolInSAR Data", *IEEE Transactions on Geoscience and Remote Sensing*, 4132 -4142, 2009.

[Tebaldini and Rocca, 2010] Tebaldini, S.; Rocca, F.; "Forest structure from longer wavelength SRS," *Geoscience and Remote Sensing Symposium (IGARSS), 2010 IEEE International* , vol., no., pp.158-161, 25-30 July 2010.

[Tebaldini and Rocca, 2012] Tebaldini, S. and Rocca, F., "Multibaseline Polarimetric SAR Tomography of a Boreal Forest at P- and L-Bands", *Geoscience and Remote Sensing, IEEE Transactions on* (2012), 232 - 246.

7. CONCLUSIONS AND RECOMMENDATIONS

The conclusions to be drawn from this study concern two research topics pertaining to the observations of tropical forests using a P-band SAR. The ground based TropiScat experiment was set up to address the temporal survey of the variations of SAR measurements in various time scales. The study on TropiSAR campaign data aimed at assessing the retrieval algorithms developed using full resolution airborne data on the data processed with a 6 MHz bandwidth allocated for P-band Earth Observation missions.

7.1. TROPISCAT

The major objective of the experiment is the temporal survey of the radar measurements in time scales ranging from diurnal, weekly, monthly, up to 12 months of observations. The measurements which have been assessed are: a) the temporal coherence in HH, VV and HV polarizations, b) the Intensity at HH, VV and HV polarizations and the vertical distribution of temporal coherence, as obtained by tomographic processing.

7.1.1. EXPERIMENTAL SET UP

The analyses carried out on the data collected in the TropiScat experiment fully confirmed the feasibility of retrieving accurate information on the temporal coherence, the polarimetric intensity, and the forest vertical structure through tomographic imaging.

It was shown that the tower itself does not perturb the measurements (e.g. by its motion and by coupling phenomenon), that the distances estimated by impulse responses are accurate, and that the system stability at short term (up to few hours) is excellent, whereas the long term (up to 1 year) stability is observed when the system coherence was taken into account. In addition, for polarimetry, system cross talk is well below the forest level.

In the temporal survey of both impulse responses and vertical SAR measurements, the effect of wind-induced motions of the forest has been found important on the coherence during the day time, and quite negligible during night time. However, this effect was found strongly mitigated by averaging over a number of acquisitions (e.g. averaging over 1 or 2 hours for acquisitions of 15 minutes each, or few minutes for each tomographic acquisition). The tower stability during night time also confirms the feasibility of accurate measurements of temporal decorrelation at 6 am and 6 pm, which are the local time for the future Biomass acquisitions. However, it was found that the rainfall is strongly affecting the measurements and the data acquired during rainfalls are excluded from the analysis.

7.1.2. TEMPORAL DECORRELATION

The main goal of this campaign is to study the temporal coherence for the tropical forest at P band for temporal baselines from days to months. For this purpose, three months of data acquired in the rainy and dry periods were analyzed with range impulse responses issued from various antennas pairs. The following results are obtained:

- Coherence exhibits a daily cycle showing a high decorrelation during the day and low decorrelation during night time. Those diurnal cycles are similar to diurnal variations of dielectric constants measured over forests as reported in literature. In addition to this, decorrelation is accentuated by the wind, which occurs systematically during day time, in both rainy and dry seasons. High coherence is observed from dusk to dawn, (6 pm to 6 am), which are the planned acquisition time of Biomass. These cycles are also perturbed by the rain.

- In the dry period, up to 20 days, the mean coherence is higher than 0.8 for all polarizations. This is the most important result since it shows that over such a temporal baseline coherence is sufficient to envisage coherent processing based on repeat pass acquisitions.
- In the rainy period the coherence drops quickly to 0.7 in the very first temporal baseline (3 days) and decreases very slowly after that to reach 0.6 at 60 day baseline.

Although there is a need to assess the generality of the findings (for example in terms of the wind in tropical forests), these results already show the relevance of the choice of the satellite dawn dusk helio-synchronous orbit to minimize the wind decorrelation effect. During the dry season, the coherence is sufficient at 20 days for coherent processing, whereas during the rainy season, the temporal decorrelation should be accounted for.

7.1.3. BACKSCATTERING INTENSITY

Due to the strong penetration of P band waves inside the canopy, more significant temporal variation would be expected, e.g. through changing ground conditions. Using TropiSAR data, the standard deviation of temporal variation for the 7 P-band SAR acquisitions over forest reference plots has been found to be less than ± 0.3 dB during 1 month in the dry season in 2009. With the TropiScat experiment, the objective is to analyze the temporal variation of the backscattering intensity during the day, and for time series encompassing the dry and rainy seasons, in order to constitute a database that can be used for statistical assessment of temporal variation of the backscattering intensity, and for studying the cause of this temporal change, either linked to forest ecophysiology, and/or to meteorological conditions effect. The following results have been obtained:

- The backscattering intensity shows a diurnal cycle (± 0.5 dB) which is compatible with the diurnal variation of the dielectric constant reported in literature.
- For a given time of the day (e.g. 6 am or 6 pm), the backscatter intensity shows a slow decrease through the dry season and a small increase through the rainy season. Although small (less than 1 dB after 3 months), the change in backscattering intensity needs to be accounted for in the retrieval algorithms. This is because such variation will result in very large uncertainties in the retrieved biomass, considering the small sensitivity of the backscatter intensity to AGB for the high values of AGB (> 300 t/ha) in tropical forest.

7.1.4. TOMOSAR

Tomographic processing was aimed at investigating the link between the temporal decorrelation over time and forest vertical structure at P-Band. The following results have been obtained:

- Diurnal analysis revealed a diurnal vertical motion of the forest center of mass. This phenomenon suggests a connection with forest ecophysiology.
- The temporal coherence drops during daytime, due to the effect of the wind moving the forest canopy. This confirms that acquisitions over tropical forests at dawn dusk are relevant for Biomass.
- Long term coherence was analyzed during the rainy season and the dry season. Only dawn-dawn and rain free acquisitions are considered.

The estimated temporal behavior was found changing within the forest volume, the highest coherence values being observed at the ground level (higher than 0.8 at 27 days in all polarimetric channels), whereas coherence at canopy height is about 0.8 at 4 days and about 0.65 at 27 days.

Finally, we remark that for the rain-free days, no relevant difference was observed between the rain and dry seasons.

7.1.5. TROPISCAT RECOMMENDATIONS/ FURTHER WORKS

The TropiScat experiment has already provided a large amount of data which still needs further analysis and interpretation.

The works to be conducted can be identified as follows:

- To continuously calibrate data with external calibrator
- To exploit bio-geophysical parameters in relation with diurnal, seasonal variations of the temporal coherence, and the backscattering coefficient during dry and rainy season. The following parameters can be considered:
 - Dielectric constant of the tree elements, in particular the branches, for which non destructive methods should be developed
 - Water vapor pressure deficit
 - Long term soil moisture variation
 - Wind in the tropical forests
- To discriminate general effects versus site specific observations (e.g. wind in tropical forest versus wind in Paracou, general scattering mechanisms in tropical forest versus mechanisms specific to the topographic conditions in Paracou).
- To carry out scattering modeling to interpret the measurements observed as a function of bio-geophysical parameters and to investigate inversion strategies.
- To draw recommendations for Biomass : This concerns how to include TropiScat observation results in Biomass retrieval algorithms, leading for example to methods to mitigate the low coherence caused by rain effect, or to delete the rainy acquisitions with the use of ancillary data (e.g. meteorological satellites) ; also methods to account for temporal variations in backscattering intensity using polarimetry.

It is important that the Tropiscat experiment could be maintained for a longer period to address the question of longer terms variations. In particular, 2012 has been a particular year for the rainy and dry periods in French Guiana (and in the Amazon forest).

The TropiScat experiment, already provides useful results in terms of observations and understanding of the temporal variations of the P-band SAR measurements over a tropical forest, can be extended in a next step on another tropical forest spot with other forest characteristics and other conditions of topography, soil type, and weather conditions etc.

7.2.ASSESSMENT OF RETRIEVAL PERFORMANCE WITH TROPISAR 6 MHZ DATA

The work has focused on assessing the performance of TropiSAR P-Band SAR processed for 6 MHz bandwidth in the retrieval of forest biomass and forest height in tropical forests. The major impact of the 6 MHz limitation is a significant reduction of the number of looks to be used for coherence and backscatter intensity evaluation, and for tomography, a significant vertical resolution loss. The retrieval methods developed and assessed using the full resolution TropiSAR data (at 125 MHz) data needs therefore to be evaluated.

7.2.1. THE PROCESSED DATA

The data were processed to have similar resolution than the Biomass resolution: about 25m (6 MHz) in range resolution and 7.5m in azimuth resolution. The data calibration using corner reflectors was a real challenge as the calibration reflectors on the ground were not large enough to be detected in the data of reduced resolution. A resolution (using an intermediate bandwidth of 50MHz) was necessary to access the antenna variation across the swath, which was subsequently applied to the 6MHz data. The radiometric calibration is estimated to be about $\pm 0.8\text{dB}$, the Noise-Equivalent sigma to be around -34dB and the cross-talk level to be of the order of -25dB .

7.2.2. ASSESSMENT OF POLSAR RETRIEVAL ALGORITHM

The retrieval of biomass using backscatter intensity in tropical dense forest is a challenging task, because the sensitivity of backscatter to biomass in the range of $250\text{-}300\text{ t ha}^{-1}$ is easily masked by perturbing effects, particularly those related to topography. Recovering the biomass signal therefore needs careful correction for these effects. To this aim, the backscattering coefficient t^0 which minimizes topographic effect has been developed and applied to full resolution TropiSAR data. The method has been assessed using 6 MHz data, provided a correlation coefficient between t^0 and AGB of 0.77 over 16 reference plots. The biomass inversion provided a relative error of 17%. However, for the full resolution data, it was possible to derive the model parameters from the other French Guiana site and to validate the method at the Paracou site. In addition, it was possible to use subplots derived from the 16 reference plots for statistical analysis.

7.2.3. POLINSAR

The PolInSAR height retrieval was applied on the 6 MHz data. The analysis has shown that the underlying topography can introduce important artifact in the vegetation height map and a method to correct a posteriori this effect has been applied. The following results are obtained:

- The Ground elevation model (DEM) derived from PolInSAR DEM is found in good agreement with the LiDAR DEM. The standard deviation error is of 3.8 m (as compared to the 2.7 m for the full 125 MHz bandwidth data)
- The PolInSAR vegetation height or digital canopy model (DCM) is compared to the LiDAR DCM. Qualitatively, vegetation structure revealed by PolInSAR height image is similar to the vegetation structure described by the LiDAR image. Quantitatively, the vegetation height information is over-estimated in PolInSAR inversion (whereas good correlation has been obtained with full bandwidth data).

7.2.4. POLSAR & POLINSAR

Method combining PolSAR and PolInSAR height for the retrieval of AGB has been developed. A Bayesian approach is proposed to handle the various noise sources that affect intensity and PolInSAR. Since the error sources are independent in these two SAR measurements, the combination of them improved significantly the retrieval performance.

The performance of the retrieval is quantified by the relationships between the retrieved biomass and the in situ biomass:

- Intensity based method: the correlation between the retrieved AGB and in situ AGB is of the order of 0.6. The relative RMSE is about 17%.
- Pol-InSAR based method: the correlation between the retrieved AGB and in situ AGB is in the range of 0.50, providing 15% RMSE.

- The combined technique shows significant improvement, retrieval results comparable to TomoSAR, with a correlation of 0.8, providing 11 % RMSE

7.2.5. TOMOSAR

In addition to the 6 MHz data processing by ONERA, another method was undertaken at PoliMi and the data processed by the two methods have been evaluated. Low resolution data were derived by first recovering the 3D distribution of the scatterers at high resolution, which was then re-projected onto the low resolution 'spaceborne' geometry. This procedure allows obtaining a data stack that is consistent with spaceborne data concerning not only spatial resolution, but also geometrical features, i.e.: system LOS.

The following results have been obtained:

- TomoSAR processing can be successfully employed to decompose the backscattered power from a tropical forest into two-three layers, and hence provide valuable information about the forest structure,
- A correlation value with respect to ABG higher than 0.8 for AGB values ranging from 250 t/ha to 450 t/ha was obtained with the backscatter intensity at the 30 m layer above the ground. This result is consistent with the one obtained by processing the full-bandwidth (125 MHz) TropiSAR data [Ho Tong et al., 2012]. The retrieved relative accuracy of the retrieved biomass was found to be better than 20% at 1.5 ha resolution and better than 10% at 6 ha resolution,
- Forest height was estimated by tracing the upper envelope of TomSAR vertical profiles, averaged over a 100 m x 100 m window. Height estimation was found reliable for vegetation height ranging from 20 m to 30-35 m, which prevails in tropical forests. For this range of forest height, standard deviation was found less than 4 m.

7.2.6. RECOMMENDATIONS AND FURTHER WORKS

The overall results of this study prove that the 6 MHz bandwidth limitation is not critical concerning P-band SAR observations of tropical forests. However, in order to have a full assessment of the end- to- end performances, different types of noise sources still need to be considered. Those are for example the ionospheric disturbances, the seasonal effects (the TropiSAR data were acquired during the dry season), the temporal decorrelation. Reversely, some of the effects prevailing in airborne data will be less significant in spaceborne data. This is the case for example of the large variation of the incidence angle across the swath, the perturbations in the flight tracks of the aircraft.

For the different retrieval methods, there is a need to have a similar error assessment structure, linking different sources of error including errors in in-situ data, and errors in the radar data.

The performance assessment has been done on the in situ reference plots (e.g. the 16 plots in Paracou forest), whereas the retrieved biomass maps have been provided for the entire area of Paracou. The relevance of the inversion outside the forest areas needs to be assessed. Alternatively, the methods could be applied only on forest areas, prealably identified and localized (e.g. using polarimetry).

The transferability of the methods has not been demonstrated with the 6 MHz data, for example by training from Paracou and validating the results in Nouragues, or vice versa, as was done with the PolSAR method using 125 MHz TropiSAR data. This is because the data have been processed at 6 MHz only at the Paracou site. Furthermore, it is foreseen that the size of the reference plots in Nouragues (100 m x 100 m) is not sufficient for an accurate plot location using the 6MHz SAR data in this site with significant tomography.

Finally, significant learning has been gained with a single airborne campaign. This is particularly important for tropical forests, which have not been extensively studied in terms of P-band SAR. To complete our knowledge, other airborne campaigns need to be foreseen, with the following criteria for test site selection:

- A tropical rain forest with structure and moisture different from Amazonian forest. This is the case for example of tropical forest in Africa,
- The site should include a gradient of biomass conditions. In particular both the high range of biomass (> 300 t/ha), but also biomass in the 50 - 300t/ha range, not covered by the TropiSAR campaign.
- Similarly to TropiSAR, test sites should have established measurement infrastructure, ancillary data and on-going science activities which can support and benefit from a campaign.
- The site should have a number of large reference forest plots (4 ha or larger) for methods calibration and validation. Alternatively, the possibility to use Lidar data for extension of the existing in situ plots will also be considered.